

Simulating intermediate black hole mass measurements for a sample of galaxies with nuclear star clusters using ELT/HARMONI high spatial resolution integral-field stellar kinematics

Dieu D. Nguyen¹*, Michele Cappellari², Hai N. Ngo^{3,4}, Tinh Q. T. Le^{5,4}, Khue N. H. Ho^{5,4}, An K. Nguyen^{5,4}, Huy G. Tong^{3,4}, Phong T. On^{5,4}, Tuan N. Le^{6,4}, and Miguel Pereira-Santaella⁷

¹Université de Lyon 1, Ens de Lyon, CNRS, Centre de Recherche Astrophysique de Lyon (CRAL) UMR5574, F-69230 Saint-Genis-Laval, France

²Sub-Department of Astrophysics, Department of Physics, University of Oxford, Denys Wilkinson Building, Keble Road, Oxford, OX1 3RH, UK

³University of Science, 227 Nguyen Van Cu Street, Ward 4, District 5, Ho Chi Minh City, Vietnam

⁴Vietnam National University in Ho Chi Minh City, Vietnam

⁵Department of Physics, International University, Quarter 6, Linh Trung Ward, Thu Duc City, Ho Chi Minh City, Vietnam

⁶University of Technology, 268 Ly Thuong Kiet Street, Ward 14, District 10, Ho Chi Minh City, Vietnam

⁷Instituto de Física Fundamental, CSIC, Calle Serrano 123, 28006 Madrid, Spain

Accepted XXX. Received YYY; in original form ZZZ

ABSTRACT

The fraction of low-mass galaxies hosting an intermediate-mass black hole (IMBH, with masses $M_{\text{BH}} \approx 10^2 - 10^5 M_{\odot}$), is sensitive to how black hole seeds formed in the early Universe but is observationally still unconstrained. In this paper, we assemble a sample of dwarf galaxies within 10 Mpc hosting bright nuclear star clusters (NSCs) that could host IMBHs. For a subset of them, we use their observed surface brightness from *Hubble Space Telescope* (*HST*) images, an assumed synthetic spectrum of their stellar population, Jeans Anisotropic Model (JAM) of the stellar dynamics, and the HSM simulator software to create mock observations with the High Angular Resolution Monolithic Optical and Near-infrared Integral (HARMONI) field spectrograph for the Extremely Large Telescope (ELT). We analyze the simulated data cube like real data, using JAM to infer the IMBH mass and its error in a Bayesian framework. Our simulations show that the ELT/HARMONI instrument can clearly detect the existence of IMBH demographics in NSCs down to a mass of about 0.5% of the NSC.

Key words: galaxies: general – galaxies: supermassive black holes – galaxies: nuclei – galaxies: kinematics and dynamics – galaxies: evolution – galaxies: formation

1 INTRODUCTION

Both theoretical (e.g. Silk & Rees 1998; Di Matteo et al. 2008) and observational (e.g. Marconi & Hunt 2003; Häring & Rix 2004) studies have firmly established a correlation between the mass of central supermassive black holes (SMBHs, $M_{\text{BH}} > 10^6 M_{\odot}$) and the large-scale properties of nearby massive galaxies ($M_{\star} \gtrsim 10^{10} M_{\odot}$, e.g. Kormendy & Ho 2013; Sahu et al. 2019a,b). These properties encompass the stellar mass (M_{\star} ; e.g. Magorrian et al. 1998) and luminosity (e.g. Kormendy & Richstone 1995) of the central spherical bulge of stars, as well as its statistical dispersion of stellar velocities (σ_{\star} ; e.g. Ferrarese & Merritt 2000; Gebhardt et al. 2000). These robust black hole–galaxy scaling correlations strongly suggest a close connection between the growth of SMBHs and the formation and evolution of their host galaxies (e.g. Schawinski et al. 2007; Fabian 2012; Krajnović et al. 2018a).

Additionally, the evolutionary trajectories of SMBHs over cosmic time provide invaluable constraints that are vital for a comprehensive understanding of the assembly and development of both galaxies and their central black holes (Gültekin et al. 2009; Netzer 2015). These connections offer profound insights into the intertwined cosmic story

of black holes and galaxies, shedding light on the underlying physical processes that have shaped the universe we observe today.

In the cosmos surrounding us, central black holes are commonly classified into two primary categories: stellar-mass black holes and SMBHs. The stellar-mass black holes possess masses ranging from a few to several tens of solar masses, and their origins are well-established as the remnants of massive stars that conclude their life-cycles by undergoing supernova explosions. In contrast, the formation mechanisms of SMBHs remain enigmatic (e.g. Volonteri et al. 2008). It is conceivable that SMBHs could grow from smaller stellar-mass “seeds” ($M_{\bullet} \approx 10^{2-3} M_{\odot}$; e.g. van Wassenhove et al. 2010; Volonteri 2012). Alternatively, these enigmatic objects may have originated as massive seeds, formed through the direct collapse of pristine gas ($M_{\bullet} \approx 10^{4-5} M_{\odot}$; e.g. Greene 2012; Bonoli et al. 2014) in extreme conditions shortly after the Big Bang.

Presently, a significant disparity exists in the limited resolving powers of both space-based and ground-based telescopes, resulting in a substantial gap (approximately spanning three orders of magnitude in M_{BH} ; Nguyen et al. 2018) that separates these two distinct populations of black holes. The nature of this gap, situated between the most massive stellar-mass black holes detected by LIGO ($M_{\text{BH}} = 142 M_{\odot}$; Graham et al. 2020) and the lowest mass dynamically confirmed central black hole ($M_{\text{BH}} \sim 10^5 M_{\odot}$; Pechetti et al. 2022), remains a subject of uncertainty. This gap may arise from the

* E-mail: nddieuphys@gmail.com

absence of black hole populations within this mass range, termed “intermediate-mass” black holes (IMBH, $M_{\text{BH}} \sim 10^{2-5} M_{\odot}$), or it could be attributed to our current limitations in detecting them.

1.1 Previous IMBH determinations

Over the past decades, extensive studies have provided dynamical M_{BH} measurements for approximately 120 galaxies (see a review by [Greene et al. 2020](#)), in which there are 23 IMBHs. These measurements determine black hole masses by analyzing stellar motions (e.g. [Verolme et al. 2002](#)), ionised gas dynamics (e.g. [Walsh et al. 2013](#)), CO-molecular gas dynamics (e.g. [Davis et al. 2013](#); [Nguyen et al. 2020](#)), [C I]-atomic gas dynamics (e.g. [Nguyen et al. 2021](#)), or accretion disks (e.g. [Miyoshi et al. 1995](#); [González-Alfonso et al. 2023](#)). Remarkably, these investigations have unveiled the ubiquity of black holes in high-mass galaxies ($M_{\star} \gtrsim 10^{10} M_{\odot}$; e.g. [Kormendy & Ho 2013](#); [Saglia et al. 2016](#)). However, the situation is notably less clear in lower-mass galaxies, where central black holes are anticipated to be IMBHs (e.g. [Seth et al. 2010](#); [Nguyen et al. 2014, 2017](#); [Davis et al. 2020](#)) or, in some cases, absent altogether (M33; e.g. [Gebhardt et al. 2001](#)).

For instance, initial measurements conducted on galaxies within the Local Group ($D < 3.5$ Mpc) boasting stellar masses exceeding $10^9 M_{\odot}$ indicated a notable absence of central IMBHs (e.g. [Gebhardt et al. 2001](#)). However, recent observations have hinted at the detections of a few IMBHs residing at the cores of dwarf galaxies ([den Brok et al. 2015](#); [Nguyen 2017](#); [Nguyen et al. 2019, 2022](#)) and massive globular clusters (GCs) like [Pechetti et al.](#) (work on B023-G078; 2022) and [Gebhardt et al.](#) (study of the brightest GC, G1 in M31; 2002). These IMBHs were identified through the disturbances observed in the motions of stars and gas within these objects. Additionally, the presence of IMBHs has been inferred from X-ray and radio emissions, believed to originate from matter falling onto a black hole, with the most compelling detection being the off-nuclear X-ray source HLX-1 (e.g. [Straub et al. 2014](#)). Furthermore, considering some M_{BH} -galaxy’s macroscopic properties scaling relations (e.g. [Kormendy & Ho 2013](#); [Greene et al. 2020](#)), IMBH populations are expected to inhabit the centers of $\sim 10^{8-9} M_{\odot}$ galaxies (as referenced therein), $\sim 10^{6-7} M_{\odot}$ ultra-compact dwarf galaxies (UCD; e.g. [Seth et al. 2014](#)), and $\sim 10^{5-6} M_{\odot}$ GCs. (e.g. [Gebhardt et al. 2005](#)), with decreasing mass from $10^5 M_{\odot}$ to $10^2 M_{\odot}$.

However, if IMBHs do indeed exist in low-mass galaxies, their demographics bear significant relevance to several intriguing astrophysical inquiries. The predictions stemming from stellar-mass seeding black holes suggest a high “occupation fraction” – i.e. a high likelihood that IMBHs are hosted by $10^9 M_{\odot}$ galaxies, estimated to be around 80–100% ([Nguyen et al. 2018](#)). Conversely, the massive seeding scenario proposes a lower fraction of IMBHs in such galaxies (e.g. [Gallo et al. 2008](#)). The occupation fraction serves as a critical metric for quantifying black hole number density, thereby influencing our expectations regarding the rate of stellar tidal disruptions (e.g. [Kochanek 2016](#); [Wevers et al. 2017](#)). It also plays a pivotal role in studies aimed at determining the number of black holes likely to be discovered in the nuclei of stripped galaxies (e.g. [Ahn et al. 2018](#)). Moreover, obtaining compelling evidence of an IMBH census holds vital importance in constraining their formation mechanisms and their relationship with SMBHs and stellar-mass black hole populations ([Nguyen 2019](#)). Such findings will further refine predictions for gravitational-wave experiments (e.g. [Bailes et al. 2021](#)), enhancing our understanding of the broader astrophysical implications associated with IMBHs.

Furthermore, an imperative aspect of the quest for IMBH demo-

graphics lies in its profound implications for our understanding of galaxy formation, co-evolution across cosmic epochs, and the broader formation of cosmic structures (e.g. [Mezcua 2017](#)). The core strategy in the search for these IMBHs involves scrutinizing the dynamic signatures exhibited by stars and gas at the centers of nuclear star clusters (NSCs; [Neumayer et al. 2020](#)) in dwarf galaxies, as well as within Galactic and intergalactic globular clusters (GCs; [Noyola et al. 2010](#)). These signatures arise due to the presence of a massive, compact, dark, and centrally concentrated mass that exceeds what would be anticipated from dynamical mass-segregation processes (discussed in Section 7.2). In very nearby stellar systems, it is plausible to expect roughly one star per central spaxel, facilitating the measurement of radial velocities for individual stars. However, in more distant systems, we continue to rely on the integrated light distributions of the bulk of stars within a single spaxel, provided that the spaxel falls within the black hole’s sphere of influence (SOI¹) radius ($R_{\text{SOI}} = GM_{\text{BH}}/\sigma_{\star}^2$, where G represents the gravitational constant).

To precisely measure the motions induced by IMBHs within their SOI, both spectroscopic and photometric observations must marginally resolve the R_{SOI} . For IMBHs within a distance of ≈ 10 Mpc, this R_{SOI} spans from a few thousandths of a parsec to a few parsecs (e.g. [de Zeeuw 2001](#)). These observational scales plunge below the diffraction limits of instruments like Gemini or the Very Large Telescope (VLT) equipped with adaptive optics (AO) techniques. These instruments provide a point spread function (PSF) with a full width at half maximum $\text{FWHM}_{\text{PSF}} \approx 0''.08 - 0''.1$, equivalent to a range from a few parsecs to a few tens of parsecs for the same sample. The current Enhanced Resolution Imager and Spectrograph (ERIS) on VLT promises a spatial resolution of about ≈ 50 milli-arcseconds (mas). However, even this level of resolution falls short in probing the SOI of a typical $10^4 M_{\odot}$ IMBH at a distance $D \approx 10$ Mpc because such a small black hole exerts minimal gravitational influence on its surroundings. Furthermore, while the *James Webb Space Telescope* (*JWST*) enhances the flux sensitivity of ongoing black hole surveys, it does not substantially improve spatial resolution. Consequently, compelling evidence for the existence of IMBH populations remains elusive beyond the Local Group, and current observational facilities do not allow unambiguous confirmation.

1.2 The role of ELT/HARMONI

The unanswered question regarding the existence of IMBH populations awaits the arrival of the Extremely Large Telescope (ELT) and its High Angular Resolution Monolithic Optical and Near-infrared Integral (HARMONI) field spectrograph ([Thatte et al. 2016, 2020](#)) along with the Multi-AO Imaging Camera for Deep Observations (MICADO) imager ([Davies et al. 2010, 2021](#)). These instruments are equipped with AO and offer unprecedented levels of sensitivity and spectral/angular resolution, boasting $R = \lambda/\Delta\lambda \sim 7, 100$ and $\sim 17,400$ for HARMONI. The HARMONI system, as reported in [Nguyen et al. \(2023\)](#) (hereafter N23), provides an $\text{FWHM}_{\text{PSF}} \approx 12$ milli-arcseconds (mas), while MICADO reaches an $\text{FWHM}_{\text{PSF}} \approx 10$ mas ([Davies et al. 2010](#)). The combination of HARMONI integral field spectroscopy (IFS) and MICADO imaging on the ELT platform will have the capacity to detect IMBHs at distances up to 10 Mpc (as detailed in this work). These IMBHs represent a crucial missing link

¹ The spherical space-time region surrounding the black hole where its gravitational force dominates other matter’s gravity, which is also defined as the black hole vicinity whose enclosed mass equals twice the black hole mass (or enclosed galaxy-mass equals the black hole mass).

between stellar-mass black holes and SMBHs and may have served as seeds for the formation of present-day SMBHs in the early Universe (e.g. Inayoshi et al. 2020; Greene et al. 2020).

The utilization of HARMONI will enable us to conduct indepth and precise three-dimensional (3D) kinematic studies of stellar populations within NSCs – locations where IMBHs are believed to be situated (as expounded in N23 for much higher mass black holes). Additionally, with MICADO, we can achieve substantially higher spatial resolution (a few mas compared to a hundred of mas with *JWST*). Consequently, the observable volume will expand by over tenfold compared to current capabilities for the search for nearby IMBHs. This extended reach will enable a significant increase in the number of direct measurements of black hole masses that can be conducted, ranging from a few to several tens. Ultimately, the ELT will facilitate dynamic measurements of prominent young star clusters. The unequivocal detection of IMBHs within such clusters carries profound implications for understanding the formation of black hole seeds during the early Universe (e.g. Greene et al. 2020).

We outline the specific selection criteria we have devised for the identification of our HARMONI IMBH survey sample in Section 2, while presenting the key properties of this sample in Section 3. Subsequently, in Sections 4 and 5, we elucidate the dynamical and photometric models we employ in our simulations, respectively. Moving on to Section 6, we undertake near-infrared (NIR) IFS simulations utilizing the HARMONI SIMULATOR (HSIM²; Zieleniewski et al. 2015) software designed for ELT observations with the HARMONI instruments. Within this section, we present the simulated datacubes and the methodologies employed for extracting stellar kinematics. In Section 7, we engage in a comprehensive discussion of the potential applications of dynamical modeling to measure the masses of central black holes using the observations, accompanied by a consideration of their limitations. Finally, our findings are summarized and concluded in Section 8.

In this paper, we adopt a flat Universe model with a Hubble constant of $H_0 \approx 70 \text{ km s}^{-1} \text{ Mpc}^{-1}$, a matter density of $\Omega_{m,0} \approx 0.3$, and dark energy density $\Omega_{\Lambda,0} \approx 0.7$, which are in accordance with constraints derived from both the Planck collaboration (Planck Collaboration et al. 2014) and WMAP (Calabrese et al. 2017). We ensure uniformity by applying a foreground extinction correction (Schlafly & Finkbeiner 2011) and utilizing the interstellar extinction law proposed by Cardelli et al. (1989) for all quantities. Furthermore, to maintain consistency throughout our work, we employ the AB-photometric magnitude system (Oke 1974) and orient all kinematic maps, aligning the horizontal and vertical directions with the galaxy’s major and minor axes, respectively.

2 SAMPLE SELECTION

We first describe the selection process to find the best dwarf galaxies hosting bright NSCs, where IMBHs probably reside and are observable with ELT in Section 2.1, and then we summarize the selection criteria in Section 2.2.

2.1 Sample selection process

Our target selection process involves two primary steps. Initially, we employed the same methodology as outlined in N23, utilizing homogeneously obtained NIR *K*s-band ($\approx 2.2 \mu\text{m}$) photometric data

sourced from the Two Micron All Sky Survey (2MASS; Skrutskie et al. 2006) and the 2MASS redshift survey (2MRS; Huchra et al. 2012). This initial step was aimed at identifying dwarf galaxies within proximity of $\lesssim 10 \text{ Mpc}$. These selected targets exhibit a stellar mass range falling within $2 \times 10^6 \lesssim M_\star \lesssim 5 \times 10^{10} M_\odot$, measured using either the simplification of a uniform mass-follow-light hypothesis with the mass-to-light ratio of $M/L_K = 1 (M_\odot/L_\odot)$ (Nguyen et al. 2018) or the equation (2) of Cappellari (2013) (i.e. $\log(M_\star) = 10.58 - 0.44 \times (M_K + 23)$ and $-23.3 \leq M_K \leq -13.3 \text{ mag}$), which is 1.8 mag overlapping the low- M_K boundary of the ATLAS^{3D} survey ($M_K < -21.5 \text{ mag}$; Cappellari et al. 2011). It is important to note that Bell & de Jong (2001) and Maraston (2005) have demonstrated that the *K*s-band is less susceptible to dust absorption compared to optical wavelengths, by a factor of 5–10, and that M/L_K exhibits less variability, by a factor of 2–3. Subsequently, in the second step of our selection process, we conducted a thorough cross-referencing of these preselected targets with all available surveys focusing on nearby low-mass galaxies known to host luminous NSCs, where IMBHs are likely to reside.

The necessity for the second step arises due to certain limitations associated with the 2MASS data. Specifically, 2MASS employs the de Vaucouleurs “effective” aperture for measuring a galaxy’s half-light radius, denoted as R_e (the radius encompassing half of the galaxy’s total light), and extrapolates the surface brightness profile of the galaxy to derive its total flux, a technique described in detail by Jarrett et al. (2003). In practice, this involves integrating the flux in incremental annular regions, commencing from the center ($r > 5''$), and moving along the elliptical contours of the galaxy until the half-light point is reached. Subsequently, interpolation is used to construct a precise value for R_e . While this approach is robust for larger galaxies and remains largely unaffected by the PSF circularizing effects, it becomes increasingly susceptible to inaccuracies when estimating R_e for dwarf galaxies.

Furthermore, it is important to note that 2MASS observations tend to possess relatively shallow photometric depths, a characteristic highlighted by Schombert & Smith (2012). This shallow depth may potentially result in an underestimation of the galaxy’s *K*s-band luminosity, thus complicating the accurate determination of Sérsic indices for light profiles in sources with relatively compact dimensions. As a result of these limitations, relying solely on 2MASS (and 2MRS) data for the identification of dwarf galaxies becomes inherently unreliable. Nevertheless, it is worth emphasizing that these datasets serve as valuable starting points for preselecting candidate galaxies that are characterized by less dust extinction, proximity, and relatively faint luminosity, while also providing robust estimates of their stellar masses.

To determine the luminosities and stellar masses of galaxies based on their observed apparent magnitudes, we followed a methodology akin to the approach employed in the Most Massive Black Holes (MMBH) IFS survey, which targeted ultra-massive galaxies with ELT/HARMONI (N23). A crucial prerequisite for this process is knowledge of the distances to the target galaxies. Among the extensive 1.65 million galaxies catalogued in the 2MASS extended source catalog (XSC; Skrutskie et al. 2006), approximately 100,000 of them possess redshift-independent distances available from the NASA/IPAC Extragalactic Database (NED³), denoted as NED-D⁴ (XSC; Steer et al. 2017). For these galaxies, we conducted matching with the 2MRS galaxies and adopted their NED-D distances, which

² v3.11; available from <https://github.com/HARMONI-ELT/HSIM>

³ <https://ned.ipac.caltech.edu/>

⁴ <http://ned.ipac.caltech.edu/Library/Distances/>

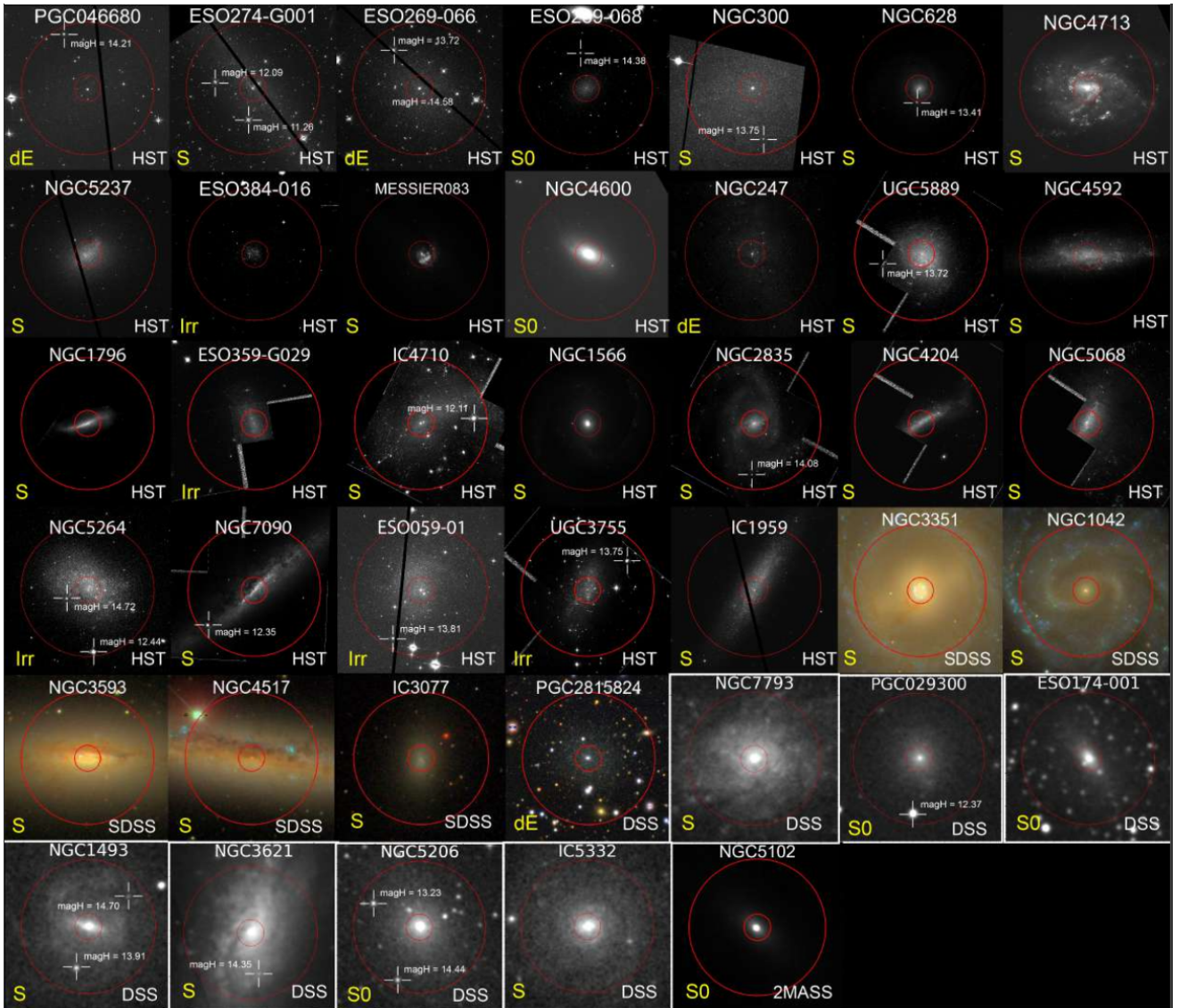


Figure 1. The 40 available observations of the nuclei out of the total number of 40 dwarf galaxies from our HARMONI IMBH sample, as captured in *HST*, SDSS, DSS, and 2MASS images (depicted in the white legend at the right corner of each insect panel and listed in the number from 1 to 40 in Fig. A1 in the supplementary material). To emphasize their NSCs at the core, the galaxy brightness has been adjusted. Each galaxy’s name (shown in the white legend at the top of each insect panel) and galaxy types (presented in the yellow legend at the left corner of each insect panel) are also shown. Two red circles define the region around the galaxy’s center, spanning from $12''$ to $60''$, where we search for a faint NGS essential for LTAO performance. The white crosses pinpoint the available NGS locations, specifying their apparent AB magnitudes measured in the *H* band. Here, dE = dwarf Elliptical, S0 = lenticular, S = Sprial, Irr = Irregular.

are estimated with a typical accuracy of approximately (10–20)%. In cases where the 2MRS targets lacked NED-D distances (but less likely for the nearby targets), we derived distances based on their redshifts, incorporating corrections for peculiar motions arising from the Virgo cluster listed in NED (Mould et al. 2000). These corrections were crucial to ensure the accuracy of redshift distances, which were then employed in our preliminary survey with a distance criterion of $2 \lesssim D \lesssim 10$ Mpc. More specifically, the redshift distances were calculated using the formula $D = V_{\text{cosmic}}/H_0$, where V_{cosmic} represents the cosmic velocity. This cosmic velocity, in turn, was calculated as the sum of the observed heliocentric velocity (V_{hel}), a correction for the Local Group centroid motion ($V_{\text{c,LG}}$; sourced from table A1 of Mould et al. 2000), and the correction for the Virgo cluster infall ($V_{\text{in,Virgo}}$), which amounted to 200 km s^{-1} at the Local Group.

Table 1. Targets selection criteria for low-mass galaxies host NSCs

Distant range:	$2 \lesssim D \lesssim 10$ Mpc
Galaxies <i>K</i> -band absolute magnitude:	$-23.7 \lesssim M_K \lesssim -14.5$ mag
Central stellar-velocity dispersion range: (peak of NSC, when available)	$\sigma_{\star,c} < 75 \text{ km s}^{-1}$
ELT Observability (Armazones site):	$ \delta + 24^\circ < 45^\circ$
Galaxy zone of avoidance:	$ b > 8^\circ$

Using the obtained distances, we proceeded to transform the observed magnitudes into absolute magnitudes, denoted as $M_K = K_T - 5 \log D - 25 - 0.11 \times A_V$ (Cappellari et al. 2011). In this equation, K_T , signifying `k_m_ext`, represents the apparent mag-

Table 2. Main characteristics of the HARMONI IMBH sample

Galaxy stellar-mass range:	$2 \times 10^7 \lesssim M_{\star} \lesssim 5 \times 10^{10} M_{\odot}$
NSC's mass range:	$10^5 \lesssim M_{\text{NSC}} \lesssim 6 \times 10^7 M_{\odot}$
NSC's effective radius range:	$3 < R_e < 27 \text{ pc}$
#Galaxies in the sample:	$N_{\text{gal}} = 45$
#dwarf Ellipticals ($T \leq -3.5$):	$N_{\text{dE}} = 6$ ($\approx 13\%$)
#Lenticulars ($-3.5 < T \leq -0.5$):	$N_{\text{S0}} = 7$ ($\approx 16\%$)
#Spirals ($-0.5 < T \leq 8$):	$N_{\text{S}} = 27$ ($\approx 60\%$)
#Irregulars:	$N_{\text{Irr}} = 5$ ($\approx 11\%$)

Notes: The galaxy *Hubble* type (T) is defined from HyperLeda: <https://leda.univ-lyon1.fr/search.html>.

nitude in the K_s -band, measured within an isophotal aperture derived from a single Sérsic surface-brightness profile, extrapolated to the inner-unresolved profile (Jarrett et al. 2003). Additionally, A_V corresponds to the Galactic extinction in the Landolt V -band, sourced from Schlafly & Finkbeiner (2011), and incorporates the reddening relation proposed by Charlot & Fall (2000), featuring $R_V = A_V/E(B - V) = 3.1$. Subsequently, we computed the K_s -band luminosities of the galaxies based on their M_K values and estimated the stellar mass of each galaxy under the assumption of a uniform mass-follow-light characterized by the mass-to-light ratio of $M/L_K = 1$ (M_{\odot}/L_{\odot}) (Nguyen et al. 2018).

With a focus on the lower stellar-mass range of $2 \times 10^6 \lesssim M_{\star} \lesssim 5 \times 10^{10} M_{\odot}$, which aligns with the capabilities of ELT for observation (as outlined in Table 1), we initially identified 570 galaxies from the 2MRS survey. To ensure the accuracy of our selections, we conducted a meticulous verification process using the Update Nearby Galaxies Catalogue (Karachentsev et al. 2013). This process involved confirming critical details such as apparent K_s -band magnitudes (or luminosities) and stellar masses. It is important to highlight that, during this step, we excluded sources with 2MASS luminosities and mass that did not align with their values from Karachentsev et al. (2013). Due to the unreliable R_e of 2MASS dwarf galaxies, which are likely included in our initial screening for a sample, their apparent magnitudes (K_T), absolute magnitudes (M_K), and consequently, their estimated stellar masses (M_{\star}) are also considered unreliable. As a result of this thorough examination, we excluded a vast majority of targets that are not present in the catalog or targets with K_s -band estimated luminosities and masses that do not match their values reported in the catalog, resulting in a final selection of approximately 110 dwarf galaxies that met our criteria.

To ensure the efficiency of our quest to detect and accurately measure IMBH masses that might be nestled within low-mass galaxies, we embarked on a search for galaxies housing NSCs exhibiting central stellar-velocity dispersions of $\sigma_{\star,c} < 75 \text{ km s}^{-1}$. The high stellar density within NSCs promises robust signal-to-noise ratios (S/N) during relatively brief exposure times, facilitating unambiguous and minimally error-prone dynamical measurements. Our choice of a velocity dispersion threshold aligns with our objective to identify IMBHs, based on the $M_{\text{BH}}-\sigma_{\star}$ scaling relation derived by Greene et al. (2020), extrapolated to the mass range relevant to IMBHs. Notably, the velocity dispersion criterion significantly impacts the required spatial resolution for HARMONI's imaging capabilities, which must resolve the SOI of IMBHs. To address this demand, we established a canonical lower limit of angular resolution at $R_{\text{SOI}} \approx 10 \text{ mas}$ for the entire sample, factoring in the trade-off between sensitivity and instrumental efficiency, as per the methodology described in equation (1) and section 2.1 from N23.

Next, we meticulously scoured the literature for essential information pertaining to NSCs within the selected dwarf galaxies. This entailed gathering data on NSC properties such as mass, effective

radius, metallicity, stellar populations, ages, and M/L . Additionally, we sought details regarding the stellar velocity dispersions of these NSCs, as well as the half-light radii of the 110 dwarf galaxies that had successfully passed our initial inspection. Our comprehensive search encompassed both photometric sources (e.g. Böker et al. 2002; Walcher et al. 2005, 2006; Seth et al. 2008; Georgiev & Böker 2014; Georgiev et al. 2016; Pechetti et al. 2020) and spectroscopic surveys (e.g. Ho et al. 2009; Kacharov et al. 2018; Nguyen et al. 2018; Fahrion et al. 2022; Baldassare et al. 2022). We also incorporated insights from detailed case studies (e.g. Hägele et al. 2007; Shields et al. 2008; de Swardt et al. 2010; Fahrion et al. 2020; Müller et al. 2021; Pinna et al. 2021; Nguyen et al. 2022). Through this thorough investigation, we identified 40 dwarf galaxies hosting NSCs within the pool of 110 low-mass galaxies that met our stringent criteria.

This final sample shown in Fig. 1 encompasses a diverse array of galaxy types, including 4 dwarf ellipticals, 6 lenticulars, 25 spirals, and 5 irregulars. These galaxies' properties, their NSCs' properties, their possible IMBHs, and related references are recorded in Table A1 of the supplementary material. Furthermore, it encompasses a wide spectrum of large-scale structures such as bulge, bulgeless, bar, and disc configurations. Notably, 17 of these NSCs benefit from high-resolution *Hubble Space Telescope* (HST) images, while the remaining NSCs have archival imagery from the Digitized Sky Survey (DSS⁵), and Sloan Digital Sky Survey (SDSS). This meticulously curated selection of galaxies has been aptly named the ‘‘HARMONI IMBH sample’’.

2.2 Selection criteria

We formed the selected criteria listed as the following selection steps:

(i) The explored volume is opened out to the distant range of $2 \lesssim D \lesssim 10 \text{ Mpc}$, where hosts $-23.3 \leq M_K \leq -13.3 \text{ mag}$ dwarf galaxies. These galaxies contain the well-known NSCs with central velocity dispersion of $\sigma_{\star,c} < 75 \text{ km s}^{-1}$, enforcing the possible IMBHs.

(ii) Observable with ELT that satisfies the limit on the zenith distance for a good AO correction: $|\delta + 24^\circ| < 45^\circ$, where δ is the sky declination (N23).

(iii) The sample must exclude all targets within the Galactic equatorial plane and Galactic bulge regions where highly contaminated by dust: $|b| \leq 8^\circ$. Here, b is the Galactic latitude.

Table 1 provides a concise summary of the selection criteria applied in our process, while Table 2 presents general properties of the low-mass galaxies and NSCs featured in the final HARMONI IMBH sample. It is important to note that in the finalization of our selected targets, an additional prerequisite emerges – namely, the availability of a tip-tilt star in close proximity to the science target (or a natural-guide star, NGS). This star serves as a reference point in the sky for the correction of atmospheric turbulence effects during ground-based IFS observations. To meet this requirement, the NGS stars should possess a magnitude of $m_H < 19$ in Vega mag (or $< 20.4 \text{ AB mag}$) and be situated at distances ranging from $12''$ to $60''$ from the center of the science target (Thatte et al. 2020).

We diligently searched for such essential NGS stars following the guidance outlined in N23, utilizing Gaia and SDSS archival databases, and showing them as the white crosses along with their H -band photometric AB magnitudes in Fig. 1 when available for each individual galaxy. For Sloan NGS, we converted their SDSS magnitude to AB magnitude following N23 section 2.1. However, for Gaia

⁵ The dataset Digital Object Identifier (DOI): [10.26131/IRSA441](https://doi.org/10.26131/IRSA441)

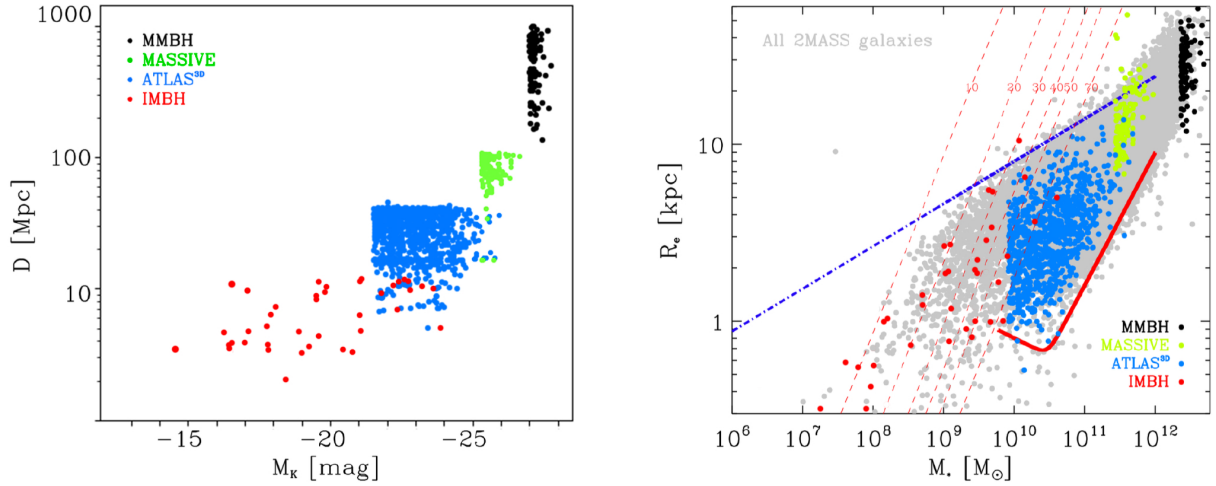


Figure 2. **Left:** Distance vs. absolute K_s -band magnitude (M_K) of the HARMONI IMBH sample (red; this work), MASSIVE survey (green; Ma et al. 2014), ATLAS^{3D} survey (blue; Cappellari et al. 2011), and MMBH survey (black; N23). There is a marginal overlapping (i.e. roughly 1.8 M_K mag or the stellar mass range of $10^{10} < M_* < 5 \times 10^{10} M_\odot$) of the HARMONI IMBH sample with the ATLAS^{3D} survey in these parameter spaces. We assumed $D \approx D_L \approx D_A$ for this HARMONI IMBH, ATLAS^{3D}, and MASSIVE surveys due to their low redshifts ($z < 0.025$), but the MMBH survey where $D \approx D_A \neq D_L$ due to its higher redshift ($z < 0.3$). Here, D_L and D_A are luminosity and angular-size distance, respectively. **Right:** The mass–size diagram of the 2MRS sources (grey dots) shows a wide range of stellar mass of $10^6 < M_* < 6 \times 10^{12} M_\odot$. The inclined-red-dashed lines are the constant-velocity dispersions (constant- σ_*) of 10, 20, 30, 40, 50, 70 km s⁻¹. The ATLAS^{3D} (full sample of Ellipticals + Spirals), MASSIVE, MMBH, and HARMONI IMBH samples occupy different regions of the diagram. The thick-solid red curve defines the zone of exclusion described by equation (4) of Cappellari et al. (2013b) in the previously explored stellar-mass range of $10^6 \leq M_* \leq 1 \times 10^{12} M_\odot$, while the thick dash-dotted blue line shows the relation ($R_e/\text{kpc} = 8 \times [M_*/(10^{10} M_\odot)]^{0.24}$), which provides a convenient approximation for the lowest 99% contour for the distribution of ETGs (Cappellari et al. 2013b). We should note that there are 56 out of 60 targets (left panel) and 46 out of 60 targets (right panel) are shown for our HARMONI IMBH sample due to the incomplete information on these relevant properties of the sample.

NGS, which uses the Vega magnitude system, we then converted it to the AB magnitude system by applying the Gaia data release 3 documentation, specifically section 5.5.1 titled “Photometric relationships with other photometric systems,” (Busso et al. 2022).

Roughly 60% of galaxies within our sample comfortably satisfy the tip-tilt star requirement for Laser Tomography Adaptive Optics (LTAO⁶) correction. In cases where galaxies lack NGS meeting the tip-tilt star criteria for LTAO correction, we suggest employing the NSCs themselves for open-loop AO correction (Krajinović et al. 2018b).

3 PROPERTIES OF THE HARMONI IMBH SAMPLE

3.1 Galaxy stellar mass and size

The left panel of Fig. 2 illustrates the distribution of our HARMONI IMBH sample (depicted as red dots) within the phase space of K_s -band absolute magnitude versus distance. This analysis confines the explored volume to a range of $2 \lesssim D \lesssim 10$ Mpc and encompasses a wide span of K_s -band absolute magnitudes, ranging from -13.3 to -23.3 mag. Consequently, the sample comprises a diverse set of nearby dwarf stellar systems, with stellar masses ranging from slightly above $2 \times 10^6 M_\odot$ to just under $5 \times 10^{10} M_\odot$. The plot also includes data from larger survey volumes, such as ATLAS^{3D} (Cappellari et al. 2011), MASSIVE (Ma et al. 2014) and MMBH (N23), for reference. This overlay emphasizes the distinct position of

the HARMONI IMBH survey sample within the hierarchy of galaxy structures, as it occupies the lowest permissible mass range for a stellar system.

In Section 2.1, we determined the galaxy photometric stellar masses based on the K -band luminosities, assuming a constant $M/L_K = 1 (M_\odot/L_\odot)$ (Nguyen et al. 2018). We also cross-verified the stellar masses for the HARMONI IMBH sample using an alternative formula from equation (2) of Cappellari (2013). This formula, calibrated from 260 ATLAS^{3D} early-type galaxies, is expressed as $\log(M_*) = 10.58 - 0.44 \times (M_K + 23)$. The differences between the two methods did not exceed 10%. In addition, the sizes of galaxies in the sample were estimated using $R_e = 1.61 \times j_r_eff$, where j_r_eff represents the 2MASS XSC keyword semimajor axis of the isophote enclosing half of the total galaxy light in the J -band (Cappellari et al. 2013b). The preference for using j_r_eff over k_r_eff was primarily due to the superior signal-to-noise ratio (S/N) of the J -band data in comparison to the equivalent K -band data (Cappellari et al. 2013a). However, we adopted $j_r_eff \equiv R_e$ as the size estimate only when it exceeded 1.5 kpc in cases where this information was not available in the literature. Otherwise, we relied on the values provided in the literature. The sample thus boats dwarf galaxies with an effective radius range of $0.3 < R_e \leq 5$ kpc.

3.2 Our IMBH sample on the mass–size diagram

We constructed a mass–size diagram (M_*-R_e) for the HARMONI IMBH sample based on the collected stellar masses and sizes. This diagram was then overlaid with data from the 2MRS sources before the application of selection criteria. Here, we removed all 2MRS galaxies those have $R_e < 3''$ because these R_e are unreliable (Section 2.1). The resulting plot, presented in the right panel of Fig. 2,

⁶ LTAO mode on the ELT/HARMONI instrument needs one NGS at least to work simultaneously with six other artificial off-axis Laser Guide Stars (LGS). The system brings the required NGS to be more than 10,000 times fainter than that from the classical AO used on Gemini and VLT.

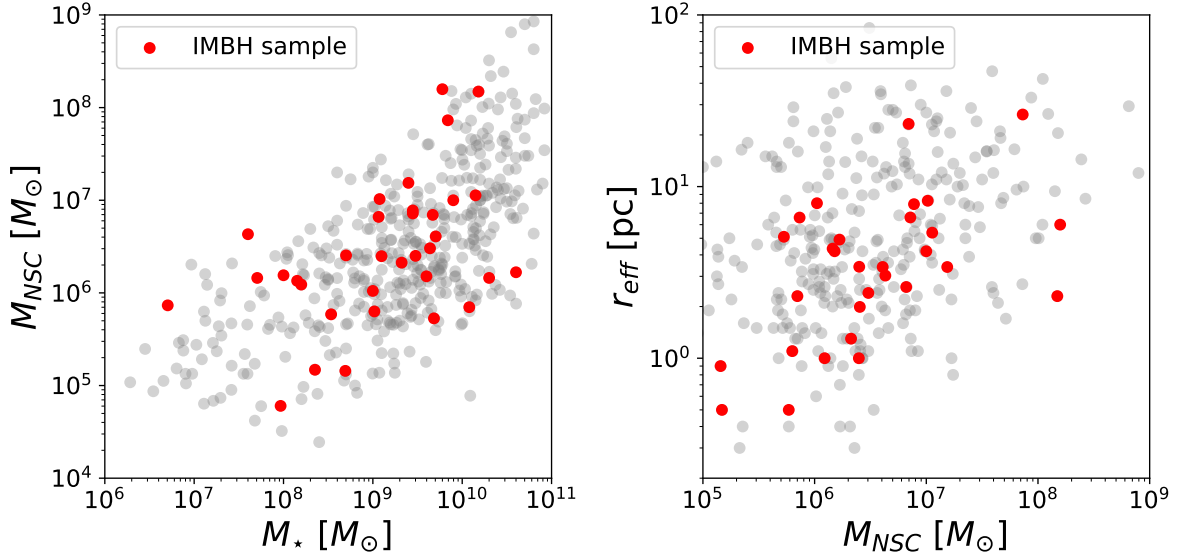


Figure 3. **Left:** The M_{\star} – M_{NSC} relation for galaxies in which galaxy and NSC masses are available regardless of their Hubble types. The compilation of dynamical and spectroscopically modeled NSC masses from Erwin & Gadotti (2012), Georgiev et al. (2016), Spengler et al. (2017), Ordenes-Briceño et al. (2018), and Sánchez-Janssen et al. (2019). **Right:** The M_{\star} – R_e relation for galaxies in which their NSC’s mass and effective radius are available. The data are taken from Walcher et al. (2005), Côté et al. (2006), Rossa et al. (2006), Erwin & Gadotti (2012), Norris et al. (2014), Georgiev et al. (2016), Spengler et al. (2017), Baldassare et al. (2022), and Fahrion et al. (2022).

reveals interesting trends. At lower masses ($M_{\star} < M_{\text{crit}} \approx 2 \times 10^{11} M_{\odot}$), the lines representing constant σ_{\star} (also indicating constant M_{BH}) trace the mass concentration and mass density (or bulge mass fraction) of galaxies. This suggests that the central M_{BH} of these galaxies behaves similarly to other galaxy properties. The evolution of SMBHs is thus linked to various factors, including optical color, molecular-gas fraction, dynamical– M/L , initial mass function (IMF) normalization, age, metallicity, and α -element abundance (fig. 22 of Cappellari 2016). Notably, their M_{BH} growth follows a similar trend to that of galaxy properties influenced by star formation within the host galaxies (Graham et al. 2018). We also added the ATLAS^{3D} (Cappellari et al. 2011), MASSIVE (Ma et al. 2014), and MMBH (N23) galaxies on this M_{\star} – R_e diagram to highlight the distinct distribution of this lowest mass and compact galaxies sample.

Our HARMONI IMBH sample spans an extensive range of galaxy masses, covering more than four orders of magnitude. It is worth noting that our sample distributes right below and fully consistent with the upper limit for dwarfs and spirals, the dashed blue line expressed as $(R_e/\text{kpc}) = 8 \times [M_{\star}/(10^{10} M_{\odot})]^{0.24}$. The sample distributes in a similar manner of the dwarfs in fig. 9 of Cappellari et al. (2013b), which is typically followed by 99% of early-type galaxies.

The properties of galaxies with masses exceeding $10^9 M_{\odot}$ tend to align with the constant σ_{\star} lines, implying that their M_{BH} may conform to the predictions of the M_{BH} – σ_{\star} relations (e.g. equation (2) of Krajnović et al. 2018a). Below this mass and due to the incompleteness at low M_{\star} and low R_e of the 2MASS survey, we have very little information of the relations among constant σ_{\star} , M_{\star} , and R_e (particularly those with $\sigma_{\star} < 30 \text{ km s}^{-1}$). Although, compare our HARMONI IMBH sample with the dwarfs sample in fig. 9 of Cappellari et al. (2013b) – which has properly R_e – it is clear that our HARMONI IMBH sample follows the expected distribution for dwarfs. Consequently, any relation among these parameters that have found based on the primary distribution of $\geq 10^9 M_{\odot}$ galaxies should

be stopped when the galaxy mass goes below this limit. However, recent observations (e.g. Nguyen et al. 2018, 2019; Greene et al. 2020, a review) suggested that black hole mass in these lower-mass galaxies does not follow to the established black hole–galaxy scaling relations, indicating the involvement of distinct mechanisms in the coevolution of these two crucial components at the low-mass regime.

The shift in the black hole–galaxy scaling relations, particularly in the low-mass regime, has prompted various explanations, as discussed in studies such as Mezcua (2017). However, a definitive answer remains elusive due to the limitations of our current observational capabilities in detecting these elusive IMBHs. The dependencies between M_{BH} and galaxy properties in this lower-mass range are challenging to discern with existing data. Our proposed sample of nearby IMBHs leverages the unique advantages of ELT/HARMONI, which offers exceptional angular and spectral resolutions as well as sensitivity. This initiative aims to overcome these challenges and potentially uncover new insights into the previously unexplored realms of IMBH and galaxy coevolution.

3.3 Nuclear star clusters and central massive black holes

Our HARMONI IMBH sample includes galactic nuclei with NSCs. Among them, 16 NSCs have known masses and effective radii falling within the ranges of $10^5 < M_{\text{NSC}} \lesssim 10^8 M_{\odot}$ and $3 < R_e < 27 \text{ pc}$, respectively. For the remaining NSCs, this information is unavailable. We have compiled data on these NSCs as well as their host galaxies’ properties in Table A1 in the supplementary material. In Fig. 3, we have plotted these NSCs alongside those obtained from literature sources, including both photometric and spectroscopic surveys.

Out of the 60 selected targets, two IMBHs have had their masses estimated through stellar kinematics, measured from marginally resolved VLT/SINFONI observations: NGC 5102 with an estimated mass of $\approx 9.1 \times 10^5 M_{\odot}$ and NGC 5206 with an estimated mass of $\approx 6.3 \times 10^5 M_{\odot}$ (Nguyen et al. 2018, 2019). Nguyen et al. (2022)

found a firm signature of an IMBH with a possible mass range of $3 \times 10^5 - 4.3 \times 10^6 M_{\odot}$ in the nucleus of NGC 3593 based on ALMA observation of circumnuclear CO(2-1)-molecular gas disc. Additional dynamical models presented in Neumayer & Walcher (2012) suggested that the IMBH in NGC 300, with kinematics measured from VLT/UVES spectra (Walcher et al. 2005), likely has a mass below $10^5 M_{\odot}$. Similarly, the IMBH in NGC 3621, with kinematics measured from the Echellette Spectrograph at the Keck Observatory (Barth et al. 2002), is estimated to have a mass below $3 \times 10^6 M_{\odot}$ (Barth et al. 2009).

In the regime of the dwarf galaxies with masses below $7 \times 10^9 M_{\odot}$, the behavior of the black hole mass–galaxy scaling correlations remain largely unconstrained. It strongly depends on the mass distribution of the currently elusive IMBH population found in the nearby universe (e.g. Mezcua 2017). Recent work by Nguyen et al. (2019) also provided evidence that the dynamical mass constraints of a sample of IMBHs within 3.5 Mpc, in a sample of five early-type galaxies, fall well below the predictions from the Kormendy & Ho (2013), Sahu et al. (2019a), and Greene et al. (2020) $M_{\text{BH}}-\sigma_{\star}$ relations.

3.4 Simulated targets

To explore the extreme ranges of observability, we created mock IFS observations with HSIM of two low-mass galaxies with NSCs: NGC 300, the closest, and NGC 3115 dw01, farther from Earth. These galaxies represent our IMBH survey’s overall characteristics.

NGC 300 is a spiral galaxy of type SA(s)d, characterized by a lack of a bulge (Bono et al. 2010) and inclined at an angle of $i = (42.3 \pm 3.0)^{\circ}$ (Kim et al. 2004) projected on the sky. Located approximately 2.2 Mpc away from us (Williams et al. 2013), this galaxy exhibits a steadily increasing size of its NSC from ultraviolet (UV) to infrared (IR) wavelengths (Carson et al. 2015). The NSC in NGC 300 possesses a central velocity dispersion $\sigma_{\star} = 13.3 \pm 2.0 \text{ km s}^{-1}$, as determined from high-resolution VLT/UVES spectroscopy ($R \approx 35,000$; Walcher et al. 2005), or $\sigma_{\star} = 13.3 \pm 0.3 \text{ km s}^{-1}$ when measured using high-resolution VLT/X-Shooter spectroscopy ($R \approx 11,000$; Kacharov et al. 2018). The NSC has a dynamical mass of $M_{\text{NSC}} \approx 10^6 M_{\odot}$ measured from VLT/UVES spectroscopy (Walcher et al. 2005). The galaxy has a total stellar mass of $2.2 \times 10^9 M_{\odot}$ (Kacharov et al. 2018).

The integration of Jeans Anisotropic Model (JAM) and the stellar kinematics measurements from the Walcher et al. (2005) high-resolution VLT/UVES spectroscopy found an $M/L_I \approx 0.6 (M_{\odot}/L_{\odot})$ and suggested an IMBH mass in the NGC 300’s NSC with an upper limit of $\approx 10^5 M_{\odot}$ (or $\approx 10\%$ of M_{NSC}), while their best-fit estimate is $\approx 10^2 M_{\odot}$ (Neumayer & Walcher 2012).

The star formation history (SFH) of NGC 300’s nucleus has been independently analyzed by Walcher et al. (2006) and Kacharov et al. (2018), utilizing different spectra, spectral ranges, and simple stellar population (SSP) models. Their findings reveal a relatively consistent picture of the stellar population. More than 50% of the stars in the nucleus formed over 5 Gyr ago, characterized by low metallicity ($[\text{Fe}/\text{H}] \sim -1$ dex). Subsequent star formation episodes involving young populations (around 10 Myr old) occurred until a few hundred million years ago, resulting in higher metallicity, eventually reaching values similar to solar metallicity about 1 billion years ago. Despite these later episodes, their contributions to the total light spectrum and mass remain modest, exceeding 10% and 1%, respectively. Remarkably, no evidence of emission lines in the spectra implies that the contribution of a very young population in NGC 300’s NSC is

likely from an extended horizontal branch (Conroy et al. 2018) or blue straggler stars (Schiavon 2007) in the nucleus.

NGC 3115 dw01 (PGC029300) falls under the classification of a dwarf elliptical galaxy (dE; Jerjen et al. 2000b; Parodi et al. 2002). Positioned at a distance of roughly 9.7 Mpc from our vantage point (Jerjen et al. 2000a,b; Karachentsev et al. 2004), this galaxy boasts a total stellar mass of $8.9 \times 10^8 M_{\odot}$ determined from its $B - V$ colour, and houses a substantial NSC with an effective radius of $6.61 \pm 0.09 \text{ pc}$ and a mass of $7.2 \times 10^6 M_{\odot}$, as gauged from *HST*/WFPC2 F814W images, resulting in a photometric $M/L_{\text{F814W}} \approx 1.4 (M_{\odot}/L_{\odot})$ (Pechetti et al. 2020). Kinematic assessments carried out at CTIO ($R \approx 10,000$), utilizing the 4 m telescope and its echelle spectrograph, yield a central velocity dispersion of $\sigma_{\star} = 32 \pm 5 \text{ km s}^{-1}$. However, measurements confined within the galaxy’s effective radius ($\approx 1.2 \text{ kpc}$) result in a value of around $\approx 45 \text{ km s}^{-1}$ (Peterson & Caldwell 1993).

Due to the absence of information regarding stellar populations and SFH in NGC 3115 dw01, as well as the galaxy’s morphology, we opted for simplicity in our HSIM IFS simulations. We employed Stellar Population Synthesis (SPS) spectra with a fixed age of 5 Gyr and Solar metallicity (z002) and inclination $i = 42^{\circ}$, which are similar to the nucleus of NGC 300.

4 DYNAMICAL MODEL

4.1 Jeans Anisotropic Model (JAM)

Our HARMONI IMBH sample comprises dwarf galaxies hosting bright NSCs with significant rotational characteristics (e.g. Seth et al. 2008, 2010; Nguyen et al. 2018; Thater et al. 2023). Notably, a considerable fraction of NSCs exhibits substantial rotation, as evidenced by the V/σ_{\star} ratio falling within the range of 0.1 to 0.6 (fig. 3 of Pinna et al. 2021), indicating their tendency toward cylindrical projections (Cappellari 2016). Consequently, we generated mock kinematics using a dynamical model based on the solution of the Jeans equations. Our model assumed axisymmetry with a cylindrical alignment of the velocity ellipsoid, providing a robust approximation for a broad spectrum of dynamics, encompassing both fast and slow rotators (Cappellari 2008). This model was implemented as JAM_{cyl} and was used to predict the mean velocity. In doing so, we assumed a model in which the velocity ellipsoid was axially symmetric around the vertical direction ($\sigma_z \neq \sigma_r = \sigma_{\phi}$). This choice aligns with the cylindrical limit and is particularly suitable for modeling the expected rotators of NSCs. This assumption was achieved by setting `align='cyl'` in the JAM_AXI_PROJ procedure of JAMPY⁷ package (Cappellari 2020).

4.2 Predicted velocity dispersion profiles

Before presenting detailed simulations of the predicted kinematics due to IMBHs of different masses in NSC, here we try to understand the quantitative behaviour we should expect. This is particularly important in this paper because we have to decide how to extrapolate the inner surface brightness profile of NSCs, at radii much smaller than resolvable with *HST*.

In their classic paper, Tremaine et al. (1994) studied the qualitative behaviour of the projected velocity dispersion (σ_p) profiles in elliptical galaxies with central SMBHs. They described the predicted velocity-dispersion profile of isotropic galaxy models described by a double power-law density profile, with general inner

⁷ jampy v7.2.0; available from <https://pypi.org/project/jampy/>

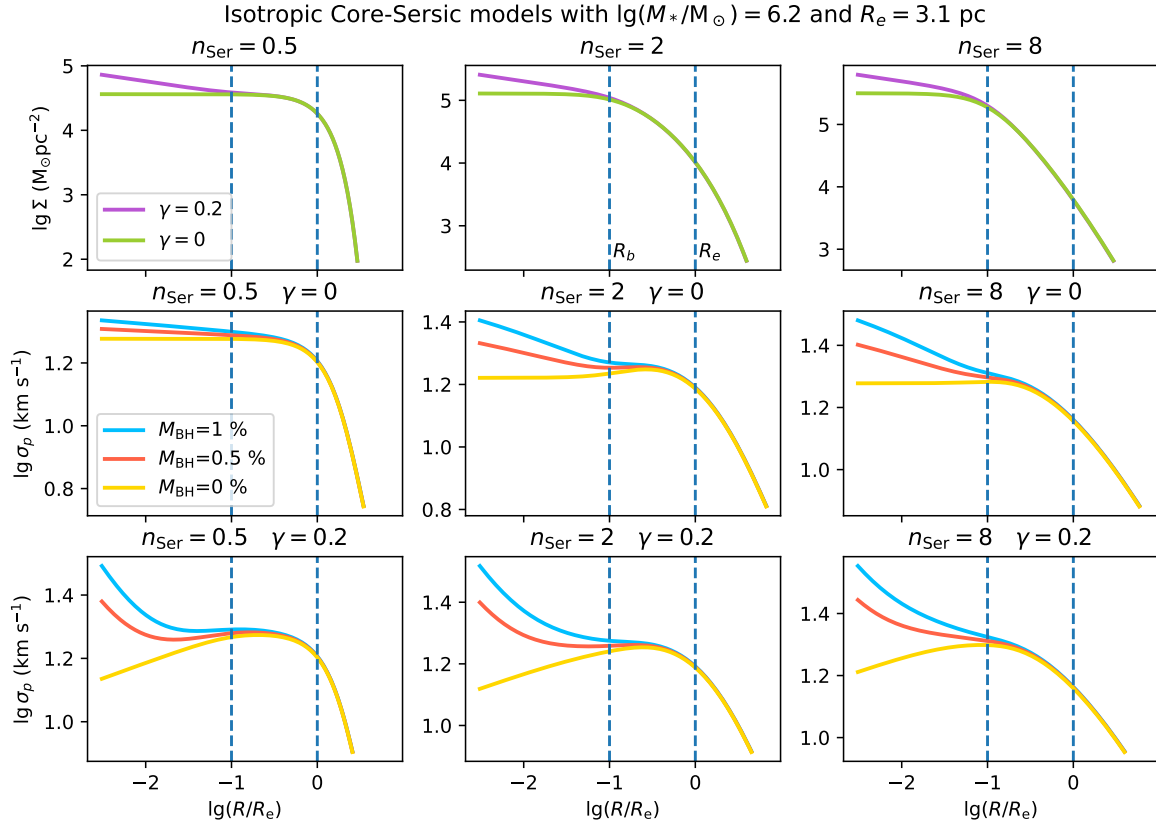


Figure 4. Atlas of the central surface-mass density (Σ , the three top-row panels) and projected velocity dispersion (σ_p), the three middle-row and bottom-row panels) profiles resolved deeply into the resolvable region of ELT/HARMONI, which are predicted by various values of the Sérsic index (n_{Ser}) and the core inner slope (γ) of the isotropic Core-Sérsic model. These theoretical profiles can be used to describe the qualitative behaviour of the σ_p of stellar systems spanning from galaxies to NSC. However, for illustration, the values of Σ and σ_p were normalized to approximate the median values of the mass and radii of NSC (see text). We utilized three different Sérsic indices – including the low $n_{\text{Ser}} = 0.5$ (corresponding to the Gaussian profile), intermediate $n_{\text{Ser}} = 2$, and high $n_{\text{Ser}} = 8$ of the Sérsic-index value – and two different values of the core inner slope: $\gamma = 0$ (green line) and $\gamma = 0.2$ (purple line). To illustrate the effects of central IMBHs having at the central region of the projected velocity dispersion profiles, we modeled with three different black hole masses: $M_{\text{BH}} = 0\%$ of M_{NSC} (no black hole, yellow line), $M_{\text{BH}} = 0.5\%$ of M_{NSC} (or $M_{\text{BH}} = 8 \times 10^3 M_\odot$, red line), and $M_{\text{BH}} = 1\%$ of M_{NSC} (or $M_{\text{BH}} = 1.6 \times 10^4 M_\odot$, blue line). The two vertically dashed lines represent the break radius (R_b , inner line) and the effective radius (R_e , outer line) of the NSC’s isotropic Core-Sérsic model. The core inner slope γ control the inner behaviour of the central surface-mass density and the projected velocity dispersion profiles, while the Sérsic index describes the outer profile.

density $\rho(r) \propto r^{-\gamma}$ and fixed outer density $\rho(r) \propto r^{-4}$ (Dehnen 1993), and a smooth transition between these two power-law regimes. Here, γ is the power-law index.

Here, we illustrate the behaviour of the velocity dispersion for the more general Core-Sérsic model (Graham et al. 2003; Trujillo et al. 2004), which parametrizes the projected surface brightness (not the intrinsic density) as follows

$$I(R) = I' \left[1 + \left(\frac{R_b}{R} \right)^\alpha \right]^{\gamma/\alpha} \exp \left[-b_{n_{\text{Ser}}} \left(\frac{R^\alpha + R_b^\alpha}{R_e^\alpha} \right)^{1/(\alpha n_{\text{Ser}})} \right] \quad (1)$$

where

$$I' = I_b 2^{-\gamma/\alpha} \exp \left[b_{n_{\text{Ser}}} 2^{1/(\alpha n_{\text{Ser}})} \left(\frac{R_b}{R_e} \right)^{1/n_{\text{Ser}}} \right]$$

and $b_{n_{\text{Ser}}}$ is a function of the various parameters (n_{Ser} , α , γ , R_b , and R_e) that can be determined by solving the relation (A10) of Trujillo et al. (2004) when the enclosed luminosity at R_e is equal to half of the total luminosity, $2L(R_e) = L_T$. In numerical practice, Ciotti & Bertin (1999) use the asymptotic expansion theorem for the $1/R^n$ law to solve for $b_{n_{\text{Ser}}}$ as an analytical function of the Sérsic index n_{Ser}

as $b_{n_{\text{Ser}}} = 2n_{\text{Ser}} - \frac{1}{3} + \frac{4}{405n_{\text{Ser}}} + \frac{46}{25515n_{\text{Ser}}^2} + \mathcal{O}\left(\frac{1}{n_{\text{Ser}}^3}\right)$. Here, n_{Ser}

is the Sérsic index, which controls the shape of the outer Sérsic part. R_e is the effective radius of the profile. R_b is the break radius, which is the point at which the surface brightness changes from the outer Sérsic part to the inner power-law regime of the profile. I_b is the intensity at the break radius (converted to surface-brightness μ_b in Table 4). α is the sharpness parameter that controls the sharpness of the transition between the outer Sérsic and inner power-law regimes.

Outside the inner break at radius $R = R_b$ this is a Sérsic (1968) profile of projected half-light radius R_e , but gradually transitions to a power law surface brightness $\Sigma(R) \propto R^{-\gamma}$ at smaller radii $R \ll R_b$.

We adopt the Core-Sérsic profile because it can describe the profile of real NSCs. However, we allow for a cusp in the inner slope to parametrize our ignorance of the profile of NSC at radii which are inaccessible with current instruments, but which will become observable with the ELT. In our analysis, we model the NSC in isolation, even though they are embedded in the large-scale gravitational potential of the host galaxy. However, the latter has an insignificant effect on the predicted σ_p profiles at the centre of the NSC. In par-

ticular, in our case, R_e represents the size of the NSC, not the size of the host galaxy.

To compute the predictions for the σ_p profiles we first used the `MGE_FIT_1D` procedure in the `MGEFIT` package⁸ (Cappellari 2002) to fit the Core-Sérsic profiles in the range $R_b/100 < R < 20R_e$ using 20 Gaussians. Then used the `JAM_SPH_PROJ` procedure in the `JAMPY` package (see footnote 7; Cappellari 2008, 2020) to compute the isotropic velocity dispersion for different values of the Sérsic index n_{Ser} and the core inner slope γ . In all our tests we adopted a fixed $\alpha = 2$ value, which produces a smooth transition between the outer Sérsic and inner power-law profiles. We show the results in Fig. 4. The qualitative behaviour of the profiles is independent of the absolute normalization of their total masses M_\star and R_e . It can be applied unchanged to describe the σ_p profile of NSC or giant elliptical galaxies. However, in this Fig., we adopt as mass and size reference the values $\lg(M_{\text{NSC}}/M_\odot) = 6.2$ and $R_e = 3.1$ pc. These are the median values for NSC of late-type galaxies with $M_\star < 10^9 M_\odot$ (Neumayer et al. 2020, table 2).

In Fig. 4, we adopt either no black hole, or black hole masses of 0.5% and 1% of the mass of the NSC. These values are the same characteristic fractions observed for normal galaxies (Kormendy & Ho 2013, eq. 11). However, nothing is currently known about the mass of IMBH in NSC. In fact, NSCs may not have IMBHs at all, or they may be dominated by the IMBH mass. But the qualitative behaviour remains unchanged.

For $\gamma > 0$ and without black holes the σ_p profile decreases towards the nucleus, regardless of n_{Ser} . This is a well-known general feature of realistic galaxy models. It appeared in puzzling contrast with the early observations (Binney 1980) until it became clear that all massive galaxies contain SMBHs. With an IMBH, the σ_p profile starts increasing towards the centre, inside the IMBH's SOI, asymptotically approaching the Keplerian rise $\sigma_p \propto R^{-1/2}$ (for $0 < \gamma < 2$), regardless of the profile slope, as shown by Tremaine et al. (1994, eq. 52).

Tremaine et al. (1994) also pointed out that⁹, when $\gamma = 0$, namely when the inner surface brightness approaches a constant value, the asymptotic behaviour becomes qualitatively different. In that case, without an IMBH, the σ_p profile approaches a constant positive value, instead of dropping towards zero. We confirm the behaviour for the Core-Sérsic profile with a flat inner core regardless of n_{Ser} . With an IMBH, the σ_p profile rises towards the centre, but it does so less steeply than the $\gamma > 0$ case, as predicted for the double power-law models.

What is new in this study is the fact that we explore a range of Sérsic indices, including the extreme case $n_{\text{Ser}} = 1/2$, which corresponds to a Gaussian profile, when $\gamma = 0$. We find that in this extreme situation, the σ_p profile becomes only weakly sensitive to the black hole mass. This is quite important for the present study, because we are approximating the surface brightness of the NSC using the multi-Gaussian expansion (MGE) method (Emsellem et al. 1994). And we are fitting photometric data that have a much lower resolution than the one we will be able to obtain with the ELT. This implies that our model may end up being described by a Gaussian in the central parts, well inside the width of the PSF of our photometry. This is precisely the key region, near the black hole, where we want to produce an accurate σ_p prediction.

In practice, we should not worry about NSC having flat surface

brightness profiles and isotropic orbital distributions. This is because such models are unphysical and cannot exist in real stellar systems. Instead, if an IMBH is present, isotropic models produce a density cusp that rises as $\rho(r) \propto r^{-1/2}$ near the black hole (Tremaine et al. 1994), or $\Sigma(R) \propto R^{-3/2}$ in surface brightness (see also van der Marel 1999). One would require extreme tangential anisotropies for flat profiles $\gamma = 0$ to be allowed, as indicated by the cusp-slope vs central anisotropy theorem (An & Evans 2006). We have no reason to think NSC satisfies this requirement. However, what is important is that, lacking real high-resolution photometry at the resolution of HARMONI, we extrapolate the observed surface brightness using a non-zero inner power slope, when constructing the mock kinematics of the NSCs. Failing to do so, we would generate predictions for σ_p profiles that vastly underestimate the central rise that we expect from high-resolution HARMONI observations.

4.3 MARCS synthetic library of stellar spectra

To create mock HSI IFS simulations, we required stellar population synthesis (SPS) spectra¹⁰ that contain information about the stellar populations (Maraston & Strömbäck 2011), based on the Model Atmospheres with a Radiative and Convective Scheme (MARCS) synthetic library of theoretical spectra, originally developed by Gustafsson et al. (2008). Although MARCS synthetic library spectra are not as reliable as an empirical stellar library, it offers broad wavelength coverage spanning from 1,300 Å to 20 μm, high spectral resolution with $\sigma = 6.4$ km s⁻¹ (equivalent to $R = \lambda/\Delta\lambda \sim 20,000$), and fine sampling with 100,724 flux points ($\Delta\lambda \approx 0.065$ Å). We assumed a Salpeter IMF, an age of 5 Gyr, and Solar metallicity (z002) for both NGC 300's NSC (Kacharov et al. 2018) and NGC 3115 dw01 (Section 3.4). The SPS spectra were truncated within the wavelength range of 1.0–2.5 μm to match the HARMONI/J, H, K, H-high, K-short, and K-long gratings.

5 GALAXY PHOTOMETRY MODELS

5.1 HST images and their PSF models

The *HST*/Wide Field and Planetary Camera 2 (WFPC2) Planetary Camera (PC) imaging details utilized in this study are provided in Table 3. Specifically, the nucleus of NGC 300 was observed on May 6, 2001, using the PC1 chip with the F814W filters. These observations comprised three exposures, each lasting 213 seconds. Similarly, the nucleus of NGC 3115 dw01 was observed on November 29, 1995, employing the PC1 chip with both F547M and F814W filters. These observations consisted of one and two exposures, each lasting 160 seconds, for the F547M and F814W filters, respectively. The data were obtained under Project ID 8599 (PI: Boeker) for NGC 300 and Project ID 5999 (PI: Phillips) for NGC 3115 dw01. We accessed the reduced and drizzled images from the *HST*/Hubble Legacy Archive (HLA), with a pixel scale of $0''.045$.

For our analysis, it was imperative to meticulously characterize the PSFs used to deconvolve the *HST* profiles into their intrinsic forms (Section 5.2). To achieve this, we generated simulated images of the *HST*/WFPC2 PSFs in each filter using `tiny1` and `tiny2` routines within the `Tiny Tim` software package (Krist 1995; Krist et al. 2011), which creates a model *HST* PSF based on the instrument, detector chip, detector chip position, and filter used in the observations. To ensure that the model PSFs were processed in the same

⁸ v5.0 of the Python package from <https://pypi.org/project/mgefit/>

⁹ Tremaine et al. (1994) studied densities $\rho(r) \propto r^{-\gamma'}$, which we convert to the corresponding surface brightness $\Sigma(R) \propto R^{-\gamma}$ using $\gamma = \gamma' + 1$.

¹⁰ Available from <https://marcs.astro.uu.se/>

Table 3. *HST*/WFPC2 PC (PC1) observations (1 pixel = 0''045) of the two galaxies hosting NSCs chosen to perform HISM simulations

Galaxy name	α (J2000) (h:m:s)	δ (J2000) (°:':")	UT Date	PID	PI	Filter	Exptime (s)	Zeropoint (mag)	A_λ (mag)	PSF (arcsec)
(1)	(2)	(3)	(4)	(5)	(6)	(7)	(8)	(9)	(10)	(11)
NGC 300	50:54:53.477	-37:41:03.31	2001 May 06	8599	Boeker	F814W	3 × 213	23.758	0.025	0.101
NGC 3115 dw01	10:05:41.599	-07:58:53.40	1995 Nov. 29	5999	Phillips	F814W	2 × 160	23.758	0.050	0.102
	10:05:41.599	-07:58:53.40	1995 Nov. 29	5999	Phillips	F547M	1 × 160	23.781	0.025	0.097

Notes: Column 1: The galaxy name. Columns 2 and 3: The galaxy's position (R.A. and Decl.) from *HST*/HLA and MAST data. Column 4: The date when observations were performed. Columns 5 and 6: The project (PID) and principal investigator (PI) identification numbers. Column 7: The board-band filter used to take the data. Column 8: The exposure times of the observations show the number of exposures multiplied by the time spent on source for each exposure. Columns 9 and 10: The photometric zero-point and extinction value in each filter. Column 11: The FWHM of the final simulated PSF obtained from Section 5.1.

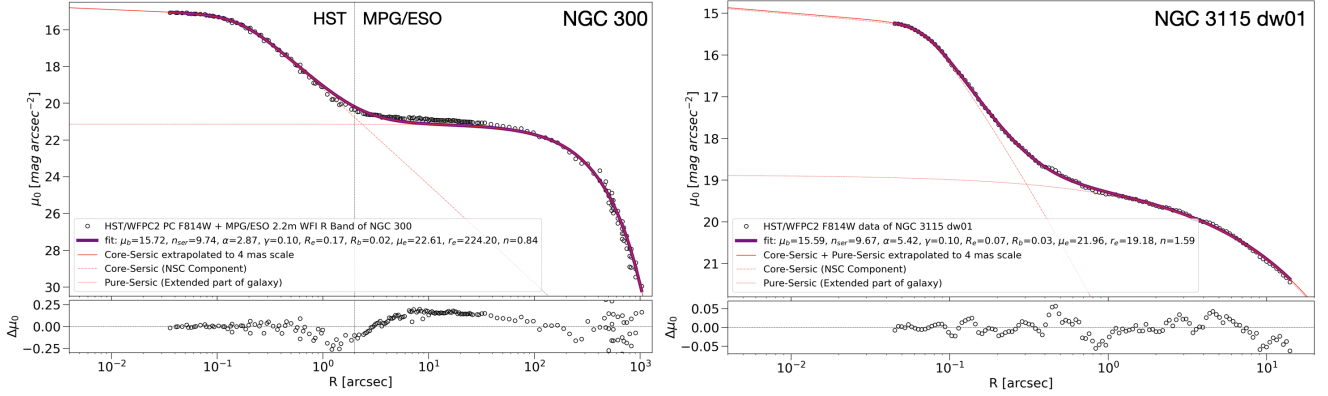


Figure 5. Upper panels: The insert *HST*/WFPC2 F814W (calibrated with the same *HST* profile from Carson et al. (2015)) + large-scale MPG/ESO 2.2-m *R* band (taken from Neumayer et al. (2020)) surface brightness profiles of the galaxy NGC 300 (left) and NGC 3115 dw01 (right) constructed directly from IRAF ellipse (open black dots). All magnitudes are corrected for foreground extinction. The best-fit Core-Sersic + pure-Sersic surface brightness profiles of these IRAF ellipse are plotted in purple solid-thick lines, and their best-fitting parameters are shown in the legend. Here, the Core-Sersic profile is plotted in a red dashed line, while the pure-Sersic profile is depicted in a red dotted line. We should note that within the radii of 0''045, these profiles are extrapolated to the 4 mas scale required for this IMBH survey's imaging with ELT/MICADO (red solid-thin lines). Lower panels: The differences (or residuals (data - model)) between the IRAF ellipse surface brightness profiles and their corresponding best-fit Core-Sersic + pure-Sersic models illustrate the fit's goodness.

Table 4. Best-fit Core-Sersic + pure-Sersic parameters of the *HST*/WFPC2 surface brightness profiles of NGC 300 and NGC 3115 dw01. We fixed $\gamma = 0.1$

Galaxy name	Filter	μ_b (mag/arcsec ⁻²)	n_{Ser}	α	R_e (arcsec)	R_b (arcsec)	μ_e (mag/arcsec ⁻²)	r_e (arcsec)	n
(1)	(2)	(3)	(4)	(5)	(6)	(7)	(8)	(9)	(10)
NGC 300	F814W	15.72 ± 0.22	9.74 ± 0.05	2.87 ± 0.05	0.17 ± 0.03	0.02 ± 0.01	22.61 ± 0.45	224.20 ± 1.52	0.84 ± 0.11
NGC 3115 dw01	F814W	15.59 ± 0.21	9.67 ± 0.05	5.42 ± 0.12	0.07 ± 0.02	0.03 ± 0.01	21.96 ± 0.20	19.18 ± 0.25	1.59 ± 0.07
	F547M	16.44 ± 0.25	9.51 ± 0.06	5.27 ± 0.15	0.06 ± 0.02	0.03 ± 0.01	23.01 ± 0.24	18.73 ± 0.27	1.71 ± 0.05

Notes: Column 1: The galaxy name. Column 2: The board-band filter used to take the data. Columns (3–7): The best-fit parameters of the Core-Sersic profile for the NSC components, orderly the surface brightness density at the break radius, the Sérsic index of the outer Sérsic part, the sharpness parameter which indicates how fast/slow the profile changes from the outer Sérsic to inner power-law regime, the break radius where the profile changes from the outer Sérsic part to the inner power-law part of the profile, and the effective radius of the outer Sérsic part of the profile. Columns (8–10): The best-fit parameters of the pure-Sersic profile for the galaxies' extended parts, orderly the surface brightness density at the effective radius, the effective radius, and the Sérsic index.

way as the *HST* images, we produced individual versions of each PSF corresponding to their realistic exposure in each filter and each galaxy on a subsampled grid with sub-pixel offsets, using the same four-point box dither pattern as the *HST*/WFPC2 exposures. Next, in order to account for the effect of electrons leaking into neighbouring pixels on the CCD, each model PSF was convolved with the appropriate charge diffusion kernel. The same filters set of PSFs of each galaxy were then combined and resampled onto a final grid with a pixel size of 0''045 using Drizzlepac/AstroDrizzle (Avila et al. 2012). The FWHM information for these ultimate PSF models is provided in Table 3.

5.2 Surface brightness profiles and galaxy mass models

The *HST* data, summarized in Table 3, served as the basis for our measurements of the galaxies' surface-brightness profiles. We conducted fits to analytical functions and extrapolated these profiles using the best-fit parameters obtained from these fits, under certain assumptions adequate for presenting the simulations and dynamical models.

Our initial step involved extracting radial surface brightness profiles of the observed stars. For NGC 300, this was accomplished in the F814W filter, while for NGC 3115 dw01, data from both the F814W and F547M filters were used. We employed the Image Reduction and Analysis Facility (IRAF) ellipse task (Jedrzejewski 1987) to conduct this task. The ellipse routine systematically in-

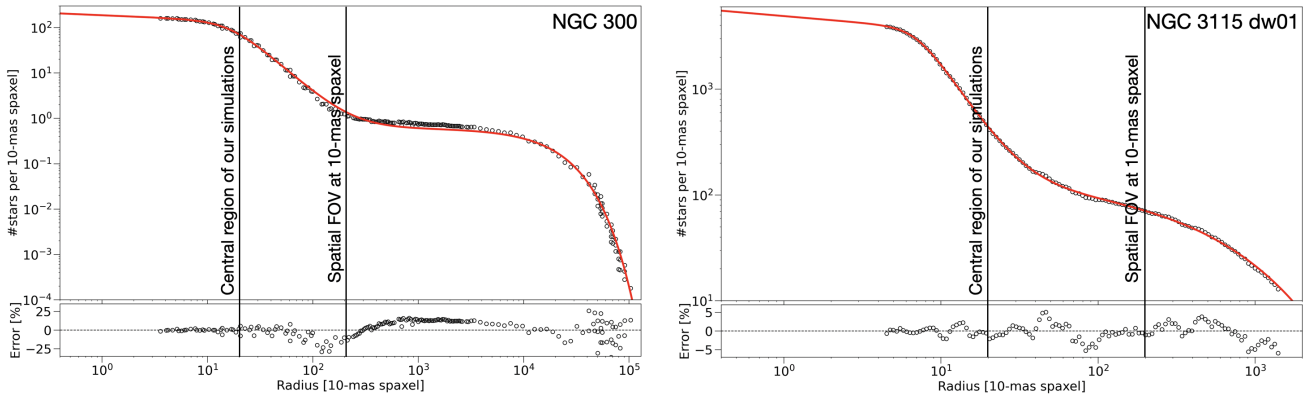


Figure 6. In the upper panels of the figure, we present the estimated number of stars per 10 mas spaxel for the nucleus of NGC 300 (left) and NGC 3115 dw01 (right). These data points, shown in black, are derived directly from the surface brightness profiles in Fig. 5, specifically from the *HST*/WFPC2 F814W observations. However, the large-scale MPG/ESO 2.2-m *R* band of NGC 300 are taken from Neumayer et al. (2020). The lower panels of the figure display the residuals, calculated as (data – mode), which provide a representation of the relative error in our estimation, helping to assess the accuracy of our calculations. The inner vertical solid line represents our spatially central regions of HARMONI simulations in Section 6.2 ($0''.4 \times 0''.4$), while that same outer line illustrates the full spatial FOV of HARMONI at our chosen 10-mas spaxel survey ($2''.15 \times 1''.54$; see Zieleniewski et al. 2015).

tegrated the flux of stars within concentric annuli, allowing for variations in position angles and ellipticities along the semi-major axis of the galaxy. Notably, fixing both position angles and ellipticities did not yield any significant changes in our results (Nguyen et al. 2022). To obtain the inherently radial profiles in IRAF, we initiated spatial imaging deconvolution using simulated images of the *HST*/WFPC2 Tiny Tim PSF generated in Section 5.1. Subsequently, we converted the average flux within each annulus, measured in counts/s, into surface brightness expressed in mag arcsec⁻². This conversion was carried out using the photometric information derived from the broad-band filters and camera specifications, as provided in Table 3. The large-scale profile of NGC 300 ($\mu_0(r > 2'')$) was taken from its Wide Field Imager (WFI) observed in *R* band with the MPG/ESO 2.2-metre telescope, which presented in Neumayer et al. (2020) and is available at <https://www.eso.org/public/images/eso1037a/>. Here, we also calibrated our inset *HST*/WFPC2 F814W profile ($\mu_0(r \leq 2'')$) with the same *HST* profile from Carson et al. (2015) using the AB magnitude system.

Next, we applied analytical functions to fit these inherently radial surface-brightness profiles of NGC 300 and NGC 3115 dw01. These functions involved combinations of a Core-Sérsic model (Graham et al. 2003; Trujillo et al. 2004) and a pure-Sérsic model (Sérsic 1968). Here, while the Core-Sérsic model is used to fit the NSC component, the pure-Sérsic model was applied to fit the extended component of the galaxy. This approach was adopted due to the morphological complexity revealed by the high-resolution *HST* and wide-field MPG/ESO observations of galaxies, which often exhibit multiple components like NSCs, bulges, disks, bars, and a constant sky/galaxy background. This detailed morphological inspection is also useful to tell us what Sérsic index (n_{Ser}) best fits these cores and predict the kinematics trend (see Section 4.2). Furthermore, the pixel size of the *HST*/WFPC2 is 45 mas. This means that a single pixel contains over 20 spaxels of the proposed 10 mas mode adopted for this HARMONI IMBH survey. In fact, it is more than 11 times larger than the pixel size for ELT/MICADO images (i.e. 4 mas). We thus have no clue of the stellar information at this scale, and this region is indeed embedded deeply in the core of an NSC, which is controlled by the power-law behaviour of the Core-Sérsic model. In this work, we adopted the power-law index $\gamma = 0.1$ as in N23 for both galaxies,

although our tests with varying γ provide $\gamma = 0.08$ for NGC 300 and $\gamma = 0.13$ for NGC 3115 dw01. Here, the Sérsic (1968) pure-Sérsic model has a form:

$$I(R) = I_e \exp \left\{ -b_n \left[\left(\frac{R}{r_e} \right)^{1/n} - 1 \right] \right\} \quad (2)$$

In which, we denoted n is the Sérsic index of the pure-Sérsic profile to distinguish with that n_{Ser} of the Core-Sérsic profile in equation (1), which controls the degree of curvature of the profile. An additional benefit of employing the pure-Sérsic model for the extended component of a galaxy is that, when $n = 0.5$, the model simplifies to a Gaussian profile. Similarly, for $n = 1$, the model represents an exponential profile, and for $n = 4$, it corresponds to the de Vaucouleurs profile. And again, the coefficient b_n is approximately as $b_n = 2n - 1/3$. r_e is the effective radius of the profile. I_e is the intensity at r_e , which is converted to surface-brightness density μ_e shown in the legends of Fig. 5 and Table 4.

We applied a non-linear least-squares algorithm using the Python MPFIT¹¹ function (Markwardt 2009) to iteratively fit the combined function of a Core-Sérsic and a pure-Sérsic above for both for NGC 300 and NGC 3115 dw01 to their corresponding spatially deconvolved profiles, thereby obtaining the best-fit parameters homogeneously. After the fits, we extrapolated the best-fit surface brightness profiles towards the galaxies' centres to a scale of 4 mas required for this IMBH survey's imaging with ELT/MICADO, as demonstrated in Fig. 5. The best-fit parameters and their associated uncertainties derived from these surface brightness profile fits are meticulously documented in Table 4.

Next, we employed these derived parameters to reconstruct the two-dimensional (2D) luminosity density models extrapolated towards the central 4 mas for each galaxy. During which, we assumed a small flattening based on the fact that not all NSCs are likely perfectly spherical and non-rotating, characterized by the ratio between the semiminor and semimajor axes $q' = b/a \approx 0.9$. This assumption also works for the extended bulge or disk of NGC 3115 dw01 as the galaxy morphology looks round through its *HST* observations. However, the extended scale of NGC 300 revealed through the MPG/ESO

¹¹ Available from <http://purl.com/net/mpfit>.

2.2-m WFI R band image suggests the galaxy's outer part ($r > 2''$) can be approximately assumed as $q' = b/a \approx 0.75$. Subsequently, we transformed these 2D luminosity density models into multiple Gaussian functions using the multi-Gaussian expansion (MGE) method (Emsellem et al. 1994; Cappellari 2002). This involved using the `MGE_FIT_SECTORS` routine from the `MGEFIT` package (see footnote 8; Cappellari 2002) and encompassed 15 Gaussians spanning radii from 4 mas to approximately $1000''$ for NGC 300 and $15''$ for NGC 3115 dw01, respectively. Detailed information regarding these MGEs can be found in Table A2 in the supplementary material.

Finally, we converted the luminosity surface density into mass surface density by assuming a constant mass-to-light ratio, $M/L_{F814W, \text{dyn}} \approx M/L_I \approx 0.6 (M_\odot/L_\odot)$ for NGC 300 (Neumayer & Walcher 2012) and $M/L_{F814W} \approx M/L_I \approx 1.4 (M_\odot/L_\odot)$ for NGC 3115 dw01 derived in AB mag (Pechetti et al. 2020). This stellar mass component was subsequently combined with an IMBH represented as a point mass. It is pertinent to mention that throughout our work, we disregarded (1) potential variations in M/L_I due to differences in stellar populations (e.g. Mitzkus et al. 2017) and (2) the distribution of dark matter halos (Navarro et al. 1996). Our focus remained exclusively on the stellar kinematics within the central part of $0''.4 \times 0''.4$ of HARMONI field-of-view (FOV), where the central black hole's and NSC's potential is the dominant factor.

5.3 Discrete stars

Given our HARMONI IMBH survey's proposed 10-mas spaxel angular resolution, it's crucial to ensure that we have a sufficient number of stars within a single spaxel for reliable statistical estimates. This issue becomes more significant for the closest targets. To address this, we carefully investigated the number of stars within a 10-mas spaxel based on the surface brightness profile presented in Fig. 5. First, we converted the surface brightness density (in mag arcsec⁻²) into surface luminosity density (in L_\odot arcsec⁻²). Then, we accounted for the size of the 10-mas spaxel to calculate the average number of stars.

Fig. 6 illustrates our estimated number of stars per 10-mas spaxel as a function of radius from the centre for NGC 300 and NGC 3115 dw01, one of the closest and furthest target galaxies in our HARMONI IMBH sample, respectively. For NGC 300, the number of stars per 10-mas spaxel decreases from approximately more than 100 stars at the centre to around one star at radii larger than 200 spaxels (equivalent to $2''.15$, the FOV of our HARMONI IMBH survey with 10-mas spaxel). Similarly, for NGC 3115 dw01, the number of stars per 10-mas spaxel decreases from approximately 5000 stars at the centre to around 700 stars within the FOV of our HARMONI IMBH survey. In the extreme case of the closest and easiest to be resolved and within our measuring $0''.4 \times 0''.4$ central region, NGC 300 maintains from approximately 100 stars per 10 mas spaxel, validating our methodology. We should also note that this matter of number of stars per 10 mas spaxel is only critical for a few central spaxels because we will Voronoi bin (see footnote 13, Section 6.3) several spaxels together at larger radii to have enough numbers of stars within spatial bins for integrated light method of the stellar orbits superposition.

6 HARMONI IFS SIMULATIONS

First, we describe the HARMONI instrument on ELT and HARMONI Simulator (HSIM) in Section 6.1. Next, we combine the mass models of NGC 300 and NGC 3115 dw01 constructed in Section 5

with HSIM to simulate their J ($1.046 - 1.324 \mu\text{m}$), H ($1.435 - 1.815 \mu\text{m}$), K ($1.951 - 2.469 \mu\text{m}$), H -high ($1.538 - 1.678 \mu\text{m}$), K -short ($2.017 - 2.201 \mu\text{m}$), and K -long ($2.199 - 2.400 \mu\text{m}$) mock datacubes in Section 6.2. Finally, we present their extracted kinematics in Section 6.3.

6.1 HARMONI instrument and HSIM simulator

HARMONI, an instrument poised to be one of the pioneers of ELT, will usher in a new era of optical and NIR wavelength IFS ranging from 0.458 to $2.469 \mu\text{m}$. Distinguished by its versatile capabilities, HARMONI offers IFS at four distinct spatial scales (i.e. 4×4 , 10×10 , 20×20 , and $30 \times 60 \text{ mas}^2$) and three spectral resolving powers (i.e. $\lambda/\Delta\lambda \approx 3, 300, \approx 7,100$ and $\approx 17,400$) through an array of 13 gratings. Assisted by the ingenious design incorporates 798 hexagonal segments, each approximately 1.4 meters across, spanning a field of 39 meters of the ELT, HARMONI possesses the remarkable capability to gather spectral data from a vast field of 152×214 spaxels (equivalent to $\approx 32,530$ spectra) equipped with laser guide star AO.

This extraordinary technical prowess positions HARMONI as an ideal instrument for unveiling the elusive population of IMBHs residing in nearby dwarf galaxies, stellar clusters such as NSCs, and extragalactic GC (Zieleniewski et al. 2015; Garcia-Lorenzo et al. 2019). Notably, a previous study (N23) demonstrated that HARMONI could robustly measure the masses of SMBHs at distances of up to 1 Gpc ($z \lesssim 0.3$) within a mere hour of exposure time.

HARMONI's versatility extends to a wide range of scientific endeavours, from diffraction-limited imaging to ultrasensitive observations. Its capabilities encompass the study of morphology, spatially resolved populations and kinematics, abundances, and line ratios in distant sources, even in regions of faint surface brightness (Thatte et al. 2016). For an in-depth understanding of the instrument, readers can refer to the comprehensive description provided by Thatte et al. (2020) and explore further details on the HARMONI webpage¹². HARMONI's arrival heralds a new chapter in astronomical observation, promising groundbreaking insights across various fields of astrophysics and significantly advancing our understanding of the cosmos.

Zieleniewski et al. (2015) introduced HSIM, a sophisticated pipeline designed for simulating observations with the HARMONI instrument on ELT. This software takes as input high spectral and spatial resolution IFS cubes devoid of random noise, generated as described in Section 6.2, and incorporates the physical properties of celestial targets to generate simulated data cubes. Throughout the simulation process, HSIM meticulously factors in the complex atmospheric conditions at the ELT's observation site and realistic detector statistics/readout, thereby producing data that faithfully mimics actual observations. This paper is primarily focused on utilizing HARMONI's LTAO IFS simulations to probe the nuclear stellar kinematics within the cores of nearby dwarf galaxies. The objective is to discern the telltale kinematic signatures associated with IMBHs and estimate their masses. These simulations also delineate the boundaries within which HARMONI can deliver feasible observables. Furthermore, they provide invaluable scientific insights, offering guidance for future research endeavours that will leverage actual data obtained with ELT/HARMONI.

¹² <https://harmoni-elt.physics.ox.ac.uk/>

Table 5. Mock HSIM IFS of NGC 300 and NGC 3115 dw01 (DIT = 15 min.)

Galaxy name	HSIM band	Exptime (minutes)	Sensitivity (minutes)
(1)	(2)	(3)	(4)
NGC 300	<i>J</i>	120 = DIT×8	60 = DIT×4
	<i>H, H-high</i>	150 = DIT×10	90 = DIT×6
	<i>K, K-short, K-long</i>	180 = DIT×12	120 = DIT×8
NGC3115 dw01	<i>J</i>	120 = DIT×8	60 = DIT×4
	<i>H, H-high</i>	150 = DIT×10	90 = DIT×6
	<i>K, K-short, K-long</i>	180 = DIT×12	120 = DIT×8

Notes: Column 1: the galaxy name. Column 2: HSIM band chosen to perform IFS simulation for observational mock datacubes and their kinematic measurements. Column 3: real exposure time we put in HSIM for our simulated kinematics maps presented in Figs 7 and 8, where the total integration time is determined as DIT×NDIT. Column 4: Sensitivity in terms of exposure time at which we test the lowest limit of S/N from the simulated IFS so that our pPXF still extract accurate kinematics (will be discussed later in Section 7.3). We should note that the estimated time show in Columns 3 and 4 are the science time on targets without accounting for the target acquisition, overhead, and AO setup time.

6.2 Simulations of the mock IFS datacubes

We used the dedicated HSIM pipeline to simulate the HARMONI observations with three medium (*J, H, K*: $\lambda/\Delta\lambda \approx 7, 100, \sigma_{\text{instr}} \approx 18 \text{ km s}^{-1}$) and three high (*H-high, K-short, K-long*: $\lambda/\Delta\lambda \approx 17, 400, \sigma_{\text{instr}} \approx 6 \text{ km s}^{-1}$) spectral resolution gratings to access the effect of kinematics errors and test the feasibility of different stellar features on M_{BH} determination.

Following N23 and Crespo Gómez et al. (2021), the spectrum in the *K*-band (comprising *K-short* and *K-long*) offers several molecular absorption lines, including commonly used CO absorption bandheads within the range of 2.29–2.47 μm (e.g. $^{12}\text{CO}(2-0)$ $\lambda 2.293 \mu\text{m}$ and $^{12}\text{CO}(3-1)$ $\lambda 2.312 \mu\text{m}$ bands), which are instrumental in measuring stellar kinematics. Additional atomic lines such as Na I $\lambda 2.207 \mu\text{m}$, Ca I $\lambda 2.263 \mu\text{m}$, and Mg I $\lambda 2.282 \mu\text{m}$ are also essential for this purpose. In the *H*-band (or *H-high*), a plethora of atomic absorption lines (e.g. Mg I $\lambda 1.487, 1.503, 1.575, 1.711 \mu\text{m}$, Fe I $\lambda 1.583 \mu\text{m}$, and Si I $\lambda 1.589 \mu\text{m}$) and strong CO absorption features (e.g. $^{12}\text{CO}(3-0)$ $\lambda 1.540 \mu\text{m}$, $^{12}\text{CO}(4-1)$ $\lambda 1.561 \mu\text{m}$, $^{12}\text{CO}(5-2)$ $\lambda 1.577 \mu\text{m}$, $^{12}\text{CO}(6-3)$ $\lambda 1.602 \mu\text{m}$, $^{12}\text{CO}(7-4)$ $\lambda 1.622 \mu\text{m}$, and $^{12}\text{CO}(8-5)$ $\lambda 1.641 \mu\text{m}$) are available. Additionally, promising atomic and molecule absorption lines in the *J*-band IFS have been identified for potential use in future works. These lines are primarily related to metallicity and include Fe I, Mg I, Si I, and Ti I (e.g. Ti I $\lambda 1.1896, 1.1953 \mu\text{m}$; Si I $\lambda 1.1988, 1.1995, 1.2035, 1.2107 \mu\text{m}$; Mg I $\lambda 1.1831, 1.2087 \mu\text{m}$; Fe I $\lambda 1.1597, 1.1611, 1.1641, 1.1693, 1.1783, 1.1801, 1.1887, 1.1976 \mu\text{m}$) (Rayner et al. 2009; Lyubenova et al. 2012). A subset of these potential atomic and molecular absorption lines is indicated on the six HSIM mock IFS spectra presented in Fig. A1 in the supplementary material. These lines were identified to guide the selection of the optimal wavelength range for extracting stellar kinematics, aiming to avoid contamination from sky emission (e.g. OH lines in *J* band), as discussed in Section 6.3. For a comprehensive list and illustrations of these stellar absorption tracers, readers can refer to Wallace & Hinkle (1996), Wallace & Hinkle (1997), Rayner et al. (2009), Evans et al. (2011), Lyubenova et al. (2012), and Crespo Gómez et al. (2021).

It is worth noting that the atomic absorption species and molecular absorption lines in the *J, H, H-high, K-short*, and the blue part of the *K*-band IFS exhibit relatively narrow profiles and low intensity, rendering them being saturated at very high velocity dispersion in massive galaxies (as in N23) but not for NSCs, which have much

lower σ_* . This limitation arises from the fact that SMBHs generate high-velocity dispersions ($\sigma_* \geq 75 \text{ km s}^{-1}$) in their vicinity, causing line broadening and blending with spectral noise. However, these lines may serve as effective indicators for measuring stellar kinematics around IMBHs with lower velocity dispersions. In this simulated work focusing on IMBHs, we will evaluate the feasibility of using these lines in the *J* band, *K-short*, and the blue part of the *K*-band IFS to measure stellar kinematics (Section 6.3).

All essential properties of NGC 300 and NGC 3115 dw01 needed for the modelings are presented in Section 3.4, while the chosen grating IFS and HSIM simulations are shown in Table 5. Regarding the AO performance during HSIM simulations, we applied the LTAO mode with an NGS of 17.5 mag in *H*-band within the radial distance of $30''$, the optical (500 nm) zenith seeing of FWHM = $0''.64$, and airmass of 1.3. These parameters are defaulted in HSIM to perform median observational conditions for the Armazones site.

We conducted IFS simulations within a central measured $0''.4 \times 0''.4$ with a pixel size of $10 \times 10 \text{ mas}^2$. This choice ensuring that the stellar kinematics, primarily influenced by the central black holes in our HARMONI IMBH sample, could be robustly detected. The exposure time for each simulation was carefully adjusted based on the gratings to ensure a S/N of at least 3 in each spaxel at the measured stellar features. Subsequently, pixel binning was employed to increase the S/N further. To replicate actual ELT observations, we incorporated multi-exposure frames and dithering by setting a Detector Integration Time (DIT) of 900 s (15 min.) for each exposure. The total exposure time was determined by the number of exposures (NDIT), which is an integer specified in the HSIM pipeline.

For this study, we adopted a Gaussian assumption for the line-of-sight velocity distribution (LOSVD). To do this, we first computed both the 2D intrinsic first (V) and second (V_{rms}) moment of stellar integrated velocity using the JAM_AXI_PROJ routine from the JAMPY package (see footnote 7; Cappellari 2008, 2020), then calculated the velocity dispersion $\sigma_*^2 = V_{\text{rms}}^2 - V^2$. Finally we assumed the LOSVD is a Gaussian with mean velocity dispersion equal to the JAM moments described in Section 4.1.

In the JAM_{cyl} modelings, we chose to simulate three sets of kinematics corresponding to three different black hole masses those are fractions of their NSC masses in both cases, such as 0%, 0.5%, 1% for both NGC 300 and NGC 3115 dw01. These adoptions are equivalent to $M_{\text{BH}} = (0, 5 \times 10^3, \text{ and } 10^4) M_{\odot}$ for NGC 300 and $M_{\text{BH}} = (0, 3.5 \times 10^4, \text{ and } 7 \times 10^4) M_{\odot}$ for NGC 3115 dw01. Here, we calculated the NSC mass for NGC 300 ($M_{\text{NSC}} = 1.05 \times 10^6 M_{\odot}$) and NGC 3115 dw01 ($M_{\text{NSC}} = 7.01 \times 10^6 M_{\odot}$) using their MGE models of Core-Sérsic profile listed in Table A2 (in the supplementary material) and their $M/L_{\text{I}} \approx 0.6 (M_{\odot}/L_{\odot})$ (for NGC 300; Neumayer & Walcher 2012) and $M/L_{\text{F814W}} \approx 1.4 (M_{\odot}/L_{\odot})$ (for NGC 3115 dw01; Pechetti et al. 2020), which are consistent with their JAM model masses within 3% uncertainty. The resulting kinematic maps were computed using JAM_{cyl} on a regular grid within the central regions of $0''.4 \times 0''.4$ and a pixel size of $5 \times 5 \text{ mas}^2$. These maps were subsequently convolved with the HARMONI PSF, rebinned, and interpolated to the specific pixel-sampling scale of $10 \times 10 \text{ mas}^2$ by the HSIM software. Additionally, for the sake of simplicity, we assumed isotropic JAM_{cyl} models ($\beta_z = 0$) and inclination angles $i = 42^\circ$ in our simulations (discussed in Section 3.4).

Because the HARMONI IMBH sample is restricted within $\lesssim 10$ Mpc, we ignored the spectrally stellar features' shifted towards the longer wavelength part due to redshift. Based on all these assumptions, we thus created an input noiseless-IFS cube for HSIM by employing the following steps:

- (i) Given the synthetic-stellar spectrum chosen for population

(SPS; Section 4.3), we logarithmically did rebin it to a scale at which the velocity scale is set as $v_{\text{scale}} = 0.5 \text{ km s}^{-1}$ to obtain a constant $\Delta \log \lambda$ intervals in the spectrum.

(ii) We constructed kinematics Gaussian kernel sampled with a step of $\Delta V = 0.5 \text{ km s}^{-1}$ for each spatial position in the IFS cube at which the mean velocity and velocity dispersion (V^2 and σ_*) is computed by the JAM_{cyl} model for that position.

(iii) We logarithmically convolved the rebinned spectrum created from step (i) with the Gaussian kernel generated from step (ii), which will be linearly interpolated to the constant wavelength step $\Delta \lambda \approx 0.01 \text{ \AA}$. This newly constant-wavelength step is small enough to conserve information during the interpolation.

(iv) We rebinned the spectrum by co-adding an integer number of adjacent spectral pixels to reach a step in wavelength at a minimum two times smaller than the smallest HARMONI instrumental resolution in terms of FWHM (e.g. the *J*, *H*, *K* gratings have $\Delta \lambda \approx 2 \text{ \AA}$ and the *H*-high, *K*-short, *K*-long have $\Delta \lambda \approx 0.5 \text{ \AA}$), making a rigorous integral over the pixels, and no information is lost.

(v) We stored the resulting linearly-sampled, LOSVD-convolved, and noiseless spectrum in a cube.

(vi) We estimated the surface brightness of NGC 300 and NGC 3115 dw01 (i.e. integrated intensities) using their models' best-fit parameters of a Core-Sérsic + a pure-Sérsic function inferred from Table 4, then assigned every spaxel's intensity to its corresponding linearly-sampled, LOSVD-convolved, and noiseless spectrum in the cube. Since these multi-Sérsic profiles only describe the galaxies' surface brightnesses along their major axes, these two galaxies are not all spherical. We thus computed the elliptical radius of every pixel using the relation: $r_{\text{ellipse}}^2 = x^2 + (y/q)^2$, to account for galaxy shapes, where x , y , and q are the positions of pixels (x , y) and the axis ratio from the stellar-light MGE model (Table A2 in the supplementary material), respectively, then assigned the flux by their corresponding multi-Sérsic profile $I(r_{\text{ellipse}})$ in equation (1).

(vii) We scaled the template spectrum in each $5 \times 5 \text{ mas}^2$ spaxels in the manner so that the surface brightness in a single pixel of the *HST*/F814W-band image (in mag arcsec^{-2} , pixel scale of $0''.045$) represented in the mean flux (in $\text{erg s}^{-1} \text{ cm}^{-2} \text{ \AA}^{-1} \text{ arcsec}^{-2}$) distributed into the total number of 80 ($5 \times 5 \text{ mas}^2$) spaxels area. The surface brightness is necessary for estimating the required sensitivity (and thus *S/N*) observed with HARMONI, which should be high enough for measuring the stellar (or ionized gas emission, if detected) kinematics precisely within a reasonable exposure time (N23).

6.3 HSIM mock datacubes and extracted kinematics

In accordance with N23, we have identified several prominent stellar absorption features associated with molecules and atomic species commonly observed in realistic IFS datacubes.

To begin, we have established the optimal spectral wavelength ranges for fitting stellar templates to measure stellar kinematics across the six grating bands. These ranges include $\lambda 2.28\text{--}2.40 \text{ \mu m}$ for both the *K*- and *K*-long bands, $\lambda 1.45\text{--}1.74 \text{ \mu m}$ for both the *H*- and *H*-high bands, and $\lambda 1.16\text{--}1.218 \text{ \mu m}$ for the *J*-band and $\lambda 2.05\text{--}2.20 \text{ \mu m}$ for the *K*-short band within the HSIM IFS mock datacubes. These wavelength ranges are depicted in Fig. A1 in the supplementary material, along with all the previously identified absorption features. Subsequently, to enhance the reliability of our stellar kinematic measurements and the applicability of the identified absorption features across the six HARMONI IFS gratings, we conducted experiments by fitting the entire spectral ranges of the gratings (excluding the *J*-band IFS due to contaminated by the OH lines from sky emission). We

then compared the results with those obtained by fitting the fixed best spectral wavelength ranges. The experiments demonstrated that the differences in kinematic measurements between these two fitting approaches are minimal, typically less than 5%. These findings validate the robustness and feasibility of employing the atomic and molecular absorption features in stellar spectra of the *J*, *H*, *H*-high, *K*-short, and the blue part of the *K*-band IFS, both from N23 and the present work, to measure stellar kinematics for IMBH mass estimation with minimal uncertainty. We will also discuss these statistical errors in Section 7.1; and see Figs 9, A4 and A5 (in the supplementary material) for NGC 300; also see Figs 10, A6 and A7 (in the supplementary material) for NGC 3115 dw01).

Prior to extracting stellar kinematic data from the simulated IFS data cubes in all six simulated HARMONI IFS bands, we employed a spatial binning technique to enhance the *S/N* to values exceeding 20 per bin over the listed above optimal spectral wavelength ranges specified for each grating band, as determined by adopting the adaptive Voronoi Binning method (vorbin¹³; Cappellari & Copin 2003). This technique involves grouping the signals of multiple spaxels within each bin while maintaining the noise at its median level, ultimately reducing the uncertainty in the kinematic measurements for that bin.

Subsequently, to derive the stellar kinematic measurements, we first carried out the binned spectra log-rebinning along the spectral dimension, then employed the Penalized PiXel-Fitting algorithm (pPXF¹⁴; Cappellari 2023) to fit the binned spectra of each bin to a stellar spectral template. During the pPXF fitting process, we utilized the MARCS (Gustafsson et al. 2008) version of the Maraston & Strömbäck (2011) SPS models. We corrected the template continuum shape using default Legendre polynomials (specifically, mdegree = 0 and degree = 4) and performed the fit for the kinematic parameters V (velocity) and σ_* (velocity dispersion) by specifying moments = 2. Additionally, we accounted for the instrumental broadening inherent to the HARMONI IFS by convolving the stellar templates with the constant instrumental dispersion adopted by HSIM.

To enhance the fidelity of our fitting procedure, we included 13 templates with ages ranging from 3 to 15 Gyr and Solar metallicities (z002). The best-fit SPS template is superimposed on sections of the simulated spectra from the central bin of all six gratings (*J*, *H*, *K*, *H*-high, *K*-short, and *K*-long), as illustrated in Fig. A1 in the supplementary material. For reference, the residuals (data-model) are also depicted as green dots in the same panel, providing a visual representation of the fit quality.

Figs 7 and A2 (in the supplementary material) present the kinematic maps of the NGC 300 nucleus, while Figs 8 and A3 (in the supplementary material) display those of the NGC 3115 dw01 nucleus. These maps have been extracted from the HSIM mock data cubes encompassing the *K*-long, *K*-short, *H*-high, *K*, *H*, and *J* bands and modeled using the JAM_{cyl} approach. Each figure comprises multiple red-bordered rectangular panels, with each panel containing kinematic measurements for three different black hole masses located at the centres of these NSCs as mentioned in Section 6.2. We have achieved a small root-mean-squared velocity scatter, typically with values of $\Delta V_{\text{rms}} \lesssim 1\%$. In each row-panel of the red-bordered rectangular plot, the kinematic maps are systematically displayed. These include maps showing the rotation (V) with the systemic velocity (V_{sys}) subtracted, velocity dispersion (σ_*), and root-mean-squared velocity (V_{rms}), which is defined as $V_{\text{rms}}^2 = V^2 + \sigma_*^2$.

The left panels of each red-bordered rectangular panel of these

¹³ v3.1.5 available from <https://pypi.org/project/vorbin/>

¹⁴ v8.2.1 available from <https://pypi.org/project/ppxf/>

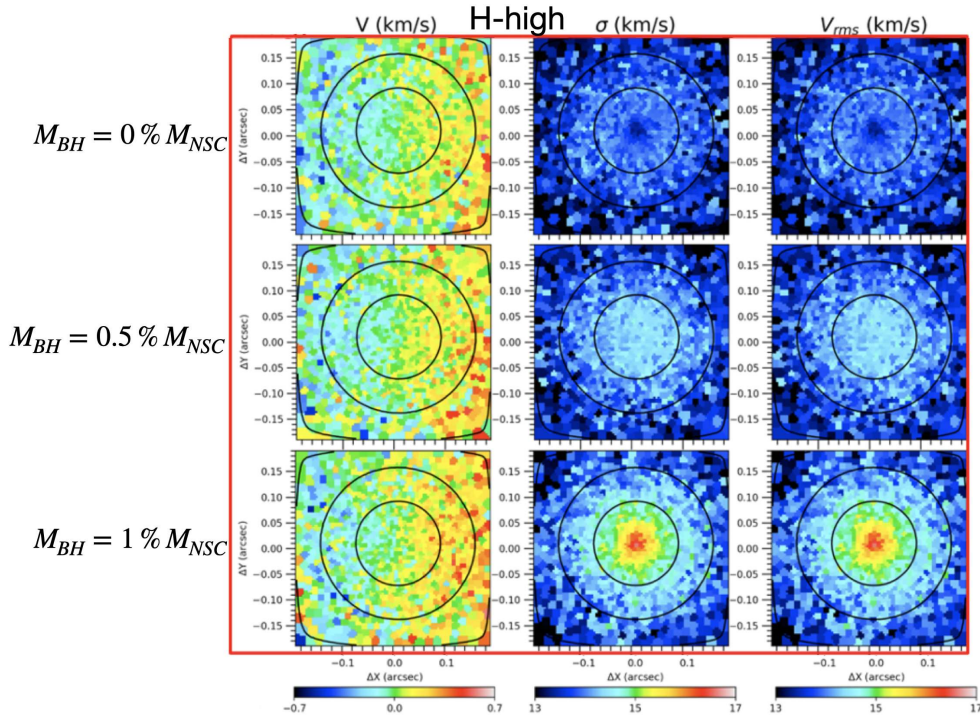


Figure 7. The stellar kinematic maps of NGC 300 extracted from the spectral part of $\lambda 1.15\text{--}1.22\ \mu\text{m}$ of the *H*-high HSIM IFS produced from JAM_{cyl} (Cappellari 2020) using pPXF (Cappellari 2023). These maps are presented with three different black hole masses: $M_{\text{BH}} = 0\ M_{\odot}$ (first-row plots), $M_{\text{BH}} = 5 \times 10^3\ M_{\odot}$ (second-row plots), and $M_{\text{BH}} = 10^4\ M_{\odot}$ (third-row plots). These IMBH masses are just a fraction of the NGC 300’s NSC mass, including 0%, 0.5%, and 1%, respectively (as indicated the left legends). On each row, these kinematic maps of each Voronoi bin are listed from left to right with (1) relative velocity (V) subtracted for the systemic velocity (V_{sys}) of the whole galaxy due to the Universe expansion, (2) velocity dispersion (σ_{\star}), (3) root-mean-squared velocity (V_{rms}); the black contours in all maps indicate the isophotes from the collapsed HSIM IFS cubes spaced by $1\ \text{mag arcsec}^{-2}$. The color bars at the bottom of the Fig are fixed at the same scale for all three black hole masses to illustrate the kinematic effects of the central black holes and also indicate the robustness of our proposed kinematic measurements at the centers of these dwarf galaxies hosting bright NSCs as the kinematic signatures for IMBHs.

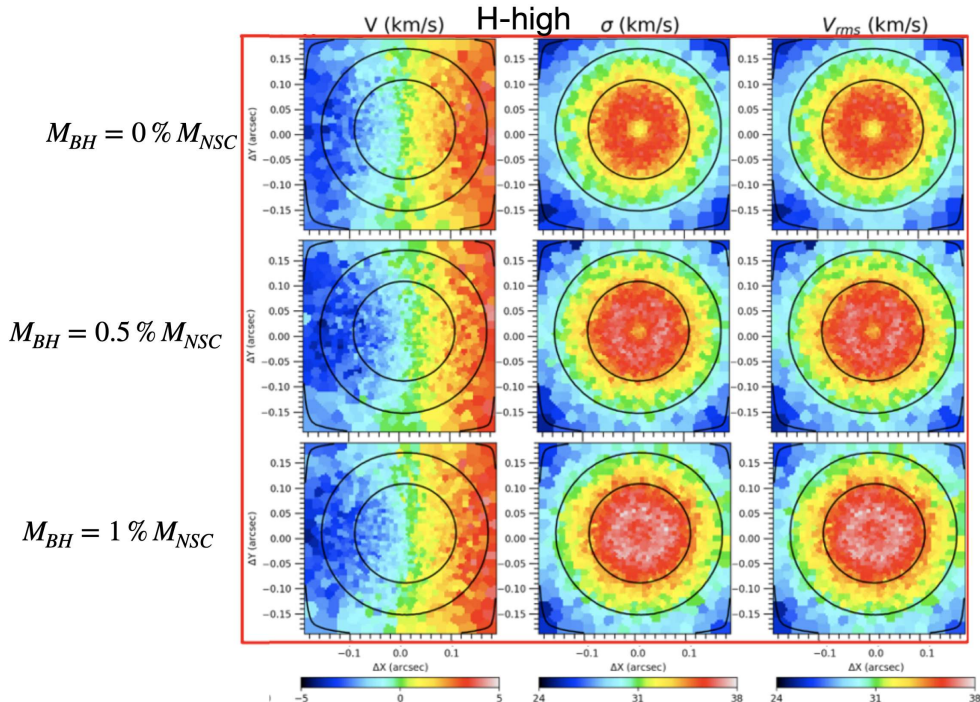


Figure 8. Same as Fig. 7 but for NGC 3115 dw01. These maps are presented with three different black hole masses: $M_{\text{BH}} = 0\ M_{\odot}$ (first-row plots), $M_{\text{BH}} = 3.5 \times 10^4\ M_{\odot}$ (second-row plots), and $M_{\text{BH}} = 7 \times 10^4\ M_{\odot}$ (third-row plots). These IMBH masses are just a fraction of the NGC 3115 dw01’s NSC mass, including 0%, 0.5%, and 1%, respectively (as indicated the left legends).

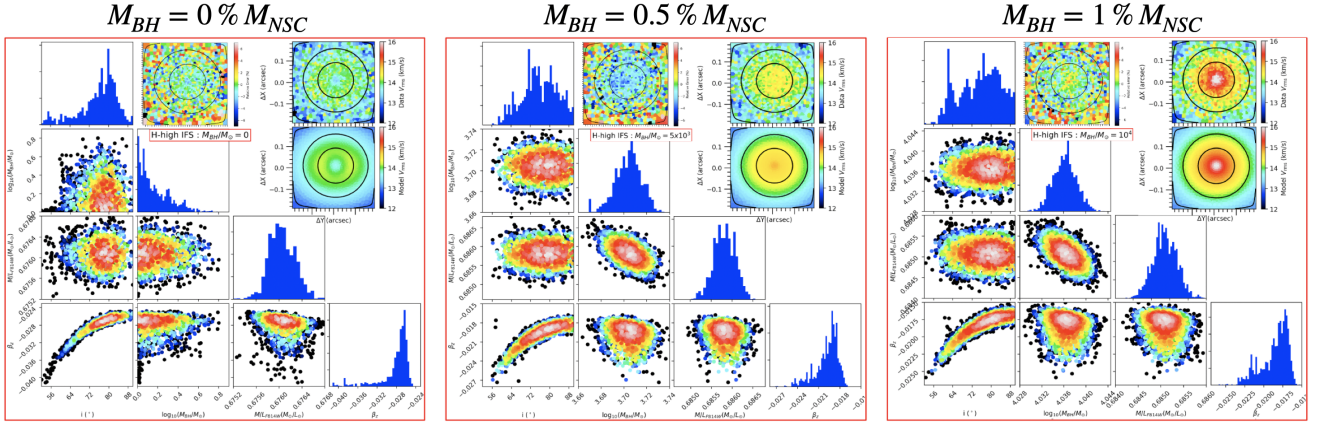


Figure 9. The figures display the posterior distributions obtained during the post-burn-in phase of the adamet MCMC optimization process for the JAM_{cy1} models applied to the HSIM simulated kinematics of NGC 300. These simulations were generated using the JAM_{cy1} models and feature three different black hole masses: $M_{\text{BH}} = 0 M_{\odot} = 0\% M_{\text{NSC}}$ (left panel), $M_{\text{BH}} = 5 \times 10^3 M_{\odot} = 0.5\% M_{\text{NSC}}$ (middle panel), and $M_{\text{BH}} = 10^4 M_{\odot} = 1\% M_{\text{NSC}}$ (right panel). Each red-square panel presents a set of four parameters, depicted as scatter plots illustrating their projected 2D distributions and histograms displaying their projected 1D distributions. These parameters include the inclination i , M_{BH} , M/L_{F814W} (mass-to-light ratio in the F814W band), and β_z . In the top right corner of each red-square panel, readers will find inset maps that depict the V_{rms} values. The top maps represent the simulated kinematic maps extracted from the simulated datacubes, while the bottom maps represent the kinematic maps recovered from the best-fit JAM_{cy1} model. These maps visually illustrate the level of agreement or disagreement at each spaxel (spatial pixel) between the simulated data and our chosen best-fit model. The determination of the best-fit JAM_{cy1} model is based on the probability distribution function (PDF) with the highest likelihood. These posterior distributions and associated maps are generated for HSIM simulated kinematics in the H -high wavelength band as an illustrated example.

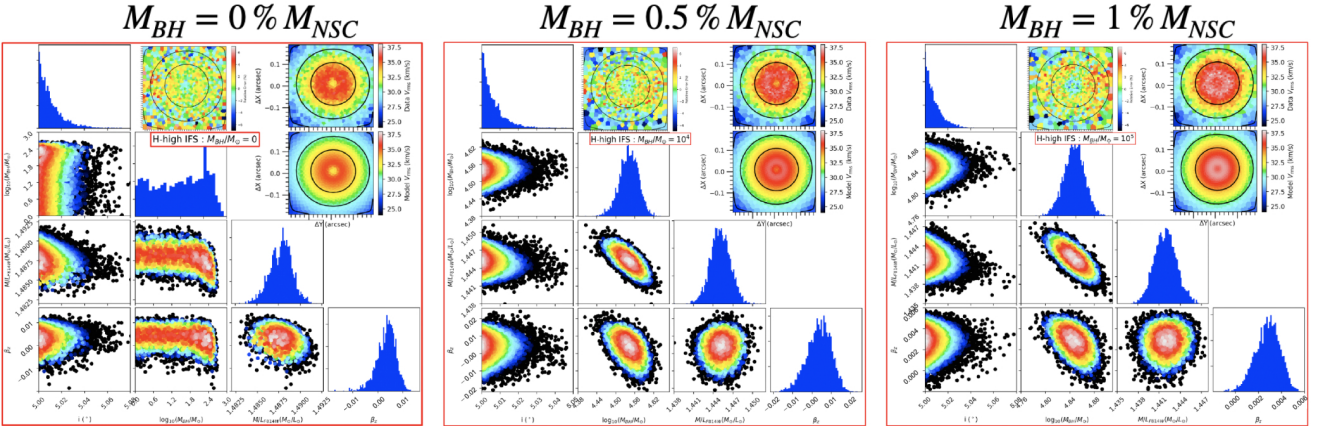


Figure 10. Same as Fig. 9 but for the HSIM simulated kinematics of NGC 3115 dw01 with three different black hole masses of $M_{\text{BH}} = 0 M_{\odot} = 0\% M_{\text{NSC}}$ (left panel), $M_{\text{BH}} = 3.5 \times 10^4 M_{\odot} = 0.5\% M_{\text{NSC}}$ (middle panel), $M_{\text{BH}} = 7 \times 10^4 M_{\odot} = 1\% M_{\text{NSC}}$ (right panel). These posteriors are produced for HSIM simulated kinematics in the H -high wavelength band as an illustrated example.

stellar kinematic maps of both NGC 300 and NGC 3115 dw01 displayed crucial signatures of the presence or absence of an IMBH, exhibiting a distinctive central drops in the velocity dispersion (σ_{\star}) and root-mean-squared velocity (V_{rms}) maps when either no black hole ($M_{\text{BH}} = 0 M_{\odot}$) is present or when the black hole masses are insufficient (e.g. $M_{\text{BH}} = 5 \times 10^3 M_{\odot}$ for NGC 300 and $M_{\text{BH}} = 3.5 \times 10^4 M_{\odot}$ for NGC 3115 dw01). This central drop in velocity dispersion is a common feature in the predicted stellar kinematics of galaxies when no or very small IMBHs are assumed, and it holds true for a range of assumed density and anisotropy profiles (e.g. see Section 4.2 and Tremaine et al. 1994). Conversely, models featuring relatively large IMBHs generate centrally rising peaks in both the velocity dispersion and root-mean-squared velocity maps at several central spaxels, which correspond to the black hole’s SOI, showing a clearly upturned trending as the IMBH mass increases. This observation aligns with the general expectation that central velocity dispersion

should increase in a Keplerian manner within a tiny region near the central IMBH, where its gravitational potential dominates over all others.

The disparity between these kinematic maps at the galaxy centers is notably clear for both NGC 300 and NGC 3115 dw01, which represent the closest and farthest targets in our HARMONI IMBH sample, respectively. This emphasizes the exceptional spectral and spatial resolving powers of ELT/HARMONI in detecting the stellar-kinematic signatures of central IMBHs in the local Universe and accurately measuring their masses through dynamic means.

Crucially, it is evident that HARMONI has the capability to distinguish between the kinematic effects of a scenario with no IMBH and one with a $3.5 \times 10^4 M_{\odot}$ IMBH ($V_{\text{rms}, M_{\text{BH}}=3.5 \times 10^4 M_{\odot}} - V_{\text{rms}, M_{\text{BH}}=0 M_{\odot}} \approx 1.0 \text{ km s}^{-1}$). This distinction remains discernible even at the distance of NGC 3115 dw01, which is $\approx 10 \text{ Mpc}$ away.

Nonetheless, both the NSCs of NGC 300 and NGC 3115 dw01

exhibit minimal rotation at their centers, with velocities of $V = 0.7$ km s⁻¹ for NGC 300 and $V = 5.0$ km s⁻¹ for NGC 3115 dw01. In both cases, the dominant factor is velocity dispersion.

The kinematic maps also reveal the presence of edge effects, particularly evident in the higher velocity dispersions (and consequently higher root-mean-squared velocities) observed in the top and bottom bins. This effect causes these bins to exhibit higher values compared to the predictions from the purely JAM_{cyl} model, primarily because these spaxel bins are located farther from the center. The consequence of this effect is the squared shape of the outermost surface brightness contour observed in all maps. To ensure the accuracy of our dynamical models and avoid uncertainties stemming from this instrumental issue, we have excluded all high V_{rms} bins from our model for M_{BH} (as described in Section 7.1).

7 DISCUSSION

7.1 Black hole mass recovering

Given the simulated IFS datacubes from six HSI gratings and the resulting kinematic maps (as detailed in Section 6.3), we performed fitting of these kinematic maps (specifically V_{rms}) to the JAM_{cyl} models, aimed at determining the black hole mass and constraining the model’s dynamical parameters. This involved making certain assumptions about a central compact dark mass object (referred to as IMBH), including its mass (M_{BH}), as well as considering dynamical parameters such as stellar orbitals (represented by the global anisotropy parameter β_z , equivalent to γ), stellar mass (parameterized by M/L relative to the best-fit stellar population estimate from the *HST*/F814W broad-band image, M/L_{F814W} , and the inclination angle (i).

In this process, we adopted a logarithmic scale for the black hole mass to ensure a more Gaussian sampling across multiple orders of magnitude, while the other three parameters were sampled in linear scales. During the fitting process, JAM_{cyl} generated kinematic models that could be compared to their corresponding simulated values (V_{rms}) while accounting for the HARMONI LTAO PSF, characterized by $\sigma_{\text{PSF}} \approx 5$ mas (or $\text{FWHM}_{\text{PSF}} \approx 12$ mas; N23).

To obtain the best-fit JAM_{cyl} model, we utilized a Markov Chain Monte Carlo (MCMC) simulation to comprehensively explore the parameter space encompassing i , M/L_{F814W} , M_{BH} , and β_z . The model was employed to fit the simulated kinematic data and determine the best-fit values, along with statistical uncertainties, using the adaptive Metropolis algorithm (Haario et al. 2001) within the Bayesian framework (adamet¹⁵ package Cappellari et al. 2013a). Our MCMC chains comprised a total of 3×10^4 iterations, with the initial 20% of iterations excluded as a burn-in phase. The full probability distribution function (PDF) was constructed from the remaining 80% of calculations after the burn-in phase. The best-fit parameters corresponded to the highest likelihood within the PDF, while the statistical uncertainties for all four parameters were determined at 1σ and 3σ confidence levels, representing the ranges (16–84)% and (0.14–99.86)% of the 80% remaining calculations after the burn-in phase, respectively.

During the fitting process, fixed search ranges were defined for all four model parameters (M_{BH} , M/L_{F814W} , β_z , i) as follows:

- M_{BH} : from 0 to $10^6 M_{\odot}$ (or $\log_{10}(M_{\text{BH}}/M_{\odot})$: from 0 to 6)
- M/L_{F814W} : from 0.1 to 3 (M_{\odot}/L_{\odot})
- β_z : from -1.0 to 0.99

- i : from 5° to 90°

Additionally, initial guesses for the JAM_{cyl} model parameters were fixed for M/L_{F814W} , β_z , and i . For example, for NGC 300, the initial guesses were set to $(M/L_{\text{F814W}}, \beta_z, i) = (0.6, 0, 42)$, while for NGC 3115 dw01, they were set to $(M/L_{\text{F814W}}, \beta_z, i) = (1.4, 0, 42)$. We also initially assumed the same values for the black hole masses as those used in the simulated IFS data, as described in Section 6.2. Specifically, we considered $M_{\text{BH}} = 0, 5 \times 10^3, 10^4 M_{\odot}$ for NGC 300 and $M_{\text{BH}} = 0, 3.5 \times 10^4, 7 \times 10^4 M_{\odot}$ for NGC 3115 dw01, irrespective of the specific IFS gratings used in the simulations. All of these initial guesses remained the same across all simulated IFS gratings.

In Figs 9, A4, A5 (in the supplementary material) for NGC 300, and Figs 10, A6, A7 (in the supplementary material) for NGC 3115 dw01, the best-fit JAM_{cyl} parameters and their associated statistical uncertainties are presented. These parameters describe the derived stellar kinematics for three different M_{BH} values and across six simulated HSI IFS gratings.

The figures depict 2D scatter plots for each parameter, with colored points representing their likelihood. White corresponds to the maximum likelihood, while black indicates a confidence level smaller than 3σ . Histograms are also included, showing the 1D distributions for each parameter. The 1D distributions were used to calculate the best-fit values and their corresponding uncertainties, which are listed in Table A3 for NGC 300 and Table A4 for NGC 3115 dw01 in the supplementary material.

The insert plots at the top-right corner of each red-squared panel in the figures highlight the best-fit models for each mock IFS by directly comparing the simulated V_{rms} to the corresponding JAM_{cyl} model, all on the same velocity scale. To provide a clearer view of the differences between the model and the data, the figures also include V_{rms} residual maps ($(\text{data} - \text{model})/\text{data}$) at the middle top of each red-squared panel. These residual maps show the relative agreements or disagreements between the data and the model on a bin-by-bin basis in the V_{rms} maps. In general, our constrained models exhibit excellent agreement with the mock kinematics across the $0''.4 \times 0''.4$ central regions of HARMONI’s FOV, irrespective of the specific gratings used.

The recovered values for M_{BH} and M/L_{F814W} closely match the input values used during the creation of the noiseless input cubes for the HSI simulations. The differences are typically less than 5% for both M_{BH} and M/L_{F814W} . However, it’s essential to note that these uncertainties, obtained from the MCMC routines, are formal and relatively small (e.g. the 3σ uncertainty is $\approx 5\%$). This is due to the high quality of the simulated kinematics and our choice of the lowest limits for the simulated black hole’s SOI used (i.e. $M_{\text{BH}} = 5 \times 10^3 M_{\odot}$ for NGC 300 and $M_{\text{BH}} = 3.5 \times 10^4 M_{\odot}$ for NGC 3115 dw01; as discussed in Section 6.2). These choices ensure that the SOIs are well-resolved with the 10×10 mas² angular scale of the HARMONI simulations (mentioned in Section 2 and for instance, these black holes have $R_{\text{SOI}} = 13$ mas at $D = 2.2$ Mpc of NGC 300 and $R_{\text{SOI}} = 35$ mas at $D = 9.7$ Mpc of NGC 3115 dw01). We expect that these errors produced from the realistic HARMONI observations will be larger, at least a factor of 2 or 3.

Remarkably, our analysis reveals consistent 2D parameter distributions across different black hole masses and mock IFS gratings, as evident in Figs 9, 10, and A4, A5, A6, A7 (in the supplementary material). Specifically, when black hole masses exceed zero, we observe an expected negative covariance between M_{BH} and M/L_{F814W} , resulting in a characteristic “banana shape” in the 3σ confidence level regions within the 2D PDF. This covariance arises due to the interplay between the potentials of central black holes and the host

¹⁵ v2.0.9 available from <https://pypi.org/project/adamet/>

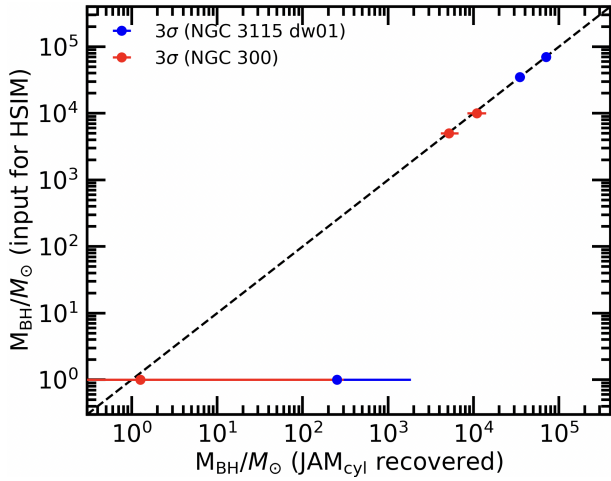


Figure 11. A summarized comparison of input IMBHs for HSIM and our recoveries, including statistical error bars at the 3σ confidence levels. The 3σ errors range from the 0.14th to the 99.86th percentiles determined from the MCMC fits of the JAM_{cyl} modelings to all six grating IFS mock data cubes for NGC 300 (see Table A3 in the supplementary material) and NGC 3115 dw01 (see Table A4 in the supplementary material). The black dashed line represents the equal-mass line between the input IMBH masses for HSIM and our recovered masses.

galaxies, where larger black holes correspond to smaller M/L_{F814W} values and vice versa.

This behaviour is attributed to the high spatial resolution of our simulations, enabled by the $10 \times 10 \text{ mas}^2$ observational scale, which allows us to resolve the SOI of even the smallest black holes in NGC 300 and NGC 3115 dw01 at their respective distances. In scenarios without black holes, the 2D PDF yields upper limits on the constrained black hole masses. Notably, these upper limits are consistently roughly $10^2 M_{\odot}$ for NGC 300 and $10^3 M_{\odot}$ for NGC 3115 dw01. This implies that HARMONI can effectively differentiate between black holes with masses above $10^2 M_{\odot}$ and $10^3 M_{\odot}$ for NGC 300 at the distance of 2.2 Mpc and NGC 3115 dw01 at the distance of 9.7 Mpc away from us, respectively; but see a discussion of dynamical mass segregation in Section 7.2.

The recoveries of β_z are also notably well-constrained by the models, yielding tiny uncertainties with preferred values of $\beta_z \approx 0$ for both NGC 300 (slight dominance with tangential stellar orbits, $\beta_z \lesssim 0$) and NGC 3115 dw01 (slight dominance with radial stellar orbits, $\beta_z \gtrsim 0$), which are totally consistent to the input $\beta_z = 0$ (isotropic; see Section 6.2). In addition, it is worth noting that the inclination angle (i) is not as tightly constrained by the simulated data, spanning a wide range from 40° to 90° for NGC 300 but strictly remains at $\gtrsim 5^\circ$ for NGC 3115 dw01 (except for the constrained model with the J band's kinematics, which behaves in a similar manner of the constrained models of NGC 300). This can be attributed to the nature of the kinematics observed in NGC 300 and NGC 3115 dw01, where velocity dispersion dominates, and there is little ($V \approx 5 \text{ km s}^{-1}$ for NGC 3115 dw01) to almost no rotation ($V \approx 0.7 \text{ km s}^{-1}$ for NGC 300). In cases where the NSCs exhibit minimal rotation, their kinematics behave almost like spherically axisymmetric systems, and in the limit of sphericity, galaxies appear similar over a wide range of inclinations. This characteristic results in less constrained inclination angles in our models.

Graphically, a concise summary of the comparisons between the input black hole masses for HSIM and their corresponding recovered values using the adamet MCMC algorithm and JAM_{cyl} modelings

is presented in Fig. 11. Additionally, the recovered black hole masses for both galaxies listed in Tables A3 and A4 of the supplementary material are included in this figure. In this figure, we utilize the median black hole masses recovered from all six gratings (e.g. H -high, K -short, K -long, J , H , K) IFS mock kinematics as the representative values for our simulations. The error bars, adopted within 5% (3σ) of the statistic uncertainties, are also displayed accordingly.

7.2 Caveat of dynamical mass-segregation processes

According to a review by Greene et al. (2020, section 3.2), stringent dynamical constraints on a black hole of $M_{\text{BH}} \approx 3 \times 10^3 M_{\odot}$ in Galactic GCs could be measurable with ELT. Because of mass segregation, only the most massive stars (i.e. $M_{\text{star}} \approx 20 M_{\odot}$ remain near the black hole. For such a black hole, their SOI contains (by definition, see footnote 1) ≈ 150 such massive stars, enough for dynamical and statistical measurements from integrated light. In this work, we adopt the lower limits for unambiguously detecting and measuring black holes in these two galaxies (i.e. also representing for our HARMONI IMBH sample entirely) equal to 0.5% of their NSCs' masses. These numbers are all above the limit of $M_{\text{BH}} \approx 3 \times 10^3 M_{\odot}$.

Nevertheless, Bianchini et al. (2017) proposed that stellar-mass black holes may undergo mass segregation on timescales considerably shorter than the relaxation time (t_{relax}) of GCs, causing them to migrate toward the center. This migration enhances the central mass-to-light ratio (M/L) of GCs. Consequently, there is a potential for a notable accumulation of stellar-mass black holes at the centers of bound stellar systems, including GCs and NSCs. This concentration of mass can lead to an increase in M/L , creating a mimicry of the stellar kinematics in the central regions of these systems and potentially resulting in a false detection of an IMBH. Observations of the GC M15 indeed show an enhancement in M/L (den Brok et al. 2014). It is important to highlight that the current simulations primarily focus on low-mass systems, which constitute a significant portion of our HARMONI IMBH sample. However, uncertainties persist regarding the extent to which stellar-mass black holes segregate and are retained during this process.

To avoid the false detections of IMBHs due to mass segregation, it is necessary to have accurate estimates of the stellar system's relaxation timescale as a function of radius using the following equation (Bahcall & Wolf 1977; Valluri et al. 2005):

$$t_{\text{relax}}(r) \approx (1.4 \times 10^8 \text{ yr}) \sigma_{20}^3(r) \rho_5^{-1}(r) (\ln \Lambda_{10})^{-1}. \quad (3)$$

where $\sigma_{20} = \sigma_{\star}/20 \text{ km s}^{-1}$, $\rho_5 = \rho/10^5 M_{\odot} \text{ pc}^{-3}$, $\ln \Lambda_{10} = \ln(\Lambda)/10$ (i.e. Λ is denoted as the "Coulomb logarithm" and we assumed it is $\ln \Lambda = 10$). Here, σ_{\star} denotes the stellar velocity dispersion, which is assumed as a constant within the central measuring $0''.4 \times 0''.4$ in our simulations. $\rho_{\text{dyn}}(r)$ is the intrinsic mass densities of the stellar systems. If the estimated relaxation time is approximately equal to or longer than the age of the Universe, it guarantees that there is no accumulation of stellar-mass black holes at the nuclei's centers. Therefore, the observed enhancement in velocity dispersion in the central region is a genuine signature of IMBHs.

In order to compute t_{relax} for the NSCs of NGC 300 and NGC 3115 dw01 as examples, we used $\sigma_{\star} = 13.3 \text{ km s}^{-1}$ for NGC 300 (Kacharov et al. 2018) and $\sigma_{\star} = 32 \text{ km s}^{-1}$ for NGC 3115 dw01 (Peterson & Caldwell 1993) (Section 3.4). We also used the MGE models listed in Table A2 (in the supplementary material) to estimate $\rho_{\text{dyn}}(R_e)$ for NGC 300 (13 first Gaussians) and NGC 3115 dw01 (3 first Gaussians), after an analytic deprojection of the MGEs,

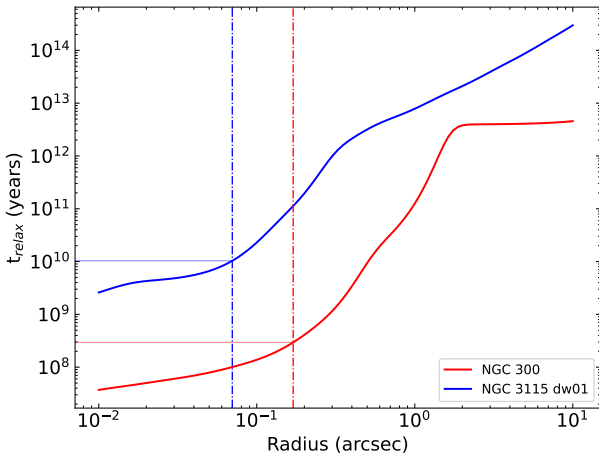


Figure 12. Relaxation time $t_{\text{relax}}(R)$ as functions of radius (in pc) in NGC 300 (red solid line) and NGC 3115 dw01 (blue solid line) in the model solutions without black holes. The same colour but vertically dash-dotted lines indicate the effective radii (R_e) of their NSCs. See text for details.

using their corresponding photometric $M/L_1 \approx 0.6 (M_\odot/L_\odot)$ (Neumayer & Walcher 2012) and $M/L_{F814W} \approx 1.4 (M_\odot/L_\odot)$ (Pechetti et al. 2020) and assuming the spherical mass distribution for both NSCs. These NSCs’ R_e are listed in Table 4. Our calculations, as shown in Fig. 12, yield $t_{\text{relax}}(R_e \approx 1.9\text{pc}) \approx 3 \text{ Myr}$ for NGC 300 and $t_{\text{relax}}(R_e \approx 3.2\text{pc}) \approx 10 \text{ Gyr}$ for NGC 3115 dw01, suggesting mass segregation cannot be exclusively excluded from our consideration for central IMBH detections via stellar kinematics in NSCs, especially for the case of NGC 300. Nevertheless, more realistic simulations are necessary to assess whether substantial fractions of the NSC black holes can indeed undergo mass segregation and remain retained within the clusters (Nguyen et al. 2018).

In the case of NGC 300, which is particularly prone to mass segregation, the situation is compounded by the fact that its NSC has a size with $R_e \approx 0''.17$, just slightly smaller than our HARMONI’s central measuring region with a radius of $0''.2$. The exceptionally well-resolved kinematics and close proximity of NGC 300 exacerbate the challenges involved in accurately measuring the mass of its IMBH. This is primarily because any variation or enhancement in M/L due to mass segregation can reproduce the kinematics exclusively attributed to the black hole. While the simulated work of mass segregation and its effect on M/L variation lies beyond the scope of this paper, we intend to present this analysis in a subsequent article.

If t_{relax} is relatively short, some stellar-mass black holes may migrate toward the center, potentially complicating the detection of IMBHs (e.g. Nguyen et al. 2018). Recent studies have proposed that these migrating stellar-mass black holes could be identified through gravitational microlensing events, observed over extended periods in time-domain observations (e.g. Bennett et al. 2002). This is particularly relevant because massive star clusters are considered primary candidates for hosting binary black hole mergers detected through gravitational waves (e.g. Wang et al. 2022). The theoretical expectation is that such massive clusters can retain a large population of stellar-mass black holes, which subsequently migrate to the cluster’s center, providing a steady source of binary systems (e.g. Banerjee et al. 2010). Nevertheless, the complexity of gravitational microlensing caused by stellar-mass objects fall well below the resolvable power of ELT for extragalactic stellar systems. This topic is beyond the scope of discussion in this paper.

For typical GCs, there is limited observational (e.g. van der Marel

& Anderson 2010) and theoretical (e.g. Zocchi et al. 2017, 2019; Baumgardt et al. 2019) supports for the idea that IMBH formation is favored in these environments. In contrast, many NSCs exhibit high velocity dispersions and a range of relaxation times (typically half-mass relaxation times are many gigayears), making them plausible sites for the formation of IMBHs (see a review by Neumayer et al. 2020, section 10.1).

7.3 Sensitivity limits

We have also examined the ultra-sensitivity in terms of exposure time for the instruments, conducting similar simulations for both galaxies, NGC 300 and NGC 3115 dw01. In these simulations, we progressively reduced the exposure times, consequently lowering S/N, until the simulated HARMONI IFS cubes still yielded marginally meaningful kinematic maps after spaxel binning via Vorbin, targeting a specific bin-S/N of ≈ 20 . The resulting required exposure times for each galaxy are detailed in Column 4 of Table 5. It is important to note that the galaxy’s surface brightness was derived from *HST* images (for NGC 300 we added the large-scale MPG/ESO observations for its extended disk) and extrapolated to the 4 mas regime using an analytical function discussed in Section 5. Additionally, we considered the flux spread across the grating’s wavelengths, as explained in Section 6.2. These required exposure times are relatively short, less than three hours, making them well-suited for ELT observations.

However, it is essential to exercise caution as our sensitivity estimates in terms of exposure time offer approximate values for the HARMONI IMBH survey. The actual sensitivity measurements may be somewhat lower, necessitating longer exposure times. This is due to the potential impact of higher spatial-resolution imaging (e.g. $\lesssim 0''.05$ from *HST*/WFPC2 and *JWST*/NIRCam or a few mas from ELT/MICADO), which could resolve out some of the flux. Therefore, we are demonstrating the feasibility of our proposed science with ELT/HARMONI while acknowledging that real sensitivity measurements may require adjustments.

8 CONCLUSIONS

Guided by our mission to conclusively establish the presence of IMBHs within the Local Universe (up to a distance of $\approx 10 \text{ Mpc}$), bridging the current gap between well-understood stellar-mass black holes and SMBHs, we have utilised the potentially unparalleled capabilities of ELT and its cutting-edge instrument, HARMONI, thanks to its remarkable advancements in spatial and spectral resolution, coupled with its unprecedented sensitivity across the optical and near-infrared spectrum. Our objective is to understand the stellar dynamics of the nuclei of nearby dwarf galaxies. Through this process, we aim to uncover integrated kinematic signatures that may signify the existence of IMBHs nestled at the cores of these galaxies. Subsequently, we endeavor to precisely determine the masses of these IMBHs via rigorous dynamical modelling.

In the near future, when the ELT becomes operational, it promises to offer a comprehensive insight into the realm of black hole physics. This endeavor will also shed light on the underlying physical processes that govern the origin and co-evolution of central black holes and their host galaxies. This profound exploration will span the entire spectrum of black hole masses and galaxy masses and sizes, encompassing IMBHs (Nguyen et al. 2018) in dwarf galaxies to the colossal SMBHs residing in the most massive galactic systems (N23).

Drawing upon the extensive body of literature encompassing both photometric and spectroscopic surveys, as well as insightful case

studies, we embarked on a quest to assemble a cohort of nearby nucleated dwarf galaxies. Our selection criteria, designed to ensure observability with ELT, were stringent: galaxies falling within the range of $-20.3 < M_K < -13.3$ mag, situated in regions with $|\delta + 24^\circ| < 45^\circ$ and $|b| \leq 8^\circ$. This meticulous pursuit yielded a treasure trove of 45 nucleated dwarf galaxies, characterized by a stellar mass spanning $2 \times 10^6 < M_\star < 5 \times 10^{10} M_\odot$. Remarkably, this selection comprises a diverse array of galaxy types, with ellipticals constituting 13%, lenticulars representing 16%, spirals accounting for 60%, and irregulars taking 11%. These galaxies play host to luminous NSCs, with masses and effective radii falling within the ranges of $10^5 < M_{\text{NSC}} < 6 \times 10^7 M_\odot$ and $3 < R_e < 27$ pc, respectively. Crucially, they exhibit low central velocity dispersion, $\sigma_{\star,c} < 75 \text{ km s}^{-1}$, a vital criterion ensuring the potential presence of IMBHs.

Subsequently, our sample selected strategy resulted in what we refer to as the ‘‘HARMONI IMBH sample.’’ By extending our attention to the galaxies with lowest stellar masses, we have pushed the limit goes below the conventional stellar and gas dynamics of current SMBH mass measurements. Additionally, the HARMONI IMBH sample is ideal to address the existing bias toward dwarf early-type galaxies, as demonstrated by previous research (Nguyen et al. 2018). It includes a wide range of galaxy types and spectrum of extragalactic environments, ranging from isolated galaxies to those dwelling within satellite galaxy fields.

Our planning IFS and imaging observations of the HARMONI IMBH sample will serve as Rosetta Stone for testing diverse black hole seeding formation scenarios, dating back to high-redshift epochs (approximately $z \sim 30 - 12$). Furthermore, these observations will be instrumental in refining models that operate at the lower end of the black hole mass function. This refinement holds significant importance, particularly in predicting the detection rate of gravitational waves with the Laser Interferometer Space Antenna (LISA). Additionally, it will afford deeper insights into the intrinsic behavior of black hole–galaxy scaling relations, particularly within the lower-mass regime (see Nguyen et al. 2019, for a compelling example).

Our analysis of the kinematic maps extracted from the previously mentioned absorption features yielded consistent results within the margins of systemic errors. Specifically, the medium spectral resolution (J, H, K) exhibited systemic errors of $\Delta V_{\text{rms,sys}} \lesssim 0.3 \text{ km s}^{-1}$, while the high spectral resolution (H -high, K -short, K -long) demonstrated even smaller systemic errors of $\Delta V_{\text{rms,sys}} \lesssim 0.1 \text{ km s}^{-1}$.

Our comprehensive testing revealed that the medium spectral gratings (J, H, K) provided kinematic measurements consistent with those obtained from the high spectral resolution gratings (H -high, K -short, K -long) for a stellar system down to a factor of 2 with respect to their instrument errors (σ_{instr}). In terms of instrument errors, the medium spectral gratings (J, H, K) exhibited an instrument error of $\sigma_{\text{instr}} \approx 18 \text{ km s}^{-1}$, while the high spectral resolution (H -high, K -short, K -long) displayed a lower instrument error of $\sigma_{\text{instr}} \approx 6 \text{ km s}^{-1}$. This implies that, despite NGC 300’s velocity dispersion of $\sigma_\star \approx 13 \text{ km s}^{-1}$, the medium spectral gratings still delivered reliable measurements in agreement with those derived from the high spectral resolution gratings. Consequently, we can establish a velocity dispersion threshold for accurately obtaining stellar kinematics using the spectral gratings: the medium spectral gratings (J, H, K) remain effective in nuclei with $\sigma_\star \approx 10 \text{ km s}^{-1}$, while the high spectral resolution gratings (H -high, K -short, K -long) can be employed down to a limit of $\sigma_\star \approx 3 \text{ km s}^{-1}$.

Subsequently, we harnessed these simulated kinematics to estimate the masses of IMBHs. This was achieved by combining the kinematic data with the interpolated stellar-mass model derived from the *HST* image (and combined with the extended MPG/ESO 2.2-m *R* band

image for NGC 300) and employing JAM_{cyl} modeling techniques. Our findings indicated that the retrieved M_{BH} and M/L_{F814W} values from the simulated data were in complete agreement with our input values, demonstrating an impressive level of consistency with uncertainties of less than 5%.

Our simulations served as a powerful demonstration of HARMONI’s capabilities, highlighting its potential as a unique facility for accurately measuring IMBH masses and delving into the black hole mass–galaxy scaling relations, particularly within the lowest-mass regimes for both host galaxies and black holes.

Our proposed survey, featuring angular resolutions of $R_{\text{SOI}} = 10 \times 10 \text{ mas}^2$ and simulated pixel scales of $10 \times 10 \text{ mas}^2$, proved to be highly effective in resolving the stellar kinematics within the central black hole’s SOI. This was achieved down the IMBHs with masses that are as small as 0.5% of their NSCs mass (i. e. $5 \times 10^3 M_\odot$ for NGC 300 at a distance of 2.2 Mpc and $3.5 \times 10^4 M_\odot$ for NGC 3115 dw01 at a distance of 9.7 Mpc. Consequently, the anti-covariance between M_{BH} M/L_{F814W} , stemming from the degeneracy between the potentials of the central black holes and the host galaxies, was prominently evident in the 3σ confidence levels within the 2D PDF.

Our simulations forecasted that ELT/HARMONI could acquire high-quality IFS and stellar kinematic data within a relatively short observation time, specifically in three hours or less. This emphasizes HARMONI’s potential as a state-of-the-art instrument for advancing our understanding of the aforementioned scientific objectives.

ACKNOWLEDGEMENTS

DDN is grateful to the LABEX Lyon Institute of Origins (ANR- 10-LABX-0066) Lyon for its financial support within the program ‘‘Investissements d’Avenir’’ of the French government operated by the National Research Agency (ANR). MPS acknowledges support from grant RYC2021-033094-I funded by MCIN/AEI/10.13039/501100011033 and the European Union NextGenerationEU/PRTR.

Facilities: HST/WFPC2, 2MASS, SDSS DR12, Gaia, DSS.

Software: python 3.12 (<https://www.python.org/>), Matplotlib 3.6.0 (<https://matplotlib.org/>), numpy 1.22 (<https://www.scipy.org/install.html>), scipy 1.3.1 (<https://www.scipy.org/install.html>), photutils 0.7 (<https://photutils.readthedocs.io/en/stable/>), MPFIT (<http://purl.com/net/mpfit>), plotbin 3.1.3 (<https://pypi.org/project/plotbin/>), astropy 5.1 (Astropy Collaboration et al. 2022), adamet 2.0.9 (Cappellari et al. 2013a), jampy 7.2.0 (Cappellari 2020), pPXF 8.2.1 (Cappellari 2023), vorbin 3.1.5 (Cappellari & Copin 2003), MgeFit 5.0.14 (Cappellari 2002) and HSIM 3.11 (Zieleniewski et al. 2015).

DATA AVAILABILITY

All data and software used in this paper are public. We provided their links in the text when discussed.

REFERENCES

- Ahn C. P., et al., 2018, *ApJ*, **858**, 102
 An J. H., Evans N. W., 2006, *ApJ*, **642**, 752
 Ashok A., et al., 2023, *ApJ*, **958**, 100
 Astropy Collaboration et al., 2022, *ApJ*, **935**, 167

- Avila R. J., Hack W. J., STScI AstroDrizzle Team 2012, in American Astronomical Society Meeting Abstracts #220. p. 135.13
- Bahcall J. N., Wolf R. A., 1977, *ApJ*, **216**, 883
- Bailes M., et al., 2021, *Nature Reviews Physics*, **3**, 344
- Baldassare V. F., Stone N. C., Foord A., Gallo E., Ostriker J. P., 2022, *ApJ*, **929**, 84
- Banerjee S., Baumgardt H., Kroupa P., 2010, *MNRAS*, **402**, 371
- Barth A. J., Ho L. C., Sargent W. L. W., 2002, *AJ*, **124**, 2607
- Barth A. J., Strigari L. E., Bentz M. C., Greene J. E., Ho L. C., 2009, *ApJ*, **690**, 1031
- Baumgardt H., et al., 2019, *MNRAS*, **488**, 5340
- Bell E. F., de Jong R. S., 2001, *ApJ*, **550**, 212
- Bennett D. P., et al., 2002, *ApJ*, **579**, 639
- Bianchini P., Sills A., van de Ven G., Sippel A. C., 2017, *MNRAS*, **469**, 4359
- Binney J., 1980, *MNRAS*, **190**, 873
- Böker T., Laine S., van der Marel R. P., Sarzi M., Rix H.-W., Ho L. C., Shields J. C., 2002, *AJ*, **123**, 1389
- Bono G., Caputo F., Marconi M., Musella I., 2010, *ApJ*, **715**, 277
- Bonoli S., Mayer L., Callegari S., 2014, *MNRAS*, **437**, 1576
- Busso G., et al., 2022, Gaia DR3 documentation Chapter 5: Photometric data, Gaia DR3 documentation, European Space Agency; Gaia Data Processing and Analysis Consortium. id. 5, doi:<https://gea.esac.esa.int/archive/documentation/GDR3/index.html>
- Calabrese E., et al., 2017, *Phys. Rev. D*, **95**, 063525
- Cappellari M., 2002, *MNRAS*, **333**, 400
- Cappellari M., 2008, *MNRAS*, **390**, 71
- Cappellari M., 2013, *ApJ*, **778**, L2
- Cappellari M., 2016, *ARA&A*, **54**, 597
- Cappellari M., 2020, *MNRAS*, **494**, 4819
- Cappellari M., 2023, *MNRAS*, **526**, 3273
- Cappellari M., Copin Y., 2003, *MNRAS*, **342**, 345
- Cappellari M., et al., 2011, *MNRAS*, **413**, 813
- Cappellari M., et al., 2013a, *MNRAS*, **432**, 1709
- Cappellari M., et al., 2013b, *MNRAS*, **432**, 1862
- Cardelli J. A., Clayton G. C., Mathis J. S., 1989, *ApJ*, **345**, 245
- Carlsten S. G., Greene J. E., Beaton R. L., Greco J. P., 2022, *ApJ*, **927**, 44
- Carson D. J., Barth A. J., Seth A. C., den Brok M., Cappellari M., Greene J. E., Ho L. C., Neumayer N., 2015, *AJ*, **149**, 170
- Charlot S., Fall S. M., 2000, *ApJ*, **539**, 718
- Ciotti L., Bertin G., 1999, *A&A*, **352**, 447
- Conroy C., Villaume A., van Dokkum P. G., Lind K., 2018, *ApJ*, **854**, 139
- Côté P., et al., 2006, *ApJS*, **165**, 57
- Crespo Gómez A., Piqueras López J., Arribas S., Pereira-Santaella M., Colina L., Rodríguez del Pino B., 2021, *A&A*, **650**, A149
- Davies R., et al., 2010, in McLean I. S., Ramsay S. K., Takami H., eds, Society of Photo-Optical Instrumentation Engineers (SPIE) Conference Series Vol. 7735, Ground-based and Airborne Instrumentation for Astronomy III. p. 77352A (arXiv:1005.5009), doi:10.1117/12.856379
- Davies R., et al., 2021, *The Messenger*, **182**, 17
- Davis T. A., Bureau M., Cappellari M., Sarzi M., Blitz L., 2013, *Nature*, **494**, 328
- Davis T. A., et al., 2020, *MNRAS*, **496**, 4061
- Dehnen W., 1993, *MNRAS*, **265**, 250
- Di Matteo T., Colberg J., Springel V., Hernquist L., Sijacki D., 2008, *ApJ*, **676**, 33
- Emsellem E., Monnet G., Bacon R., 1994, *A&A*, **285**, 723
- Erwin P., Gadotti D. A., 2012, *Advances in Astronomy*, **2012**, 946368
- Evans C. J., et al., 2011, *A&A*, **527**, A50
- Fabian A. C., 2012, *ARA&A*, **50**, 455
- Fahrion K., et al., 2020, *A&A*, **637**, A27
- Fahrion K., et al., 2022, *A&A*, **667**, A101
- Ferrarese L., Merritt D., 2000, *ApJ*, **539**, L9
- Gallo E., Treu T., Jacob J., Woo J.-H., Marshall P. J., Antonucci R., 2008, *ApJ*, **680**, 154
- García-Lorenzo B., Monreal-Ibero A., Mediavilla E., Pereira-Santaella M., Thatte N., 2019, *Frontiers in Astronomy and Space Sciences*, **6**, 73
- Gebhardt K., et al., 2000, *ApJ*, **539**, L13
- Gebhardt K., et al., 2001, *AJ*, **122**, 2469
- Gebhardt K., Rich R. M., Ho L. C., 2002, *ApJ*, **578**, L41
- Gebhardt K., Rich R. M., Ho L. C., 2005, *ApJ*, **634**, 1093
- Georgiev I. Y., Böker T., 2014, *MNRAS*, **441**, 3570
- Georgiev I. Y., Böker T., Leigh N., Lützgendorf N., Neumayer N., 2016, *MNRAS*, **457**, 2122
- González-Alfonso E., García-Bernete I., Pereira-Santaella M., Neufeld D. A., Fischer J., Donnan F. R., 2023, arXiv e-prints, p. arXiv:2312.04914
- Graham A. W., Erwin P., Trujillo I., Asensio Ramos A., 2003, *AJ*, **125**, 2951
- Graham M. T., et al., 2018, *MNRAS*, **477**, 4711
- Graham M. J., et al., 2020, *Phys. Rev. Lett.*, **124**, 251102
- Greene J. E., 2012, *Nature Communications*, **3**, 1304
- Greene J. E., Strader J., Ho L. C., 2020, *ARA&A*, **58**, 257
- Gültekin K., et al., 2009, *ApJ*, **698**, 198
- Gustafsson B., Edvardsson B., Eriksson K., Jørgensen U. G., Nordlund Å., Plez B., 2008, *A&A*, **486**, 951
- Haario H., Saksman E., Tamminen J., 2001, *Bernoulli*, **7**, 223
- Hägele G. F., Díaz Á. I., Cardaci M. V., Terlevich E., Terlevich R., 2007, *MNRAS*, **378**, 163
- Häring N., Rix H.-W., 2004, *ApJ*, **604**, L89
- Ho L. C., Greene J. E., Filippenko A. V., Sargent W. L. W., 2009, *ApJS*, **183**, 1
- Hoyer N., Neumayer N., Seth A. C., Georgiev I. Y., Greene J. E., 2023, *MNRAS*, **520**, 4664
- Huchra J. P., et al., 2012, *ApJS*, **199**, 26
- Inayoshi K., Visbal E., Haiman Z., 2020, *ARA&A*, **58**, 27
- Jarrett T. H., Chester T., Cutri R., Schneider S. E., Huchra J. P., 2003, *AJ*, **125**, 525
- Jedrzejewski R. I., 1987, *MNRAS*, **226**, 747
- Jerjen H., Freeman K. C., Binggeli B., 2000a, *AJ*, **119**, 166
- Jerjen H., Binggeli B., Freeman K. C., 2000b, *AJ*, **119**, 593
- Kacharov N., Neumayer N., Seth A. C., Cappellari M., McDermid R., Walcher C. J., Böker T., 2018, *MNRAS*, **480**, 1973
- Karachentsev I. D., Karachentseva V. E., Huchtmeier W. K., Makarov D. I., 2004, *AJ*, **127**, 2031
- Karachentsev I. D., Makarov D. I., Kaisina E. I., 2013, *AJ*, **145**, 101
- Kim S. C., Sung H., Park H. S., Sung E.-C., 2004, *Chinese J. Astron. Astrophys.*, **4**, 299
- Kochanek C. S., 2016, *MNRAS*, **461**, 371
- Kormendy J., Ho L. C., 2013, *ARA&A*, **51**, 511
- Kormendy J., Richstone D., 1995, *ARA&A*, **33**, 581
- Krajnović D., Cappellari M., McDermid R. M., 2018a, *MNRAS*, **473**, 5237
- Krajnović D., et al., 2018b, *MNRAS*, **477**, 3030
- Krist J., 1995, in Shaw R. A., Payne H. E., Hayes J. J. E., eds, Astronomical Society of the Pacific Conference Series Vol. 77, Astronomical Data Analysis Software and Systems IV. p. 349
- Krist J. E., Hook R. N., Stoehr F., 2011, in Kahan M. A., ed., Society of Photo-Optical Instrumentation Engineers (SPIE) Conference Series Vol. 8127, Optical Modeling and Performance Predictions V. p. 81270J, doi:10.1117/12.892762
- Lyubenova M., Kuntschner H., Rejkuba M., Silva D. R., Kissler-Patig M., Tacconi-Garman L. E., 2012, *A&A*, **543**, A75
- Ma C.-P., Greene J. E., McConnell N., Janish R., Blakeslee J. P., Thomas J., Murphy J. D., 2014, *ApJ*, **795**, 158
- Magorrian J., et al., 1998, *AJ*, **115**, 2285
- Maraston C., 2005, *MNRAS*, **362**, 799
- Maraston C., Strömbäck G., 2011, *MNRAS*, **418**, 2785
- Marconi A., Hunt L. K., 2003, *ApJ*, **589**, L21
- Markwardt C. B., 2009, in Bohlender D. A., Durand D., Dowler P., eds, Astronomical Society of the Pacific Conference Series Vol. 411, Astronomical Data Analysis Software and Systems XVIII. p. 251 (arXiv:0902.2850), doi:10.48550/arXiv.0902.2850
- Mezcua M., 2017, *International Journal of Modern Physics D*, **26**, 1730021
- Mitzkus M., Cappellari M., Walcher C. J., 2017, *MNRAS*, **464**, 4789
- Miyoshi M., Moran J., Herrnstein J., Greenhill L., Nakai N., Diamond P., Inoue M., 1995, *Nature*, **373**, 127
- Mould J. R., et al., 2000, *ApJ*, **529**, 786
- Müller O., et al., 2021, *ApJ*, **923**, 9
- Navarro J. F., Frenk C. S., White S. D. M., 1996, *ApJ*, **462**, 563

- Netzer H., 2015, *ARA&A*, **53**, 365
- Neumayer N., Walcher C. J., 2012, *Advances in Astronomy*, **2012**, 709038
- Neumayer N., Seth A., Böker T., 2020, *A&ARv*, **28**, 4
- Nguyen D. D., 2017, *arXiv e-prints*, p. [arXiv:1712.02470](https://arxiv.org/abs/1712.02470)
- Nguyen D. D., 2019, in *ALMA2019: Science Results and Cross-Facility Synergies*. p. 106, doi:[10.5281/zenodo.3585410](https://doi.org/10.5281/zenodo.3585410)
- Nguyen D. D., Seth A. C., Reines A. E., den Brok M., Sand D., McLeod B., 2014, *ApJ*, **794**, 34
- Nguyen D. D., et al., 2017, *ApJ*, **836**, 237
- Nguyen D. D., et al., 2018, *ApJ*, **858**, 118
- Nguyen D. D., et al., 2019, *ApJ*, **872**, 104
- Nguyen D. D., et al., 2020, *ApJ*, **892**, 68
- Nguyen D. D., et al., 2021, *MNRAS*, **504**, 4123
- Nguyen D. D., et al., 2022, *MNRAS*, **509**, 2920
- Nguyen D. D., Cappellari M., Pereira-Santaella M., 2023, *MNRAS*, **526**, 3548
- Norris M. A., et al., 2014, *MNRAS*, **443**, 1151
- Noyola E., Gebhardt K., Kissler-Patig M., Lützgendorf N., Jalali B., de Zeeuw P. T., Baumgardt H., 2010, *ApJ*, **719**, L60
- Oke J. B., 1974, *ApJS*, **27**, 21
- Ordenes-Briceño Y., et al., 2018, *ApJ*, **860**, 4
- Parodi B. R., Barazza F. D., Binggeli B., 2002, *A&A*, **388**, 29
- Pechetti R., Seth A., Neumayer N., Georgiev I., Kacharov N., den Brok M., 2020, *ApJ*, **900**, 32
- Pechetti R., et al., 2022, *ApJ*, **924**, 48
- Peterson R. C., Caldwell N., 1993, *AJ*, **105**, 1411
- Pinna F., et al., 2021, *ApJ*, **921**, 8
- Planck Collaboration et al., 2014, *A&A*, **571**, A16
- Rayner J. T., Cushing M. C., Vacca W. D., 2009, *ApJS*, **185**, 289
- Rossa J., van der Marel R. P., Böker T., Gerssen J., Ho L. C., Rix H.-W., Shields J. C., Walcher C.-J., 2006, *AJ*, **132**, 1074
- Saglia R. P., et al., 2016, *ApJ*, **818**, 47
- Sahu N., Graham A. W., Davis B. L., 2019a, *ApJ*, **876**, 155
- Sahu N., Graham A. W., Davis B. L., 2019b, *ApJ*, **887**, 10
- Sánchez-Janssen R., et al., 2019, *ApJ*, **878**, 18
- Schawinski K., Thomas D., Sarzi M., Maraston C., Kaviraj S., Joo S.-J., Yi S. K., Silk J., 2007, *MNRAS*, **382**, 1415
- Schiavon R. P., 2007, *ApJS*, **171**, 146
- Schlafly E. F., Finkbeiner D. P., 2011, *ApJ*, **737**, 103
- Schombert J., Smith A. K., 2012, *Publ. Astron. Soc. Australia*, **29**, 174
- Sersic J. L., 1968, *Atlas de galaxias australes*. Obs. Astron. Univ. Nacional de Córdoba, Córdoba
- Seth A., Agüeros M., Lee D., Basu-Zych A., 2008, *ApJ*, **678**, 116
- Seth A. C., et al., 2010, *ApJ*, **714**, 713
- Seth A. C., et al., 2014, *Nature*, **513**, 398
- Shields J. C., Walcher C. J., Böker T., Ho L. C., Rix H.-W., van der Marel R. P., 2008, *ApJ*, **682**, 104
- Silk J., Rees M. J., 1998, *A&A*, **331**, L1
- Skrutskie M. F., et al., 2006, *AJ*, **131**, 1163
- Spengler C., et al., 2017, *ApJ*, **849**, 55
- Steer I., et al., 2017, *AJ*, **153**, 37
- Straub O., Godet O., Webb N., Servillat M., Barret D., 2014, *A&A*, **569**, A116
- Thater S., Lyubenova M., Fahrion K., Martín-Navarro I., Jethwa P., Nguyen D. D., van de Ven G., 2023, *A&A*, **675**, A18
- Thatte N. A., et al., 2016, in *Evans C. J., Simard L., Takami H., eds, Society of Photo-Optical Instrumentation Engineers (SPIE) Conference Series Vol. 9908, Ground-based and Airborne Instrumentation for Astronomy VI*. p. 99081X, doi:[10.1117/12.2230629](https://doi.org/10.1117/12.2230629)
- Thatte N. A., et al., 2020, in *Evans C. J., Bryant J. J., Motohara K., eds, Society of Photo-Optical Instrumentation Engineers (SPIE) Conference Series Vol. 11447, Ground-based and Airborne Instrumentation for Astronomy VIII*. p. 114471W, doi:[10.1117/12.2562144](https://doi.org/10.1117/12.2562144)
- Tremaine S., Richstone D. O., Byun Y.-I., Dressler A., Faber S. M., Grillmair C., Kormendy J., Lauer T. R., 1994, *AJ*, **107**, 634
- Trujillo I., Erwin P., Asensio Ramos A., Graham A. W., 2004, *AJ*, **127**, 1917
- Valluri M., Ferrarese L., Merritt D., Joseph C. L., 2005, *ApJ*, **628**, 137
- Verolme E. K., et al., 2002, *MNRAS*, **335**, 517
- Volonteri M., 2012, *Science*, **337**, 544
- Volonteri M., Lodato G., Natarajan P., 2008, *MNRAS*, **383**, 1079
- Walcher C. J., et al., 2005, *ApJ*, **618**, 237
- Walcher C. J., Böker T., Charlot S., Ho L. C., Rix H. W., Rossa J., Shields J. C., van der Marel R. P., 2006, *ApJ*, **649**, 692
- Wallace L., Hinkle K., 1996, *ApJS*, **107**, 312
- Wallace L., Hinkle K., 1997, *ApJS*, **111**, 445
- Walsh J. L., Barth A. J., Ho L. C., Sarzi M., 2013, *ApJ*, **770**, 86
- Wang L., Tanikawa A., Fujii M., 2022, *MNRAS*, **515**, 5106
- Wevers T., van Velzen S., Jonker P. G., Stone N. C., Hung T., Onori F., Gezari S., Blagorodnova N., 2017, *MNRAS*, **471**, 1694
- Williams B. F., Dalcanton J. J., Stilp A., Dolphin A., Skillman E. D., Radburn-Smith D., 2013, *ApJ*, **765**, 120
- Zieleniewski S., Thatte N., Kendrew S., Houghton R. C. W., Swinbank A. M., Tecza M., Clarke F., Fusco T., 2015, *MNRAS*, **453**, 3754
- Zocchi A., Gieles M., Hénault-Brunet V., 2017, *MNRAS*, **468**, 4429
- Zocchi A., Gieles M., Hénault-Brunet V., 2019, *MNRAS*, **482**, 4713
- de Swardt B., Kraan-Korteweg R. C., Jerjen H., 2010, *MNRAS*, **407**, 955
- de Zeeuw T., 2001, in *Kaper L., Heuvel E. P. J. V. D., Woudt P. A., eds, Black Holes in Binaries and Galactic Nuclei*. p. 78 ([arXiv:astro-ph/0009249](https://arxiv.org/abs/astro-ph/0009249)), doi:[10.1007/10720995_12](https://doi.org/10.1007/10720995_12)
- den Brok M., van de Ven G., van den Bosch R., Watkins L., 2014, *MNRAS*, **438**, 487
- den Brok M., et al., 2015, *ApJ*, **809**, 101
- van Wassenhove S., Volonteri M., Walker M. G., Gair J. R., 2010, *MNRAS*, **408**, 1139
- van der Marel R. P., 1999, *AJ*, **117**, 744
- van der Marel R. P., Anderson J., 2010, *ApJ*, **710**, 1063

APPENDIX A: SUPPLEMENTARY FIGURES AND TABLES

This paper has been typeset from a $\text{\TeX}/\text{\LaTeX}$ file prepared by the author.

Table A1. Full list of our HARMONI IMBH survey: host galaxies' and their nuclear star clusters' properties

No.	Galaxy Name	R.A. (J2000) (h:m:s)	Decl. (J2000) (d:m:s)	D (Mpc)	Hubble Type	L_K (L_\odot)	$M_{\star, \text{gal.}}$ (M_\odot)	$\sigma_{\star, \text{NSC}}$ (km s^{-1})	$R_{e, \text{gal}}$ (kpc)	M_{NSC} (M_\odot)	$R_{e, \text{NSC}}$ (pc)	ref.
(1)	(2)	(3)	(4)	(5)	(6)	(7)	(8)	(9)	(10)	(11)	(12)	(13)
1	PGC046680	13:22:02.048	-42:32:07.34	3.77	-3.0	1.32×10^8	4.0×10^7	13.2	0.73	4.30×10^6	3.0	(1)
2	NGC 5206	13:33:43.961	-48:09:03.95	3.50	-3.0	1.05×10^9	2.5×10^9	46.0	0.99	1.54×10^7	3.4	(2)
3	ESO269-066	13:13:09.156	-44:53:23.63	3.66	-2.1	2.75×10^8	1.0×10^8	-	0.70	1.55×10^6	-	-
4	ESO269-068	13:13:11.917	-43:15:54.69	3.77	-2.1	8.91×10^7	1.7×10^7	-	0.41	-	-	-
5	NGC 4600	12:40:22.957	03:07:03.91	8.15	0.0	1.32×10^9	1.2×10^9	73.6	0.94	1.03×10^7	8.3	(2)
6	NGC 5102	13:21:57.610	-36:37:48.37	3.20	0.0	4.27×10^9	6.9×10^9	61.1	1.20	7.30×10^7	26.3	(3)
7	NGC 300	00:54:53.444	-37:41:03.22	2.01	6.9	5.00×10^8	1.0×10^9	47.0	2.94	1.05×10^6	8.0	(4, 5)
8	NGC 7793	23:57:49.753	-32:35:27.74	3.40	7.4	7.94×10^7	2.8×10^9	24.6	2.19	7.76×10^6	7.9	(4, 5)
9	NGC 3621	11:18:16.511	-32:48:50.55	6.60	7.0	2.24×10^{10}	7.9×10^9	43.0	2.60	1.01×10^7	4.2	(6)
10	NGC 247	00:47:08.470	-20:45:36.71	3.38	6.9	3.16×10^9	3.0×10^9	15.1	2.46	2.51×10^6	3.4	(7)
11	IC3077	12:24:22.18	21:09:35.95	9.12	5.8	1.45×10^8	1.3×10^9	25.0	1.40	-	-	-
12	NGC 5237	13:37:39.050	-42:50:49.099	3.33	-3.5	2.82×10^8	1.6×10^8	48.5	0.34	-	-	-
13	PGC029300	10:05:41.599	-07:58:53.40	9.70	-1.9	1.86×10^9	2.8×10^9	32.0	1.20	7.01×10^6	6.6	(3)
14	ESO384-016	13:57:01.370	-35 19 58.699	4.49	-4.9	6.76×10^7	6.0×10^7	-	0.69	-	-	-
15	ESO174-001	13:33:19.680	-53:21:16.88	3.60	-1.7	7.94×10^7	7.9×10^7	-	0.42	-	-	-
16	MESSIER083	13:37:00.950	-29:51:55.50	4.85	5.0	7.24×10^{10}	4.5×10^{10}	40.0	5.29	1.67×10^6	4.9	-
17	NGC 3593	11:14:37.001	12:49:03.61	9.20	-4.8	2.69×10^{10}	1.5×10^{10}	60.0	1.90	1.58×10^8	6	(3, 8)
18	ESO274-G001	15:14:14.554	-46:48:19.32	3.15	6.7	8.32×10^8	5.0×10^8	17.2	1.45	2.54×10^6	2.0	(3)
19	NGC 4713	12:49:57.874	05:18:41.04	10.7	6.8	-	3.0×10^{10}	23.2	2.12	-	-	-
20	NGC 3351	10:43:57.701	11:42:13.72	9.46	3.1	5.75×10^{10}	2.0×10^{10}	67.0	3.95	1.45×10^6	4.4	(9)
21	IC 5332	23:34:27.490	-36:06:03.89	4.63	6.8	5.50×10^9	4.7×10^9	58.3	1.18	6.95×10^6	23.2	(3)
22	NGC 1493	03:57:27.430	-46:12:38.52	11.3	6.0	-	4.0×10^9	25.0	-	1.51×10^6	4.2	-
23	NGC 1042	02:40:23.966	-08:26:00.74	4.21	6.0	-	2.1×10^9	32.0	1.09	2.12×10^6	1.3	(4)
24	PGC2815824	13:06:00.400	-36:19:42.4	4.21	-3.7	1.41×10^7	5.1×10^6	-	0.24	7.34×10^5	6.6	-
25	NGC 628	01:36:41.747	15:47:01.18	4.21	5.2	3.98×10^{10}	1.4×10^{10}	72.2	0.68	1.13×10^7	5.4	(10)
26	ESO059-01	07:31:18	-68:11:14	4.57	9.8	1.48×10^8	5.1×10^7	-	-	1.45×10^6	-	-
27	UGC 3755	07:13:51.57	10:31:16.53	4.99	9.9	2.69×10^8	9.3×10^7	-	-	6.03×10^4	0.5	(10)
28	IC 1959	03:33:12.53	-50:24:52.19	6.05	8.4	3.09×10^8	1.4×10^8	-	-	1.35×10^6	-	-
29	UGC 5889	10:47:22.4	14:04:16.58	6.89	8.9	3.55×10^8	1.6×10^8	-	-	1.23×10^6	1.0	(10)
30	NGC 4592	12:39:18.76	-00:31:55.61	10.6	7.9	1.45×10^9	1.0×10^9	38.9	-	6.31×10^5	1.1	(10)
31	NGC 1796	05:02:41.27	-61 08 18.79	10.6	5.3	-	1.2×10^9	-	-	6.61×10^6	2.6	-
32	ESO359-G029	04:12:50.52	-33:00:10.34	10.1	9.9	-	2.3×10^8	29.5	-	1.48×10^5	0.5	(10)
33	IC 4710	18:28:40.9	-66:59:10.0	8.91	8.9	1.74×10^9	1.3×10^9	67.2	-	2.49×10^6	1.0	(10)
34	NGC 1566	04:20:0.4	-54:56:16.5	9.95	4.0	-	1.5×10^{10}	116	-	1.49×10^8	2.3	(12)
35	NGC 2835	09:17:52.85	-22:21:16.79	10.8	5.0	2.19×10^{10}	5.1×10^9	70.7	-	4.07×10^6	3.4	(10)
36	NGC 4204	12:15:14.44	20:39:30.14	7.8	7.8	1.32×10^9	4.9×10^8	20.1	-	1.44×10^5	0.9	(10)
37	NGC 4517	12:32:45.51	00:06:54.9	10.6	6.0	1.86×10^{10}	1.2×10^{10}	28.3	-	7.01×10^5	2.3	(10)
38	NGC 5068	13:18:54.77	-21:02:19.66	6.03	6.0	5.37×10^9	4.83×10^9	15.6	-	5.31×10^5	5.1	(10)
39	NGC 5264	-	-	4.51	9.7	7.59×10^8	3.40×10^8	51.0	-	5.83×10^5	0.5	(10)
40	NGC 7090	21:36:28.19	-54 33 19.86	8.71	5.0	1.10×10^{10}	4.36×10^9	56.3	-	3.03×10^6	2.4	(10)
41	[KK2000] 03	02 24 44.4	-73 30 51	2.12	-4.9	7.70×10^7	2.30×10^7	-	-	1.35×10^5	3.8	(11)
42	LV J0956-0929	09 56 37.57	-09 29 10.8	9.37	-5	-	1.95×10^8	-	-	9.12×10^5	3.0	(11)
43	UGC 01104	01 32 42.53	+18 19 01.6	7.55	9.5	3.28×10^8	1.00×10^8	-	8.17	-	3.7	(11)
44	PGC 154449	09 57 08.88	-09 15 48.7	9.68	-1	1.60×10^8	5.01×10^7	-	5.25	-	-	(11)
45	ESO 553-046	05 27 05.72	-20 40 41.1	6.7	4	1.56×10^8	4.79×10^7	-	1.47	1.10×10^6	4.3	(11)

Notes: Columns 2, 3, and 4: Galaxy name, R.A., and Decl., respectively. Column 5: Distance to the galaxy from Earth. Column 6: Galaxy Hubble type. Column 7: the total galaxy's K -band luminosity estimated from the equation $M_K = K_T - 5 \log D - 25 - 0.11 \times A_V$ (Cappellari et al. 2011). Column 8: the total galaxy stellar mass estimated from equation $\log(M_\star) = 10.58 - 0.44 \times (M_K + 23)$ (Cappellari 2013). Columns 9, 10, 11, and 12: the nucleus stellar velocity dispersion, the galaxy effective radius that enclosed half of the galaxy mass or light, the nuclear star cluster mass, and the effective radius, respectively. Column 13: references - (1): Fahrion et al. (2020), (2): Nguyen et al. (2018), (3): Pechetti et al. (2020), (4): Walcher et al. (2005), (5): Neumayer & Walcher (2012), (6): Barth et al. (2009), (7): Carlsten et al. (2022), (8): Nguyen et al. (2021), (9): Ashok et al. (2023), (10): Georgiev & Böker (2014), (11): Hoyer et al. (2023). Target numbers from 41–45 are galaxies those are not present in Fig. 3 (main text).

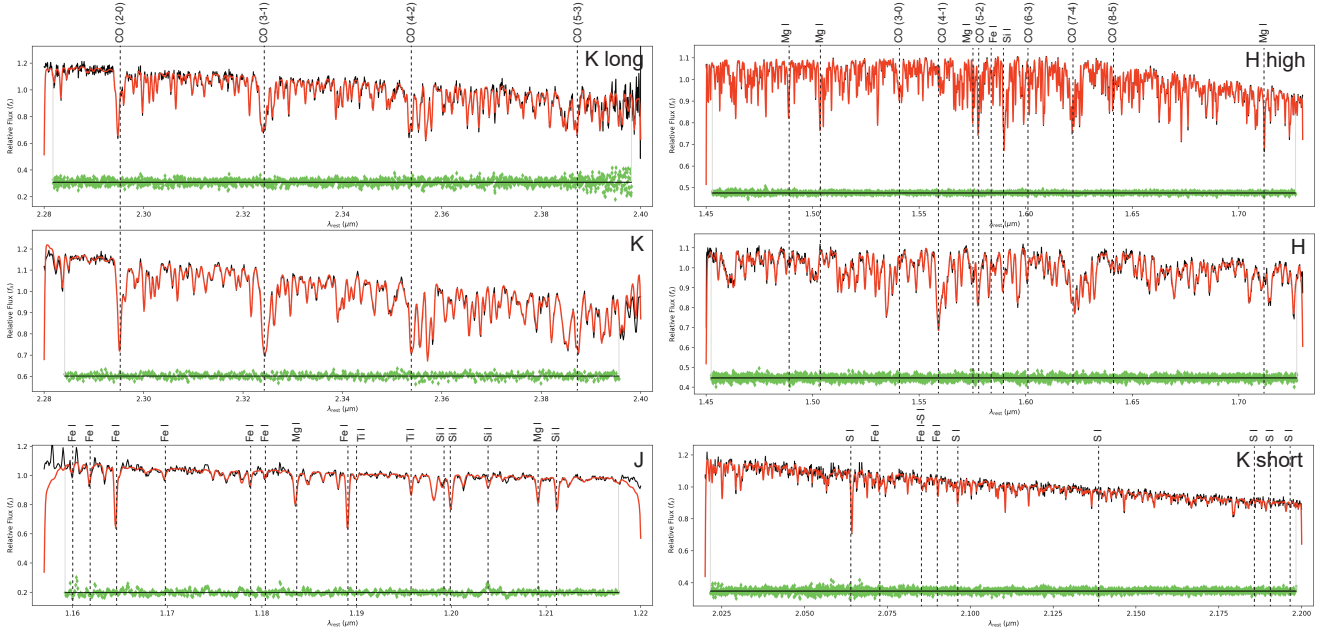


Figure A1. Parts of the simulated spectra over the six HSIM mock datacubes, which are fixed as the best spectral wavelength ranges for measuring the stellar kinematics for NGC 300 and NGC 3115 dw01, including $\lambda 2.28\text{--}2.40\ \mu\text{m}$ for both the K - and K -long, $\lambda 1.45\text{--}1.74\ \mu\text{m}$ for both the H - and H -high, and $\lambda 1.16\text{--}1.218\ \mu\text{m}$ for the J - and $\lambda 2.05\text{--}2.20\ \mu\text{m}$ for K -long, specifically. For the fixed spectra parts of the K - and K -long bands, we used the CO absorption bandheads (e.g. $^{12}\text{CO}(2\text{--}0)\ \lambda 2.293\ \mu\text{m}$, $^{12}\text{CO}(3\text{--}1)\ \lambda 2.312\ \mu\text{m}$, $^{12}\text{CO}(4\text{--}2)\ \lambda 2.351\ \mu\text{m}$, and $^{12}\text{CO}(5\text{--}3)\ \lambda 2.386\ \mu\text{m}$; Wallace & Hinkle 1997). For the fixed spectra parts of the H - and H -bands, we used the atomic-absorption species of Mg I $\lambda 1.487, 1.503, 1.575, 1.711\ \mu\text{m}$; Fe I $\lambda 1.583\ \mu\text{m}$; Si I $\lambda 1.589\ \mu\text{m}$ and the CO-absorptions lines of $^{12}\text{CO}(3\text{--}0)\ \lambda 1.540\ \mu\text{m}$; $^{12}\text{CO}(4\text{--}1)\ \lambda 1.561\ \mu\text{m}$; $^{12}\text{CO}(5\text{--}2)\ \lambda 1.577\ \mu\text{m}$; $^{12}\text{CO}(6\text{--}3)\ \lambda 1.602\ \mu\text{m}$; $^{12}\text{CO}(7\text{--}4)\ \lambda 1.622\ \mu\text{m}$; $^{12}\text{CO}(8\text{--}5)\ \lambda 1.641\ \mu\text{m}$. For the fixed spectrum part of the J -band, we used the atomic-absorption species of Ti I $\lambda 1.1896, 1.1953\ \mu\text{m}$; Si I $\lambda 1.1988, 1.1995, 1.2035, 1.2107\ \mu\text{m}$; Mg I $\lambda 1.1831, 1.2087\ \mu\text{m}$; Fe I $\lambda 1.1597, 1.1611, 1.1641, 1.1693, 1.1783, 1.1801, 1.1887, 1.1976\ \mu\text{m}$. For the fixed spectrum part of the K -short band, we used the atomic-absorption lines of Fe I $\lambda 2.088, 2.070\ \mu\text{m}$; Si I $\lambda 2.188, 2.183, 2.179, 2.137, 2.092, 2.062\ \mu\text{m}$, and the blended-absorption features of Fe I – Si I at $\lambda 2.070, \lambda 2.083\ \mu\text{m}$. In each panel plot, the black vertically thin-dashed lines indicate the positions of atomic/molecule absorptions of the stellar component extracted from one bin (black line) and its best-fit model produced by pPXF (red line). The two gray-vertical lines limit the wavelength range where the spectrum was fit, and blue dots show the residual between the galaxy spectrum and the best-fitting model (data–model). The kinematic results of these pPXF fits are shown in Figs 7 (main text) and A2 (below in this supplementary material) for NGC 300 and Figs 8 (main text) and A3 (below in this supplementary material) for NGC 3115 dw01 in terms of the 2D maps.

Table A2. The stellar-light MGE models of NGC 300 and NGC 3115 dw01

	$\log_{10} \Sigma_{\star,j}/(L_{\odot}\text{pc}^{-2})$	σ_j (")	$q'_j = b_j/a_i$	$\log_{10} \Sigma_{\star,j}/(L_{\odot}\text{pc}^{-2})$	σ_j (")	$q'_j = b_j/a_i$
(1)	(2)	(3)	(4)	(5)	(6)	(7)
j	NGC 300	NGC 300	NGC 300	NGC 3115 dw01	NGC 3115 dw01	NGC 3115 dw01
1	3.954	0.0007	0.90	4.298	0.0069	0.90
2	3.745	0.0012	0.90	4.791	0.0512	0.90
3	3.714	0.0020	0.90	4.339	0.1044	0.90
4	3.377	0.0028	0.90	3.201	0.2293	0.90
5	3.195	0.0039	0.90	2.886	0.6191	0.90
6	3.774	0.0052	0.90	2.739	1.3815	0.90
7	3.971	0.0119	0.90	2.570	2.8272	0.90
8	3.159	0.0174	0.90	2.376	5.4128	0.90
9	3.456	0.0267	0.90	2.154	9.8186	0.90
10	4.334	0.0358	0.90	1.905	17.040	0.90
11	4.778	0.0877	0.90	1.632	28.594	0.90
12	3.620	0.1103	0.90	1.332	47.157	0.90
13	4.814	0.1774	0.90	0.994	78.302	0.90
14	4.518	0.5033	0.75	0.587	136.755	0.90
15	3.312	57.735	0.75	−0.019	288.675	0.90

Notes: The MGE models used in JAMcyl model to create the input cubes for HSIM (Section 6.2) and recover the IMBH mass (Section 7.1). Each MGE model has 15 Gaussian components as shown in Column 1. Columns 2, 3 and 4: The MGE models that represented the mass models of the galaxies when scaled with a constant M/L_{F814W} and the Gaussian width along the major axis for NGC 300, respectively. Columns 5, 6 and 7: Similarities of Columns 2, 3 and 4 but for NGC 3115 dw01. Bold-face numbers are representative parameters for the Gaussians decomposed from the Core-Sérsic profile, which describes the NSC in each galaxy.

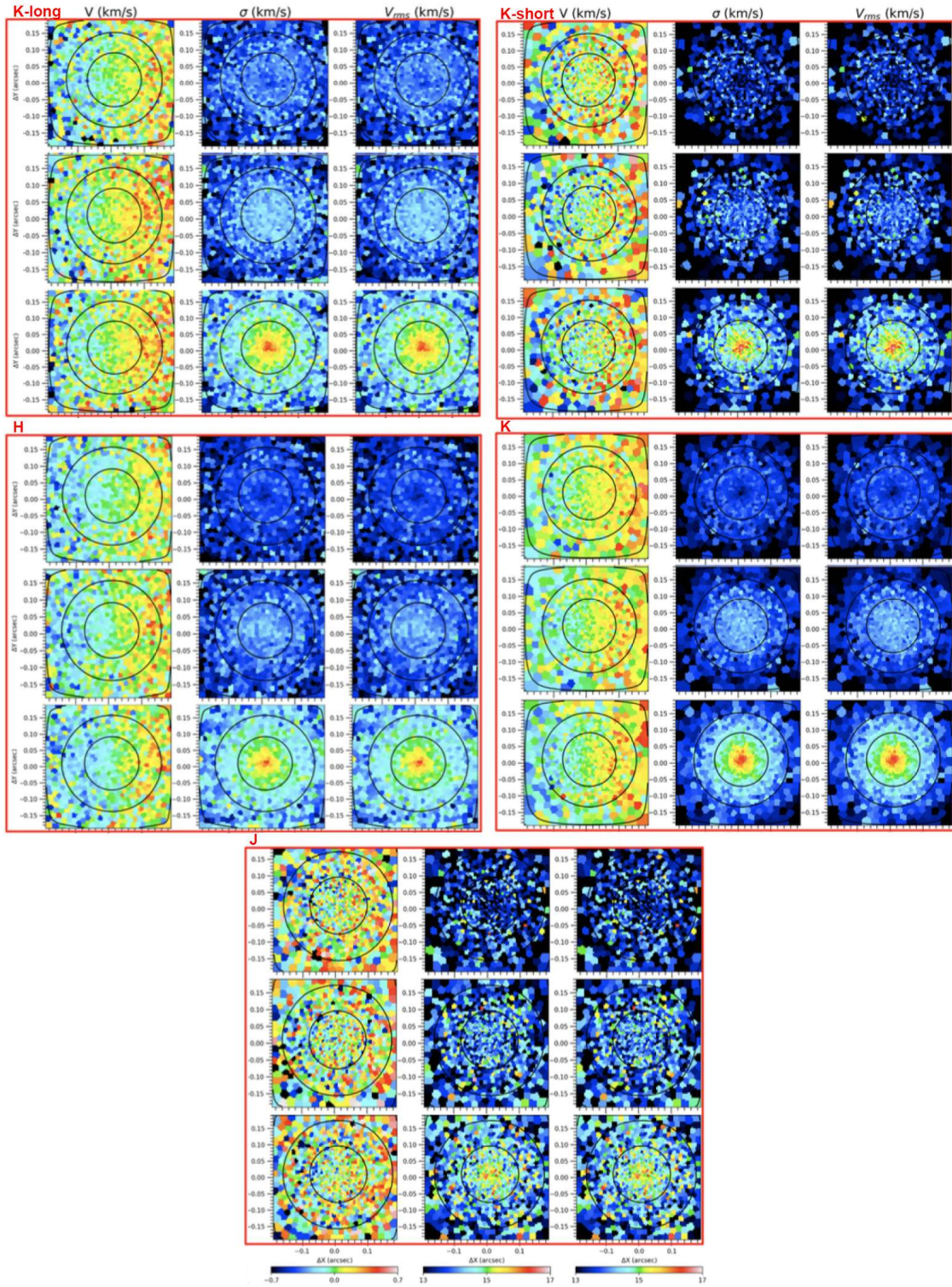


Figure A2. Mock kinematics for NGC 300: The stellar kinematic maps of NGC 300 extracted from the spectral part of $\lambda 2.28\text{--}2.40\ \mu\text{m}$ of the *K*-long (the top-left red-rectangular panel) and the *K* (the middle-right red-rectangular panel), from the spectral part of $\lambda 2.05\text{--}2.20\ \mu\text{m}$ of *K*-short (the top-right red-rectangular panel), from the spectral part of $\lambda 1.15\text{--}1.22\ \mu\text{m}$ of the *H* (the bottom-left red-rectangular panel), and from the spectral part of $\lambda 1.15\text{--}1.22\ \mu\text{m}$ of the *J* (the bottom red-rectangular panel) HSIM mock IFS datacubes produced from JAM_{cyl} (see Section 6.2 of the main text; Cappellari 2020) using Penalized PiXel-Fitting (pPXF; Cappellari 2023). In each red-rectangular panel, these maps are present with three different black hole masses: $M_{\text{BH}} = 0\ M_{\odot}$ (first-row plots), $M_{\text{BH}} = 5 \times 10^3\ M_{\odot}$ (second-row plots), and $M_{\text{BH}} = 10^4\ M_{\odot}$ (third-row plots). These IMBH masses are just a fraction of the NGC 300's NSC mass, including 0%, 0.5%, and 1%, respectively (also see the text). On each row of each red-rectangular panel, these maps are listed from left to right with (1) relative velocity (V) subtracted for the systemic velocity (V_{sys}) of the whole galaxy due to the Universe expansion, (2) velocity dispersion (σ_{\star}), (3) root-mean-squared velocity (V_{rms}); the black contours in all maps indicate the isophotes from the collapsed HSIM IFS cubes spaced by $1\ \text{mag arcsec}^{-2}$. The color bars at the bottom of the Fig are fixed at the same scale for all three black hole masses to illustrate the kinematic effects of the central black holes and also indicate the robustness of our proposed kinematic measurements at the centers of these dwarf galaxies hosting bright NSCs as the kinematic signatures for IMBHs.

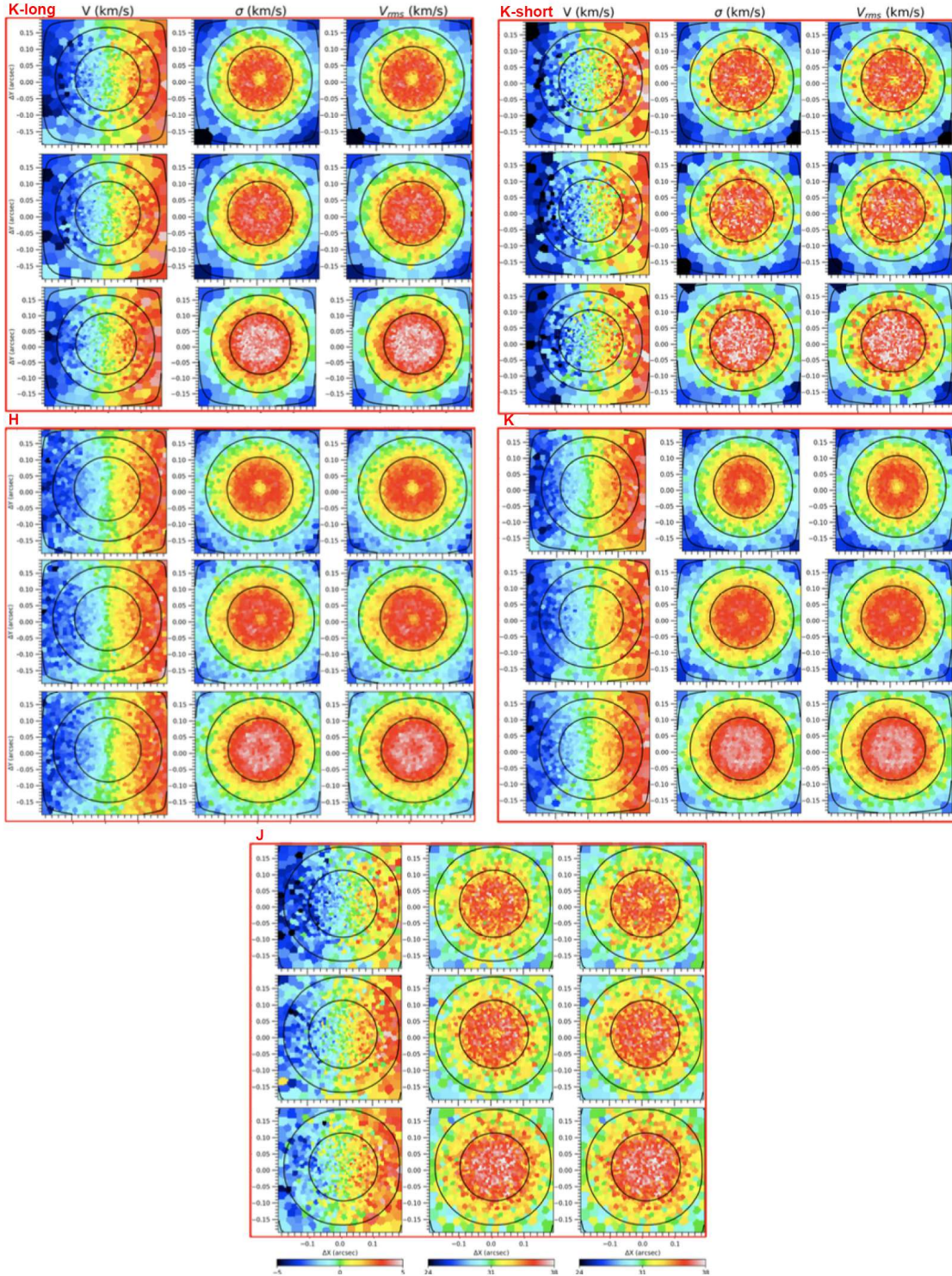


Figure A3. Mock kinematics for NGC 3115 dw01: The stellar kinematic maps of NGC 3115 dw01 extracted from the spectral part of $\lambda 2.28\text{--}2.40\ \mu\text{m}$ of the *K*-long (the top-left red-rectangular panel) and the *K* (the middle-right red-rectangular panel), from the spectral part of $\lambda 2.05\text{--}2.20\ \mu\text{m}$ of *K*-short (the top-right red-rectangular panel), from the spectral part of $\lambda 1.15\text{--}1.22\ \mu\text{m}$ of the *H* (the bottom-left red-rectangular panel), and from the spectral part of $\lambda 1.15\text{--}1.22\ \mu\text{m}$ of the *J* (the bottom-right red-rectangular panel) HSI_M mock IFS datacubes produced from JAM_{Cyl} (see Section 6.2 of the main text; Cappellari 2020) using (Penalized PiXel-Fitting (pPXf); Cappellari 2023). In each red-rectangular panel, these maps are present with three different black hole masses: $M_{\text{BH}} = 0\ M_{\odot}$ (first-row plots), $M_{\text{BH}} = 3.5 \times 10^4\ M_{\odot}$ (second-row plots), and $M_{\text{BH}} = 7 \times 10^4\ M_{\odot}$ (third-row plots). These IMBH masses are just a fraction of the NGC 3115 dw01’s NSC mass, including 0%, 0.5%, and 1%, respectively (also see the text). On each row of each red-rectangular panel, these maps are listed from left to right with (1) relative velocity (V) subtracted for the systemic velocity (V_{sys}) of the whole galaxy due to the Universe expansion, (2) velocity dispersion (σ_{\star}), (3) root-mean-squared velocity (V_{rms}); the black contours in all maps indicate the isophotes from the collapsed HSI_M IFS cubes spaced by $1\ \text{mag arcsec}^{-2}$. The color bars at the bottom of the Fig are fixed at the same scale for all three black hole masses to illustrate the kinematic effects of the central black holes and also indicate the robustness of our proposed kinematic measurements at the centers of these dwarf galaxies hosting bright NSCs as the kinematic signatures for IMBHs.

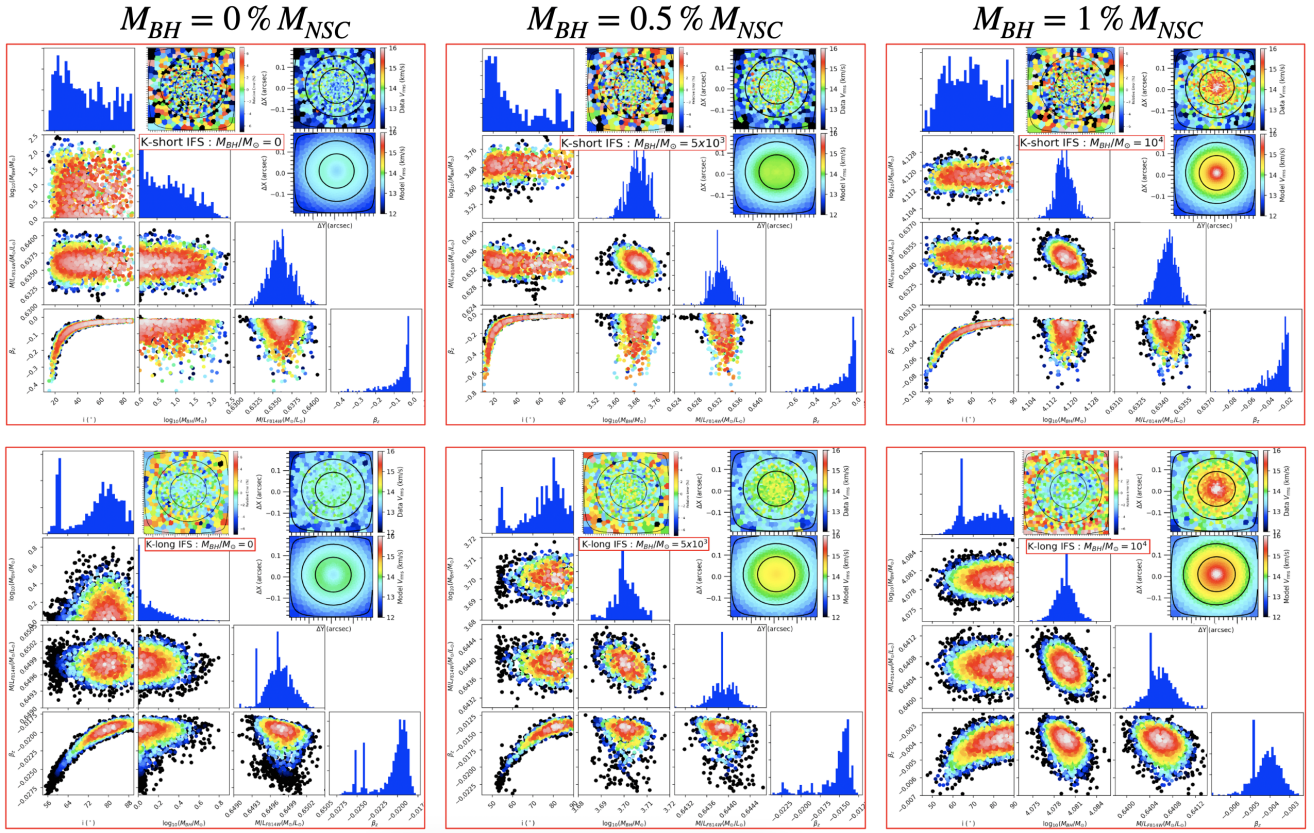


Figure A4. The figures display the posterior distributions obtained during the post-burn-in phase of the adamet MCMC optimization process for the JAM_{cyl} models applied to the HSIM simulated kinematics of NGC 300. These simulations were generated using the JAM_{cyl} models and feature three different black hole masses: $M_{BH} = 0\% M_{NSC} = 0 M_{\odot}$ (left panels), $M_{BH} = 0.5\% M_{NSC} = 5 \times 10^3 M_{\odot}$ (middle panels), and $M_{BH} = 1\% M_{NSC} = 10^4 M_{\odot}$ (right panels). Each red-square panel presents a set of four parameters, depicted as scatter plots illustrating their projected 2D distributions and histograms displaying their projected 1D distributions. These parameters include the inclination i , M_{BH} , M/L_{F814W} (mass-to-light ratio in the F814W band), and β_z . In the top right corner of each red-square panel, readers will find inset maps that depict the V_{rms} values. The top maps represent the simulated kinematic maps extracted from the simulated datacubes, while the bottom maps represent the kinematic maps recovered from the best-fit JAM_{cyl} model. These maps visually illustrate the level of agreement or disagreement at each spaxel (spatial pixel) between the simulated data and our chosen best-fit model. The determination of the best-fit JAM_{cyl} model is based on the probability distribution function (PDF) with the highest likelihood. These posterior distributions and associated maps are generated for HSIM simulated kinematics in two different wavelength bands: *K*-short (upper-row panels) and *K*-long (lower-row panels).

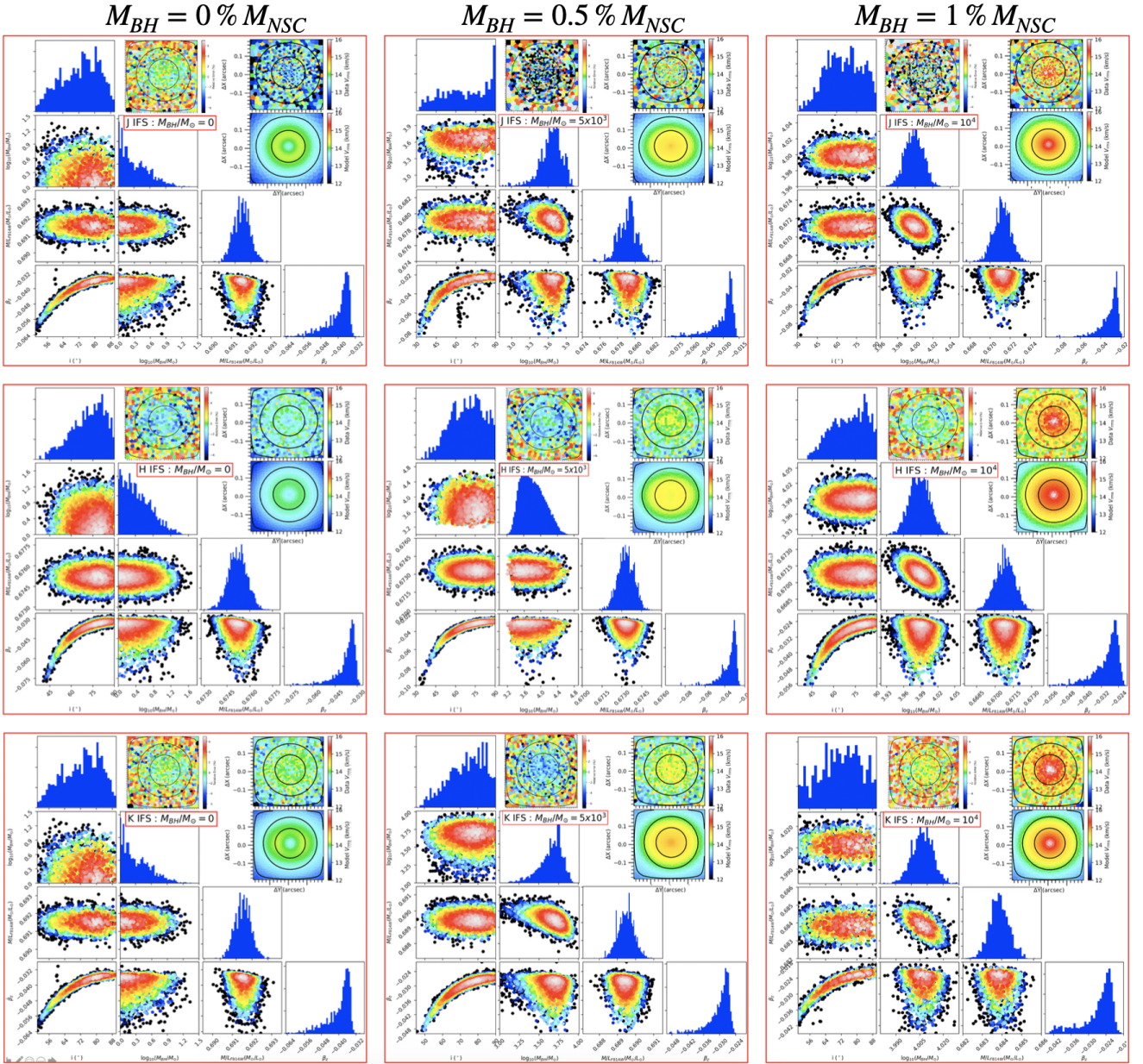


Figure A5. The figures display the posterior distributions obtained during the post-burn-in phase of the adamet MCMC optimization process for the JAM_{cy1} models applied to the HSIM simulated kinematics of NGC 300. These simulations were generated using the JAM_{cy1} models and feature three different black hole masses: $M_{\text{BH}} = 0\% M_{\text{NSC}} = 0 M_{\odot}$ (left panels), $M_{\text{BH}} = 0.5\% M_{\text{NSC}} = 5 \times 10^3 M_{\odot}$ (middle panels), and $M_{\text{BH}} = 1\% M_{\text{NSC}} = 10^4 M_{\odot}$ (right panels). Each red-square panel presents a set of four parameters, depicted as scatter plots illustrating their projected 2D distributions and histograms displaying their projected 1D distributions. These parameters include the inclination i , M_{BH} , M/L_{F814W} (mass-to-light ratio in the F814W band), and β_z . In the top right corner of each red-square panel, readers will find inset maps that depict the V_{rms} values. The top maps represent the simulated kinematic maps extracted from the simulated datacubes, while the bottom maps represent the kinematic maps recovered from the best-fit JAM_{cy1} model. These maps visually illustrate the level of agreement or disagreement at each spaxel (spatial pixel) between the simulated data and our chosen best-fit model. The determination of the best-fit JAM_{cy1} model is based on the probability distribution function (PDF) with the highest likelihood. These posterior distributions and associated maps are generated for HSIM simulated kinematics in three different wavelength bands: J (upper-row panels), H (middle-row panels), and K (lower-row panels).

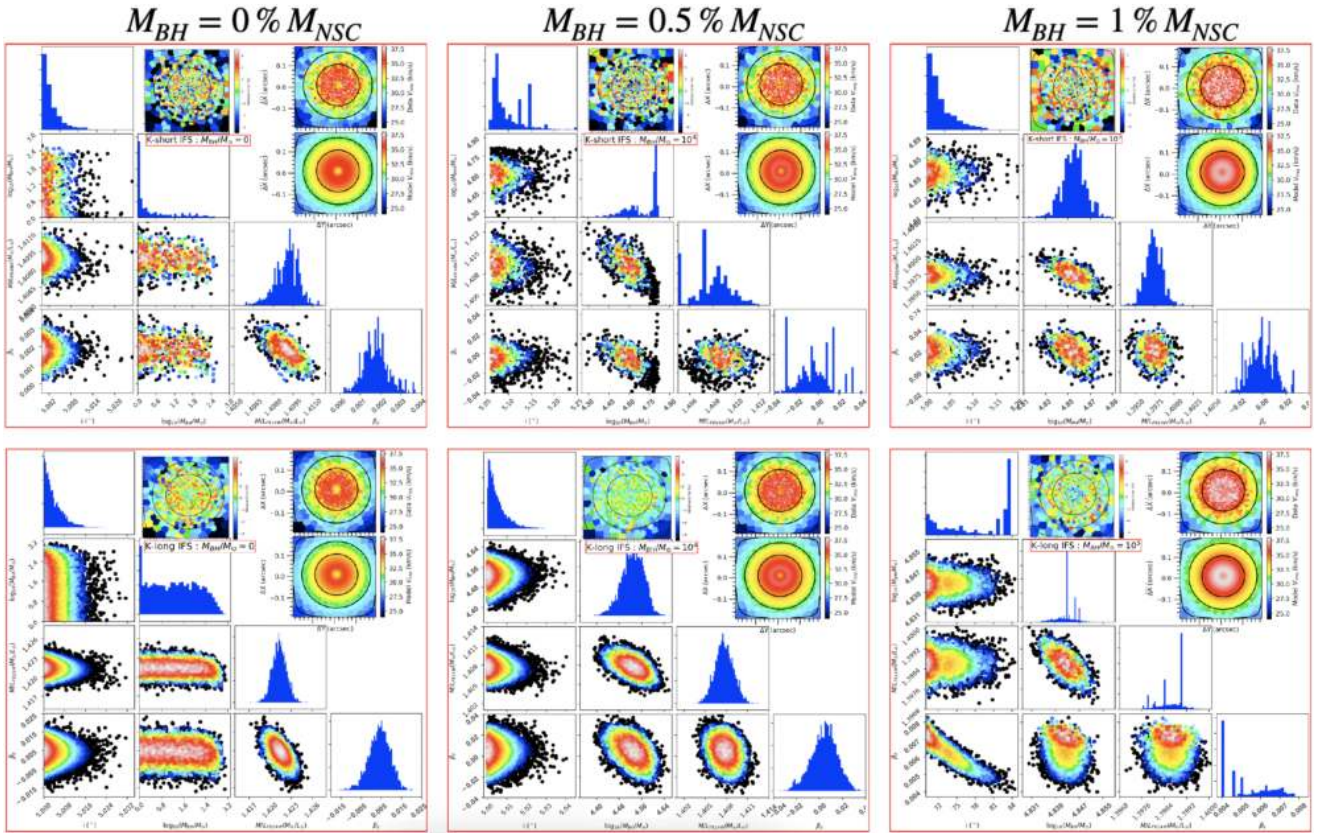


Figure A6. The figures display the posterior distributions obtained during the post-burn-in phase of the adamet MCMC optimization process for the JAM_{cyl} models applied to the HSIM simulated kinematics of NGC 3115 dw01. These simulations were generated using the JAM_{cyl} models and feature three different black hole masses: $M_{BH} = 0\% M_{NSC} = 0 M_{\odot}$ (left panels), $M_{BH} = 0.5\% M_{NSC} = 3.5 \times 10^4 M_{\odot}$ (middle panels), and $M_{BH} = 1\% M_{NSC} = 7 \times 10^4 M_{\odot}$ (right panels). Each red-square panel presents a set of four parameters, depicted as scatter plots illustrating their projected 2D distributions and histograms displaying their projected 1D distributions. These parameters include the inclination i , M_{BH} , M/L_{F814W} (mass-to-light ratio in the F814W band), and β_2 . In the top right corner of each red-square panel, readers will find inset maps that depict the V_{rms} values. The top maps represent the simulated kinematic maps extracted from the simulated datacubes, while the bottom maps represent the kinematic maps recovered from the best-fit JAM_{cyl} model. These maps visually illustrate the level of agreement or disagreement at each spaxel (spatial pixel) between the simulated data and our chosen best-fit model. The determination of the best-fit JAM_{cyl} model is based on the probability distribution function (PDF) with the highest likelihood. These posterior distributions and associated maps are generated for HSIM simulated kinematics in two different wavelength bands: K -short (upper-row panels) and K -long (lower-row panels).

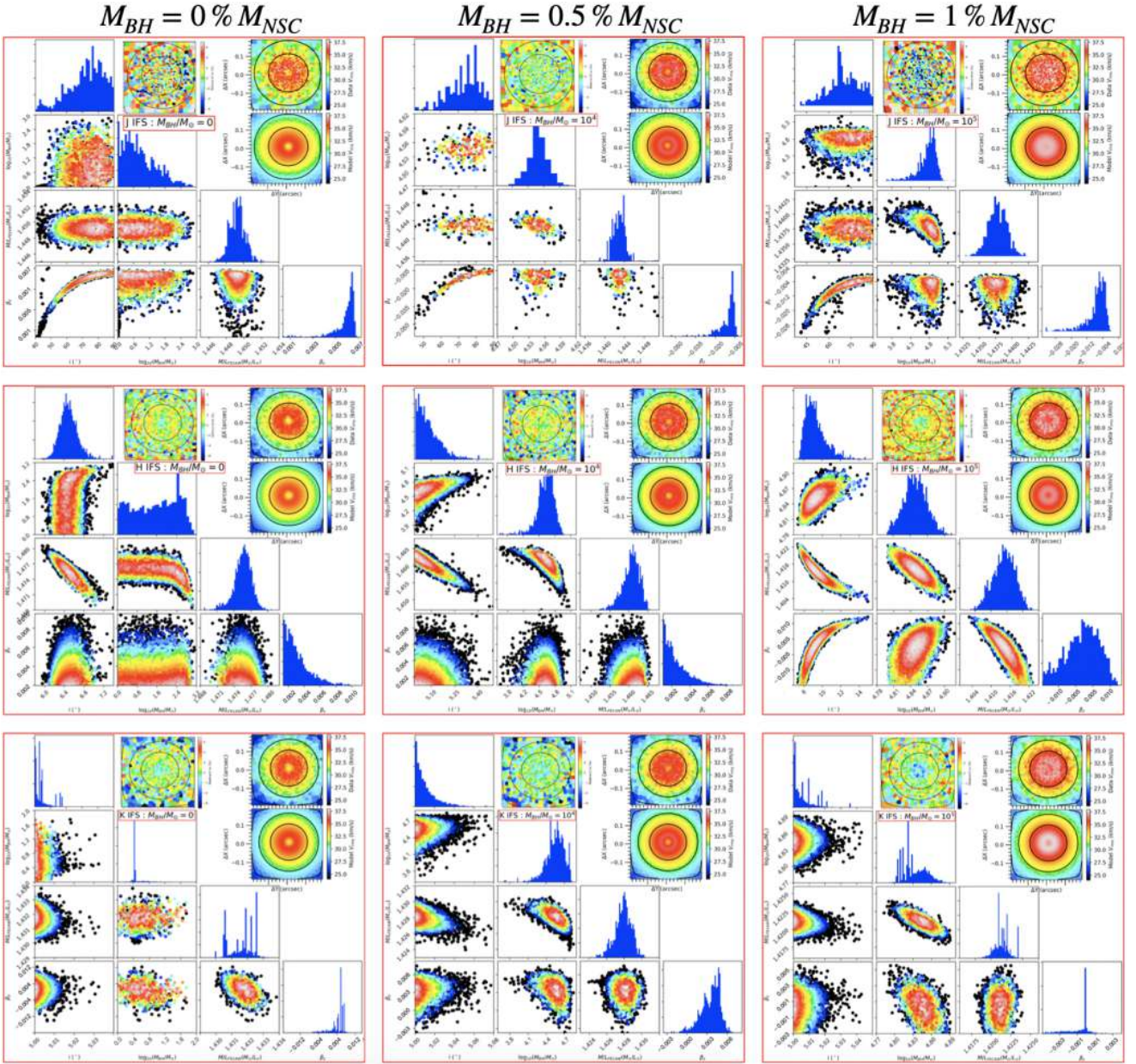


Figure A7. The figures display the posterior distributions obtained during the post-burn-in phase of the adamet MCMC optimization process for the JAM_{cy1} models applied to the HSIM simulated kinematics of NGC 3115 dw01. These simulations were generated using the JAM_{cy1} models and feature three different black hole masses: $M_{BH} = 0\% M_{NSC} = 0 M_{\odot}$ (left panels), $M_{BH} = 0.5\% M_{NSC} = 3.5 \times 10^4 M_{\odot}$ (middle panels), and $M_{BH} = 1\% M_{NSC} = 7 \times 10^4 M_{\odot}$ (right panels). Each red-square panel presents a set of four parameters, depicted as scatter plots illustrating their projected 2D distributions and histograms displaying their projected 1D distributions. These parameters include the inclination i , M_{BH} , M/L_{F814W} (mass-to-light ratio in the F814W band), and β_z . In the top right corner of each red-square panel, readers will find inset maps that depict the V_{rms} values. The top maps represent the simulated kinematic maps extracted from the simulated datacubes, while the bottom maps represent the kinematic maps recovered from the best-fit JAM_{cy1} model. These maps visually illustrate the level of agreement or disagreement at each spaxel (spatial pixel) between the simulated data and our chosen best-fit model. The determination of the best-fit JAM_{cy1} model is based on the probability distribution function (PDF) with the highest likelihood. These posterior distributions and associated maps are generated for HSIM simulated kinematics in three different wavelength bands: J (upper-row panels), H (middle-row panels), and K (lower-row panels).

Table A3. Best-fit JAM_{cy1} parameters and their statistical uncertainties for six mock IFS of NGC 300

Grating (1)	Parameters (2)	input $M_{\text{BH}} = 0 M_{\odot}$			input $\log_{10}(M_{\text{BH}}/M_{\odot}) = 3.7$			input $\log_{10}(M_{\text{BH}}/M_{\odot}) = 4$		
		(3) best-fit	(4) 1σ	(5) 3σ	(6) best-fit	(7) 1σ	(8) 3σ	(9) best-fit	(10) 1σ	(11) 3σ
			(16-84%)	(0.14-99.86%)		(0.14-99.86%)	(16-84%)		(16-84%)	(0.14-99.86%)
<i>H</i> -high	$\log_{10}(M_{\text{BH}}/M_{\odot})$	0.1	<0.5	<0.8	3.710	± 0.012	± 0.025	4.04	± 0.01	± 0.03
	$M/L_{\text{F814W}} (M_{\odot}/L_{\odot})$	0.676	± 0.001	± 0.003	0.67	± 0.001	± 0.003	0.665	± 0.001	± 0.002
	$i (^{\circ})$	77.2	± 7.7	± 19.0	80.0	± 9.1	± 17.6	80.0	± 8.2	± 17.2
	β_z	-0.027	± 0.002	± 0.006	-0.019	± 0.002	± 0.005	-0.017	± 0.002	± 0.006
<i>K</i> -short	$\log_{10}(M_{\text{BH}}/M_{\odot})$	0.5	<1.9	<2.4	3.70	± 0.04	± 0.17	4.117	± 0.004	± 0.013
	$M/L_{\text{F814W}} (M_{\odot}/L_{\odot})$	0.636	± 0.002	± 0.004	0.635	± 0.002	± 0.006	0.634	± 0.001	± 0.003
	$i (^{\circ})$	84	± 26	± 37	56	± 30	± 40	89	± 20	± 32
	β_z	-0.024	± 0.069	± 0.190	-0.028	± 0.120	± 0.400	-0.017	± 0.01	± 0.035
<i>K</i> -long	$\log_{10}(M_{\text{BH}}/M_{\odot})$	0.1	± 0.4	<0.7	3.703	± 0.005	± 0.015	4.080	± 0.001	± 0.004
	$M/L_{\text{F814W}} (M_{\odot}/L_{\odot})$	0.650	± 0.001	± 0.002	0.644	± 0.001	± 0.002	0.640	± 0.001	± 0.002
	$i (^{\circ})$	82	± 6	± 16	81	± 11	± 18	83.0	± 11	± 19
	β_z	-0.019	± 0.001	± 0.003	-0.014	± 0.002	± 0.009	-0.004	± 0.001	± 0.003
<i>J</i>	$\log_{10}(M_{\text{BH}}/M_{\odot})$	0.3	<0.6	<1.2	3.69	± 0.19	± 0.45	4.00	± 0.01	± 0.03
	$M/L_{\text{F814W}} (M_{\odot}/L_{\odot})$	0.692	± 0.003	± 0.008	0.679	± 0.001	± 0.003	0.671	± 0.001	± 0.003
	$i (^{\circ})$	80	± 7	± 16	82	± 14	± 30	75	± 16	± 29
	β_z	-0.038	± 0.140	± 0.460	-0.023	± 0.011	± 0.032	-0.025	± 0.009	± 0.033
<i>H</i>	$\log_{10}(M_{\text{BH}}/M_{\odot})$	0.1	<0.8	<1.6	3.66	± 0.32	± 0.91	4.00	± 0.03	± 0.06
	$M/L_{\text{F814W}} (M_{\odot}/L_{\odot})$	0.675	± 0.001	± 0.002	0.673	± 0.001	± 0.002	0.671	± 0.001	± 0.003
	$i (^{\circ})$	81	± 11	± 23	82	± 14	± 24	82	± 14	± 24
	β_z	-0.033	± 0.007	± 0.031	-0.025	± 0.006	± 0.017	-0.028	± 0.003	± 0.009
<i>K</i>	$\log_{10}(M_{\text{BH}}/M_{\odot})$	0.1	<0.7	<1.2	3.710	± 0.11	± 0.30	4.005	± 0.007	± 0.015
	$M/L_{\text{F814W}} (M_{\odot}/L_{\odot})$	0.691	± 0.001	± 0.002	0.689	± 0.001	± 0.002	0.684	± 0.001	± 0.002
	$i (^{\circ})$	80	± 11	± 22	79	± 15	± 31	80	± 15	± 25
	β_z	-0.038	± 0.006	± 0.016	-0.028	± 0.006	± 0.012	-0.025	± 0.003	± 0.012

Notes: We fixed the search ranges for all four model parameters (M_{BH} , M/L_{F814W} , β_z , and i) to ensure consistency in the fitting process. These ranges were set as follows:

- M_{BH} : from 0 to $10^6 M_{\odot}$ (or $\log_{10}(M_{\text{BH}}/M_{\odot})$: from 0 to 6)
- M/L_{F814W} : from 0.1 to 3 (M_{\odot}/L_{\odot})
- β_z : from -1.0 to 0.99
- i : from 5° to 90°

Column 1: The ELT/HARMONI grating. Column 2: The JAM_{cy1} model's parameters. Columns 3, 4, and 5: The best-fit parameters, 1σ (or 16-84%), and 3σ (or 0.14-99.86%) uncertainties provided by the JAM_{cy1} models, respectively, when constrained from the HARMONI mock kinematics. These model constraints are associated with the case of no input black hole ($M_{\text{BH}} = 0 M_{\odot}$). Columns 6, 7, and 8: Similarities of Columns 3, 4, and 5 but for the case of input black hole mass of $M_{\text{BH}} = 5 \times 10^3 M_{\odot}$. Columns 9, 10, and 11: Similarities of Columns 3, 4, and 5 but for the case of input black hole mass of $M_{\text{BH}} = 10^4 M_{\odot}$.

Table A4. Best-fit JAM_{cyl} parameters and their statistical uncertainties for six mock IFS of NGC 3115 dw01

Grating (1)	Parameters (2)	input $M_{\text{BH}} = 0 M_{\odot}$			input $\log_{10}(M_{\text{BH}}/M_{\odot}) = 4.544$			input $\log_{10}(M_{\text{BH}}/M_{\odot}) = 4.845$		
		(3) best-fit	(4) 1σ	(5) 3σ	(6) best-fit	(7) 1σ	(8) 3σ	(9) best-fit	(10) 1σ	(11) 3σ
		(16-84%)	(0.14-99.86%)		(0.14-99.86%)	(16-84%)		(16-84%)	(0.14-99.86%)	
<i>H</i> -high	$\log_{10}(M_{\text{BH}}/M_{\odot})$	2.4	<2.5	<2.6	4.543	± 0.031	± 0.091	4.850	± 0.020	± 0.050
	$M/L_{\text{F814W}} (M_{\odot}/L_{\odot})$	1.487	± 0.001	± 0.004	1.446	± 0.002	± 0.005	1.441	± 0.002	± 0.005
	$i (^{\circ})$	5.00	± 0.010	± 0.034	5.001	± 0.006	± 0.022	5.000	± 0.01	± 0.03
	β_z	0.003	± 0.002	± 0.006	0.005	± 0.005	± 0.018	0.003	± 0.001	± 0.003
<i>K</i> -short	$\log_{10}(M_{\text{BH}}/M_{\odot})$	0.5	<1.8	<2.4	4.550	± 0.13	± 0.27	4.850	± 0.01	± 0.08
	$M/L_{\text{F814W}} (M_{\odot}/L_{\odot})$	1.410	± 0.002	± 0.010	1.408	± 0.003	± 0.007	1.398	± 0.001	± 0.003
	$i (^{\circ})$	5.000	± 0.020	± 0.099	5.07	± 0.04	± 0.14	5.00	± 0.03	± 0.10
	β_z	0.002	± 0.001	± 0.002	-0.002	± 0.005	± 0.018	-0.002	± 0.007	± 0.022
<i>K</i> -long	$\log_{10}(M_{\text{BH}}/M_{\odot})$	1.2	<2.8	<3.2	4.540	± 0.04	± 0.12	4.843	± 0.003	± 0.010
	$M/L_{\text{F814W}} (M_{\odot}/L_{\odot})$	1.422	± 0.001	± 0.003	1.408	± 0.001	± 0.003	1.398	± 0.001	± 0.002
	$i (^{\circ})$	5.000	± 0.004	± 0.012	5.000	± 0.005	± 0.014	70.1	± 2.1	± 6.6
	β_z	0.004	± 0.006	± 0.015	0.000	± 0.012	± 0.031	0.007	± 0.001	± 0.002
<i>J</i>	$\log_{10}(M_{\text{BH}}/M_{\odot})$	1.0	<2.0	<2.5	4.540	± 0.015	± 0.043	4.830	± 0.240	± 0.750
	$M/L_{\text{F814W}} (M_{\odot}/L_{\odot})$	1.449	± 0.002	± 0.006	1.443	± 0.001	± 0.009	1.438	± 0.002	± 0.004
	$i (^{\circ})$	80	± 12	± 24	79	± 11	± 29	80	± 12	± 24
	β_z	-0.006	± 0.001	± 0.003	-0.007	± 0.006	± 0.020	-0.005	± 0.005	± 0.016
<i>H</i>	$\log_{10}(M_{\text{BH}}/M_{\odot})$	2.4	<2.0	<2.5	4.580	± 0.15	± 0.59	4.846	± 0.022	± 0.053
	$M/L_{\text{F814W}} (M_{\odot}/L_{\odot})$	1.475	± 0.002	± 0.007	1.463	± 0.003	± 0.007	1.414	± 0.004	± 0.009
	$i (^{\circ})$	6.49	± 0.18	± 0.69	5.006	± 0.075	± 0.210	9.0	± 1.2	± 3.5
	β_z	0.002	± 0.002	± 0.006	0.001	± 0.003	± 0.008	-0.001	± 0.008	± 0.019
<i>K</i>	$\log_{10}(M_{\text{BH}}/M_{\odot})$	0.5	<1.2	<1.6	4.550	± 0.16	± 0.54	4.845	± 0.023	± 0.045
	$M/L_{\text{F814W}} (M_{\odot}/L_{\odot})$	1.432	± 0.001	± 0.002	1.428	± 0.001	± 0.004	1.421	± 0.001	± 0.003
	$i (^{\circ})$	5.000	± 0.004	± 0.010	5.000	± 0.01	± 0.04	5.000	± 0.007	± 0.018
	β_z	0.001	± 0.004	± 0.012	0.003	± 0.002	± 0.005	-0.002	± 0.001	± 0.004

Notes: We fixed the search ranges for all four model parameters (M_{BH} , M/L_{F814W} , β_z , and i) to ensure consistency in the fitting process. These ranges were set as follows:

- M_{BH} : from 0 to $10^6 M_{\odot}$ (or $\log_{10}(M_{\text{BH}}/M_{\odot})$: from 0 to 6)
- M/L_{F814W} : from 0.1 to 3 (M_{\odot}/L_{\odot})
- β_z : from -1.0 to 0.99
- i : from 5° to 90°

Column 1: The ELT/HARMONI grating. Column 2: The JAM_{cyl} model's parameters. Columns 3, 4, and 5: The best-fit parameters, 1σ (or 16-84%), and 3σ (or 0.14-99.86%) uncertainties provided by the JAM_{cyl} models, respectively, when constrained from the HARMONI mock kinematics. These model constraints are associated with the case of no input black hole ($M_{\text{BH}} = 0 M_{\odot}$). Columns 6, 7, and 8: Similarities of Columns 3, 4, and 5 but for the case of input black hole mass of $M_{\text{BH}} = 3.5 \times 10^4 M_{\odot}$. Columns 9, 10, and 11: Similarities of Columns 3, 4, and 5 but for the case of input black hole mass of $M_{\text{BH}} = 7 \times 10^4 M_{\odot}$.